eXPRESS Polymer Letters Vol.6, No.10 (2012) 772
Available online at www.expresspolymlett.com
DOI: 10.3144/expresspolymlett.2012.82

Editorial corner – a personal view
Graphene and graphene/polymer nanocomposites

*B. K. Kim**

Department of Polymer Science and Engineering, Pusan National University, Busan 609-735, Korea

Since the single graphene layers were isolated from the graphite by Geim and Novoselov group in 2004, graphene triggered a gold rush for exploiting its possible applications. A search with graphene as a key word using the SciFinder shows even a tremendous increase of publication from 3900 (2010) to 9500 (2011) as they were awarded the novel prize in physics in 2010.

Graphene is a one-atom thick, two-dimensional sheet composed of sp^2 hybridized carbon atoms arranged in a honeycomb structure. It has combined benefits of layered silicates and carbon nanotubes, and is considered as the most promising reinforcing and functional filler of polymers.

Large area graphene is typically produced by bottom-up method such as chemical vapor deposition while flake type by top-down method consisting of oxidation of graphite, exfoliation of graphite oxide (GO) by sonication in liquid media, and reduction. Rapid thermal expansion of GO in inert atmosphere gives thermal exfoliation and reduction simultaneously and is suited for economical, large scale production without using any dispersion media.

The oxygen groups on the surface remaining upon reduction of GO enable dispersion in solvent and water and provide sites for chemical functionalization which allows covalent bonding with reactive polymer function (Advanced Materials, DOI: 10.1002/adma.201102036). For example, polyurethanes (PUs) are readily blended with graphene, and hydroxyl functions of graphene react with isocyanate termini of PU to form graphene/PU chemical hybrids. It is vital to control the type and amount of reactive sites on the graphene surface and edges. Markets for graphene are opened for i) energy saving electrodes as secondary cells for smartphone, notebook, electric car and solar cell, ii) transparent electrodes for flat panel (LCD, OLED) and touch screen, and iii) semiconductors. If graphene thin layer is properly deposited on glass or polymer surfaces, flexible displays, thin film transistors, and photovoltaic and LCD devices will be made possible (Macromolecules, DOI: 10.1021/ma100572e).

Graphene can be used as functional reinforcement for polymer to include packaging, gasketing, automotive, aircraft, ink, painting, sensor etc. When graphene is doped to PU, electrically and infrared light triggered shape memory material is synthesized where graphene provides crosslinks, strain energy storage and light absorption. However, low cost and large production of graphene will only expedite its applications. Otherwise, 'It is a dream. The prospect is so far beyond the horizon that we cannot even assess it properly', as Geim says.

Prof. Byung Kyu Kim
Member of International Advisory Board

*Corresponding author, e-mail: bkkim@pnu.edu

eXPRESS Polymer Letters Vol.6, No.10 (2012) 773–782
Available online at www.expresspolymlett.com
DOI: 10.3144/expresspolymlett.2012.83

Characterizations of polybenzoxazine modified with isomeric biphenyltetracarboxylic dianhydrides

S. Rimdusit[1*], *B. Ramsiri*[1], *C. Jubsilp*[2], *I. Dueramae*[1]

[1]Polymer Engineering Laboratory, Department of Chemical Engineering, Faculty of Engineering, Chulalongkorn University, 10330 Bangkok, Thailand
[2]Department of Chemical Engineering, Faculty of Engineering, Srinakharinwirot University, 26120 Nakhonnayok, Thailand

Received 25 February 2012; accepted in revised form 22 April 2012

Abstract. A series of polymeric alloying films were prepared from bisphenol A/aniline-based bifunctional benzoxazine resin (BA-a) with three isomeric biphenyltetracarboxylic dianhydrides, i.e., 2,3′,3,4′-biphenyltetra carboxylic dianhydride (a-BPDA), 2,2′,3,3′-biphenyltetracarboxylic dianhydride (i-BPDA), and 3,3′,4,4′-biphenyltetracarboxylic dianhydride (s-BPDA) through fully thermal curing. Chemical structure, thermomechanical property and thermal stability of bisphenol A/aniline type polybenzoxazine (PBA-a) copolymers were evaluated. Their chemical structures analyzed via Fourier transform infrared spectroscopy reveal ester carbonyl linkage formation between hydroxyl group of the PBA-a and anhydride group in the isomeric dianhydride. Glass transition temperatures (T_gs) of the dianhydride-modified PBA-a increased with PBA-a << i-BPDA < a-BPDA < s-BPDA. Degradation temperatures (T_d) of the PBA-a copolymers recorded to be in the range of 365–402°C were significantly higher than that of the neat PBA-a i.e. 334°C. Finally, char yield of the PBA-a copolymers was found to be about 54–57% which is about twofold increase from that of the parent PBA-a.

Keywords: *polymer blends and alloys, polybenzoxazine, isomeric dianhydride, thermal properties, mechanical properties*

1. Introduction

Polybenzoxazine, synthesized by the ring-opening polymerization reaction of cyclic benzoxazine resin only by thermal treatment without the need of catalyst and without producing any harmful by-products during the polymerization process, is recognized as an interesting new class of phenolic resin [1–5]. Moreover, polybenzoxazine provides some characteristics such as excellent dimension stability, high heat resistance, flame retardance and low moisture absorption as well as good dielectric properties in which cannot be found in traditional phenolic resins [6, 7]. Alloying of polybenzoxazine with various other resins or polymers has been reported to economically provide a novel class of resin systems with superior performance [1, 4, 8–15]. However, the major shortcoming of polybenzoxazine is its relatively high rigidity. Therefore, various efforts have been done to toughen polybenzoxazine such as by easily blending with more flexible monomers or polymers e.g. flexible epoxy resins [9, 12], urethane elastomers [8, 13], polyimides [14, 15] or dianhydrides [16, 17].

In recent reports, thermal and thermo-oxidative stabilities of polybenzoxazines have been substantially improved by alloying techniques [8, 15–18]. Alloying between benzoxazine resin and epoxy resin is considered to be a potentially effective measure to enhance thermal, mechanical properties, and flammability as well as processability of the polymers. Rimdusit *et al*. [12] investigated effects of epoxy resin on various arylamine-based benzoxazine resins,

*Corresponding author, e-mail: sarawut.r@chula.ac.th

i.e. aniline (BA-a), m-toluidine (BA-mt), and 3,5-xylidine (BA-35x) on processability, thermal, and mechanical properties of the polybenzoxazine copolymers. The authors reported that processing windows of the polybenzoxazine copolymers were found to be widened with epoxy resin content. Glass transition temperature (T_g) of the polybenzoxazine copolymers, i.e., PBA-a/epoxy resin and PBA-mt/epoxy resin, exhibited a synergistic behavior with the maximum T_g value, i.e. 183 and 215°C, respectively, at the polybenzoxazine blended with epoxy content of 20 wt%. Moreover, flexural strength and elongation at break of the polybenzoxazine alloys increased with increasing amount of the epoxy resin. Spontón *et al*. [19] developed a mixture of bis(m-aminophenyl)methylphosphine oxide-based benzoxazine (Bz-BAMPO) and glycidylether (DGEBA). The authors reported that the Bz-BAMPO: DGEBA at 2:1 mole ratio showed degradation temperature (T_d) at 5% weight loss of about 347°C compared to 333°C of Bz-BAMPO. Moreover, thermomechanical properties of bisphenol A and aniline-based polybenzoxazine (PBA-a) modified with highly flexible urethane elastomer (PU) [13] were reported. The obtained T_g of the PBA-a:PU copolymers was in a range of 177 to 245°C which was substantially greater than those of the parent polymers, i.e. T_g = 166°C for PBA-a, and T_g = –70°C for PU. Coefficient of thermal expansion of the copolymers showed a minimum value at PBA-a:PU (90:10) mass ratio. In addition, flexural strength of the alloys also exhibited a synergistic characteristic at the PBA-a:PU mass ratio of 90:10 with an ultimate value of 142 MPa. Takeichi *et al*. [15] disclosed a performance improvement of bisphenol A and aniline type polybenzoxazine (PBA-a) by blending with polyimide (PI). The authors reported that T_g values, degradation temperature and char yield of the copolymers were enhanced as the PI component increased. T_g of the PBA-a:PI copolymers was in a range of 186–205°C which was greater than that of the neat polybenzoxazine.

In more recent reports, organic acid dianhydrides have been shown to easily copolymerize with benzoxazine resin leading to substantially higher crosslink density of the copolymer network, thus greatly enhancing thermal stability of the polybenzoxazine [15, 16]. Jubsilp *et al*. [16] reported property enhancement of a novel bisphenol A and aniline-based polybenzoxazine (PBA-a) modified with 3,3′,4,4′-benzophenonetetracarboxylic dianhydride (BTDA). Fourier-transform infrared spectroscopy (FTIR) reveals ester linkage formation between hydroxyl group of the PBA-a and anhydride group of the BTDA. The PBA-a:BTDA copolymer films showed single T_g with the value as high as 263°C at BA-a:BTDA = 1.5:1 mole ratio. The value is remarkably higher than that of the unmodified PBA-a. In addition, the resulting PBA-a:BTDA copolymers display relatively high thermal stability with T_d at 5% weight loss up to 364°C and substantial enhancement in char yield at 800°C with a value up to 61% vs. that of 38% of the PBA-a.

In this work, a series of aromatic biphenyltetracarboxylic dianhydride isomers including a-BPDA, i-BPDA, and s-BPDA are investigated for their ability to form copolymer with bisphenol A-based benzoxazine resin (BA-a). The three isomers are originally synthesized to provide polyimides with improved solubility [20–22]. Curing behaviors, dynamic mechanical properties and thermal stability of the obtained polybenzoxazine copolymers are also reported.

2. Experimental

2.1. Materials

Materials used in this study are bisphenol A/aniline-based bifunctional benzoxazine resin (BA-a), dianhydrides, 1-methyl-2-pyrrolidone (NMP) as solvent. Benzoxazine resin based on bisphenol A, paraformaldehyde and aniline was synthesized according to the patented solventless technology [7]. Bisphenol A (polycarbonate grade) was provided by Thai Polycarbonate Co., Ltd., TPCC, (Rayong, Thailand). Paraformaldehyde (AR grade) and aniline (AR grade) were purchased from Merck Co., Ltd. (Darmstadt, Germany) and Panreac Quimica SA (Barcelona, Spain), respectively. Biphenyltetracarboxylic dianhydride isomers which are 2,3′,3,4′-biphenyltetracarboxylic dianhydride (a-BPDA), 2,2′,3,3′-biphenyltetracarboxylic dianhydride (i-BPDA), and 3,3′,4,4′-biphenyltetracarboxylic dianhydride (s-BPDA) are obtained from Japan Aerospace Exploration Agency, JAXA, (Prof. R. Yokota) (Ibaraki, Japan) and Akron Polymer Systems, Inc. (Ohio, United States). 1-methyl-2-pyrroli-

done (NMP) solvent was purchased from Fluka Chemical Co. (Bushs, Switzerland). All chemicals were used as-received.

BA-a resin was blended with various types of biphenyltetracarboxylic dianhydride isomers (DA) at BA-a:DA = 4:1, 3:1, 2:1, 1.5:1, and 1:1 mole ratios. The mixtures were dissolved in NMP and stirred at 80°C until a clear homogeneous mixture was obtained. The solution was cast on Teflon sheet and dried at room temperature for 24 h. Additional drying was carried out at 80°C for 24 h in a vacuum oven followed by thermal curing at 170°C for 1 h, at 190, 210, 230°C for 2 h each and 240°C for 1 h to guarantee complete curing of the mixtures.

2.2. Characterization methods

Glass transition temperatures (T_g) of all specimens were determined using a differential scanning calorimeter (DSC) model 2910 from TA Instruments (New Castle, DE, United States). The thermogram was obtained using a heating rate of 10°C/min from 30 to 300°C under nitrogen purging with a constant flow 50 mL/min. The specimen with a mass of 8–10 mg was sealed in an aluminum pan with lid. The $T_{g,\,DSC}$ was obtained from the temperature at half extrapolated tangents of the step transition midpoint.

Fourier transform infrared spectra of fully cured specimens were acquired at room temperature using a Spectrum GX FT-IR spectometer with an ATR accessory from PerkinElmer, Inc. (Waltham, Massachusette, United States). In the case of a BA-a and a pure biphenyltetracarboxylic isomers, a small amount of biphenyltetracarboxylic isomer powder was cast as thin film on a potassium bromide (KBr) window. All spectra were taken with 64 scans at a resolution of 4 cm^{-1} and in a spectral range of 4000–400 cm^{-1}.

A dynamic mechanical analyzer (DMA) model DMA242 from Netzsch, Inc. (Bavaria, Germany) was used to investigate viscoelastic properties of all specimens. The dimension of specimens has a width of 7.0 mm, a long 10 mm, and a 0.1 mm thick. The test was performed in a tension mode at a frequency of 1 Hz with a strain value of 0.1% and at a heating rate of 2°C/min from 30 to 400°C under nitrogen atmosphere with a constant flow 80 mL/min. The storage modulus (E'), loss modulus (E''), and loss tangent or damping curve ($\tan\delta$) were then obtained. The $T_{g,\,DMA}$ was taken as the maximum point on the loss modulus curve in the DMA thermograms.

Degradation temperature (T_d) at 5% weight loss and char yield at 800°C of all specimens were acquired using a Diamond TG/DTA from PerkinElmer, Inc. (Waltham, Massachusetts, United States). The testing temperature program was ramped at a heating rate of 20°C/min from 30 to 1000°C under nitrogen purging with a constant flow of 50 mL/min. The sample mass used was approximately 15 mg. T_ds and char yields of the specimens were reported at their 5% weight loss and at 800°C, respectively.

3. Results and discussion

3.1. Optimal composition of BA-a:dianhydride isomer mixtures

DSC thermograms of the fully cured PBA-a copolymers of BA-a:s-BPDA at various mole ratios ranging from 4:1, 3:1, 2:1, 1.5:1 and 1:1 are depicted in Figure 1. From this figure, we can see that the glass transition temperature ($T_{g,\,DSC}$) determined from a mid-point in initial slope change of DSC thermograms of the PBA-a copolymers increases with increasing amount of s-BPDA content until BA-a:s-BPDA = 1.5:1 mole ratio and then the $T_{g,\,DSC}$ value of the copolymer at 1:1 mole ratio tends to decrease. In other words, the ultimate value of $T_{g,\,DSC}$ of the copolymer was obtained at the BA-a:s-BPDA composition of 1.5:1 mole. All of the fully cured PBA-a:s-BPDA copolymers showed only single $T_{g,\,DSC}$ ranging from 170 to 257°C suggesting a single phase

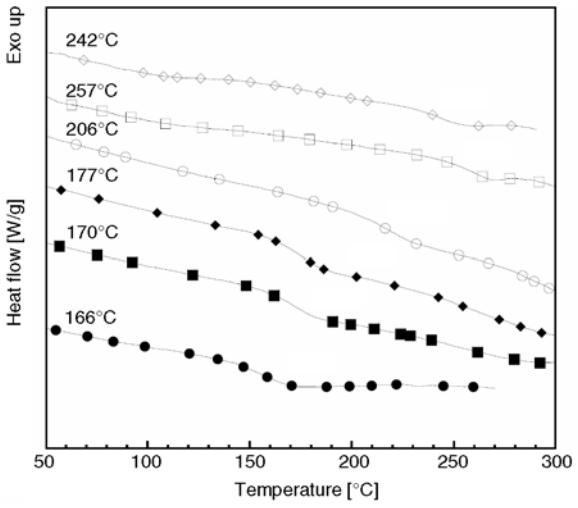

Figure 1. DSC thermograms of PBA-a:s-BPDA copolymer films at various mole ratios: (●) PBA-a, (■) BA-a:s-BPDA = 4:1, (◆) BA-a:s-BPDA = 3:1, (○) BA-a:s-BPDA = 2:1, (□) BA-a:s-BPDA = 1.5:1, and (◇) BA-a:s-BPDA = 1:1

material in these PBA-a-dianhydride copolymers. Those values are substantially greater than the $T_{g,\,DSC}$ of the neat PBA-a i.e. 166°C. From the $T_{g,\,DSC}$ results, the optimal network formation reaction of the PBA-a copolymers clearly required greater moles of benzoxazine monomers than those of the s-BPDA or did not follow the stoichiometric ratio of the two monomers. This is because an ability of the benzoxazine monomers to undergo self-polymerizability upon heating besides their ability to react with the dianhydrides. As a consequence, the consumption of the benzoxazine monomers tended to be greater than that of the dianhydrides in order to form a perfect network which may be related to the phenoxy-phenolic rearrangement that occurs during the formation for PBA-a [23]. This result is also in good agreement with the reaction of BA-a with BTDA [16]. In addition, DSC thermograms of the fully cured BA-a:a-BPDA and BA-a:i-BPDA copolymers at various dianhydride contents (not shown here) also provided similar trend on the T_g values. The maximum $T_{g,\,DSC}$ value of the copolymers prepared from BA-a:a-BPDA = 1.5:1 mole and BA-a:i-BPDA = 1.5:1 mole indicated about 245 and 237°C, respectively. The results show that each isomeric BPDA significantly affected the glass transition temperature of the copolymers as previously observed in polyimides based on isomeric BPDA [24].

3.2. Network formation by thermal cure of PBA-a:dianhydride isomer copolymers

Chemical structures of BA-a, PBA-a, isomeric dianhydride modifiers and their network formation reactions between the PBA-a and those isomeric dianhydride modifiers were studied using Fourier transform infrared spectroscopy (FT-IR) technique. The FT-IR absorption bands of the BA-a resin are previously reported in details [1, 15, 18]. In Figure 2, the important characteristics of infrared absorptions of BA-a resin were obviously observed at 947 and 1497 cm^{-1} attributed to the tri-substituted benzene ring and at 1232 cm^{-1} assigned to the asymmetric stretching of C–O–C group of oxazine ring. On the other hand, the biphenyltetracarboxylic dianhydride isomers, i.e., a-BPDA, i-BPDA, and s-BPDA, were identified by a distinctive carbonyl band region. From Figure 2, the spectrum of biphenyltetracarboxylic dianhydride isomer, e.g. a-BPDA, provided

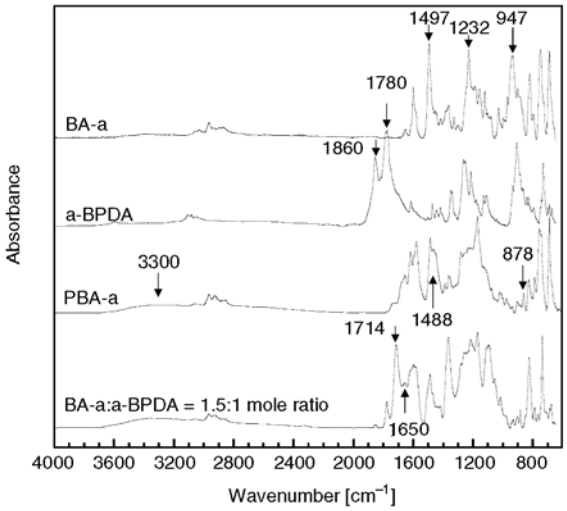

Figure 2. FTIR spectra of isomeric biphenyltetracarboxylic dianhydrides-modified PBA-a films of BA-a: a-BPDA = 1.5:1 mole

the characteristic absorption peaks with component in the 1780–1740 cm^{-1} region assigned to symmetric and 1860–1800 cm^{-1} region assigned to asymmetric starching of strong anhydride carbonyl groups [16, 25]. After thermal curing, an infinite three dimensional network was formed from benzoxazine ring opening by the breakage of C–O bond and then the benzoxazine molecule transformed from a ring structure to a network structure [6, 26]. During this curing process via ring opening reaction of the BA-a resin upon thermal treatment, the tri-substituted benzene ring around 1497 cm^{-1} which is the backbone of benzoxazine ring, became tetra-substituted benzene ring centered at 1488 and 878 cm^{-1} which led to the formation of a phenolic hydroxyl group-based polybenzoxazine structure. The phenolic hydroxyl group is also confirmed by the appearance of new absorption peak about 3300 cm^{-1}.

The chemical transformations of BA-a:a-BPDA at 1.5:1 mole ratio upon thermal curing were investigated and the resulting spectra are shown in Figure 2. The new absorption bands of PBA-a:a-BPDA copolymer were observed. The phenomenon was ascribed to the appearance of carbonyl stretching bands of ester linkages. From the PBA-a:biphenyltetracarboxylic dianhydride isomer spectrum in Figure 2, we can see that the anhydride carbonyl stretching bands of biphenyltetracarboxylic dianhydride at 1860 and 1780 cm^{-1} completely disappeared. It was suggested that the reaction between the phenolic hydroxyl group of the PBA-a and the

anhydride group of the biphenyl tetracarboxylic dianhydride isomer could occur to form ester carbonyl linkage as evidenced by the observed peak in the spectrum at 1730–1700 cm^{-1} of its C=O stretching of ester carbonyl group bonded phenolic hydroxyl group of the PBA-a modified with biphenyltetracarboxylic dianhydride [18]. Furthermore, the carboxylic acid occurred after thermal curing of the PBA-a:dianhydride isomer mixture can also be followed by monitoring a band at 1650–1670 cm^{-1} due to C=O stretching [27]. In addition, carboxylic acid shows characteristic C–O–H in-plane bending band at 1440–1395 cm^{-1}, C–O stretching band at 1320–1210 cm^{-1}, and C–O–H out-of-plane bending band at 960–900 cm^{-1}, respectively [25, 28]. Furthermore, the FTIR results for the i-BTDA and s-BTDA-modified PBA-a (not shown here) are relatively similar to a-BTDA-modified PBA-a.

As a consequence, the proposed reaction model of these mixtures was shown in Figure 3 which was similar to the cure reaction between anhydride group and hydroxyl group of the ring-opened epoxide group to form the ester carbonyl linkage [29–31] and a diglycidyl ether of bisphenol A-based epoxide resin (DGEBA) with dodecyl succinic anhydride (DDSA) [32] as well as reaction between BTDA dianhydride and hydroxyl group of 2-hydroxyethyl acrylate (HEA) [33].

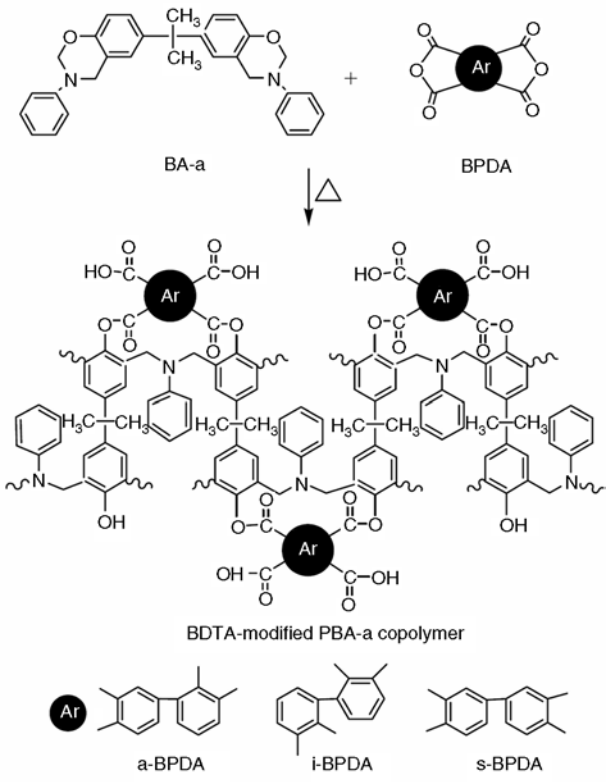

Figure 3. Model compound of isomeric BPDA-modified polybenzoxazine copolymers

3.3. Thermomechanical properties of PBA-a:dianhydride isomer copolymers

The mechanical properties of the PBA-a modified with isomeric biphenyltetracarboxylic dianhydrides, i.e. BA-a:a-BPDA, BA-a:i-BPDA, and BA-a:s-BPDA at 1.5:1 mole ratio were measured as a function of temperature. In this study dynamic tensile property was applied as dynamic mechanical analysis (DMA). The DMA thermograms were displayed in Figure 4, 5 and 6, respectively. Generally, the storage modulus of the materials demonstrates the deformation resistances of material when external force were applied sinusoidally. The storage moduli at room temperature (25°C) of PBA-a:a-BPDA, PBA-a:i-BPDA, and PBA-a: s-BPDA copolymers exhibited the values of 2.91, 2.89 and 3.42 GPa, respectively, which were higher than that of the neat PBA-a of 2.57 GPa as shown in Figure 4. This is due to higher crosslink density and greater aromatic content of the PBA-a copolymers with a greater amount of the isomeric biphenyltetracarboxylic dianhydride.

The effects of isomeric biphenyltetracarboxylic dianhydride on the crosslink density, ρ_x, of their polymer alloy network can be calculated from a value of the equilibrium storage shear modulus in the rubbery region, G'_e, which equals to $E'_e/3$ as follow in Equation (1) derived from the statistical theory of rubber elasticity by Nielsen [34]:

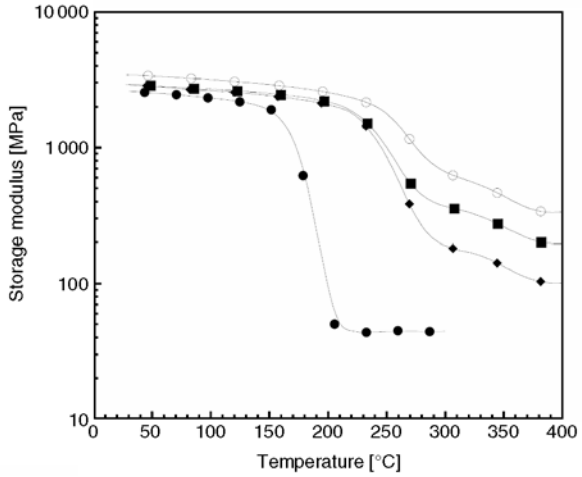

Figure 4. Storage modulus of isomeric biphenyltetracarboxylic dianhydrides-modified PBA-a films of BA-a:BPDA = 1.5:1 mole: (●) PBA-a, (■) PBA-a:a-BPDA, (◆) PBA-a:i-BPDA, (○) PBA-a:s-BPDA

$$\log(E'_e/3) = 7.0 + 293(\rho_x) \quad (1)$$

where E'_e is an equilibrium storage modulus in rubbery plateau [dyne/cm^2] and ρ_x is crosslink density [mol/cm^3] which is the mole number of network chains per unit volume of the polymers.

As expected, crosslink density values of the PBA-a and its copolymers i.e. PBA-a:a-BPDA, PBA-a:i-BPDA, and PBA-a:s-BPDA, calculated from Equation (1) are 3981, 7157, 6353 and 7664 mol/m^3, respectively. It is evident that the crosslink density of the neat PBA-a was greatly enhanced by an addition of isomeric biphenyltetracarboxylic dianhydrides, corresponding to an enhancement in their storage modulus values discussed previously. Moreover, we can see that the storage modulus at room temperature of the isomeric BPDA-modified PBA-a copolymer films increases with i-BPDA < a-BPDA < s-BPDA as similarly reported in polyimide film derived from isomeric BPDA/*p*,*p*′-ODA and isomeric BPDA/1,4,4-APB [35]. This behavior results from the greater interaction of the macromolecules and denser packing of s-BPDA than those of a-BPDA and i-BPDA. In case of i-BPDA based polyimides, the polyimides tend to form internal cyclization which may be lead to obtain lower interaction of the macromolecules and rather low molecular weights than s-BPDA based polyimides [36].

Figure 5 displays glass transition temperature, the maximum point on the loss modulus curve ($T_{g,\,DMA}$), related to molecular motion at structural level determimed from of the PBA-a:a-BPDA, PBA-a:i-BPDA, and PBA-a:s-BPDA copolymer films. From the figure, the neat PBA-a and its copolymers showed only single $T_{g,\,DMA}$ as reported in DSC thermogram in Figure 1. This result suggested that all kinds of PBA-a:isomeric biphenyltetracarboxylic dianhydride copolymer films were homogeneous and no phase separation occurred in these copolymers. From Figure 5, the $T_{g,\,DMA}$ value of the neat PBA-a was determined to be about 178°C and those of the PBA-a modified with isomeric biphenyltetracarboxylic dianhydrides films were found to be in the range of 239–266°C. The $T_{g,\,DMA}$ value of the neat PBA-a was clearly enhanced by blending with the a-BPDA or i-BPDA or s-BPDA dianhydrides. The obtained high $T_{g,\,DMA}$ value of PBA-a:isomeric biphenyltetracarboxylic dianhydride copolymers can be attributed to the improved crosslink structure

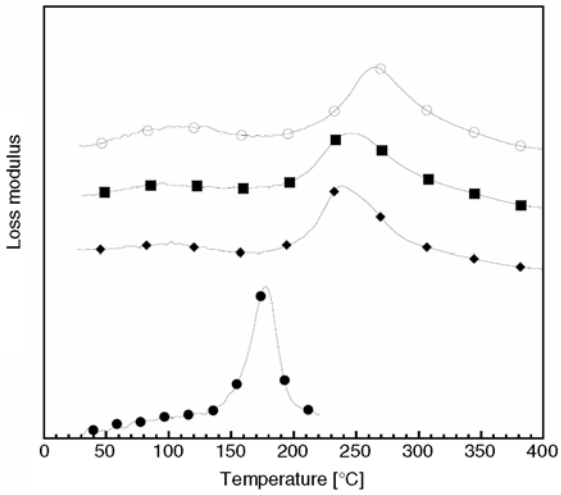

Figure 5. Loss modulus of isomeric biphenyltetracarboxylic dianhydrides-modified PBA-a films of BA-a:BPDA = 1.5:1 mole: (●) PBA-a, (■) PBA-a:a-BPDA, (◆) PBA-a:i-BPDA, (○) PBA-a:s-BPDA

via ester carbonyl linkage between phenolic hydroxyl group of PBA-a and anhydride group of isomeric biphenyltetracarboxylic dianhydride as seen in FT-IR spectra and their high aromatic content from the presence of the dianhydrides in the copolymers network as well as hydrogen bonding between ester carbonyl group (C=O) or OH groups in a carboxylic acid and phenolic hydroxyl group (–OH) of the PBA-a. Moreover, the T_g values of PBA-a copolymers measured by DMA displayed descending order on basis of both molecular packing and chain conformation such as semirigid s-BPDA and bent chain a-BPDA structures of isomeric biphenyltetracarboxylic dianhydrides [37, 38]. In our experiments, the order of T_g's PBA-a: s-BPDA (266°C) > PBA-a:a-BPDA (247°C) > PBA-a: i-BPDA (239°C) was observed as similarly investigated in [23]. This observation implied that the T_g values were also dependent on stiff/linear chain of these isomeric biphenyltetracarboxylic dianhydride moieties that a decrease in the chain linearity as follow s-BPDA > a-BPDA > i-BPDA caused an increase of energy to motivate motions in PBA-a:s-BPDA copolymer as compared with that of PBA-a:a-BPDA and PBA-a:i-BPDA copolymers and thus results in higher T_g for the PBA-a:s-BPDA copolymer as compared to latter copolymers.

The loss tangent (tan δ) of the neat PBA-a and their copolymers with various types of isomeric biphenyltetracarboxylic dianhydrides was illustrated in Figure 6. The peak height of the tan δ of the PBA-a:

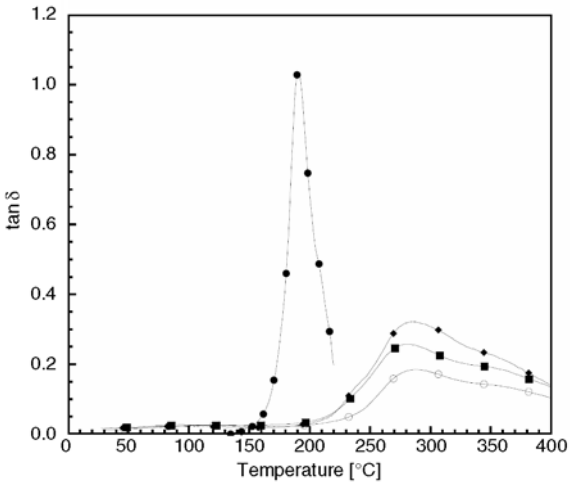

Figure 6. Loss tangent of isomeric biphenyltetracarboxylic dianhydrides-modified PBA-a films of BA-a:BPDA = 1.5:1 mole: (●) PBA-a, (■) PBA-a:a-BPDA, (◆) PBA-a:i-BPDA, (○) PBA-a:s-BPDA

a-BPDA, PBA-a:i-BPDA, and PBA-a:s-BPDA tended to decrease while the peak position of their PBA-a copolymers shifted to a higher temperature. The results indicated that the increase in the crosslink density with decreasing the chain's segmental mobility in the PBA-a modified with biphenyltetracarboxylic dianhydride isomers. This characteristic of the copolymers conformed to increasing of T_g's copolymer as follow s-BPDA > a-BPDA > i-BPDA. Furthermore, the width-at-half-height of tan δ curves was broader in their PBA-a copolymers, which confirmed the more heterogeneous network in the resulting copolymers due to a hybrid polymer network formation. Moreover, the obtained transparent copolymer films and the single tan δ peak observed in each copolymer suggested no macroscopic phase separation in their PBA-a copolymer films.

3.4. Visual appearance of PBA-a:dianhydride isomer copolymers

Because of the ester carbonyl linkage, structurally flexible functional group, formed after thermal curing stages, the enhancement of the PBA-a:dianhydride isomer copolymer bending was expected. A transparent brown neat PBA-a film and red brown PBA-a blended with isomeric biphenyltetracarboxylic dianhydrides at the neat BA-a equal to 1.5 mole and dianhydride isomer equal to 1 mole which showed the highest $T_{g,\,DMA}$ value of the PBA-a copolymers were obtained. The visual appearances of the cured PBA-a copolymer specimens are presented in Figure 7. We can see that the PBA-a specimen of about 100 μm thick is rather brittle, and it can not be bent further than as shown in Figure 7a due to the internal hydrogen bonding among hydroxyl and amino groups of the PBA-a. Whereas the homogeneous specimens of all the PBA-a copolymers of the same thickness as illustrated in Figures 7b–7d showed a remarkable improvement in their tough-

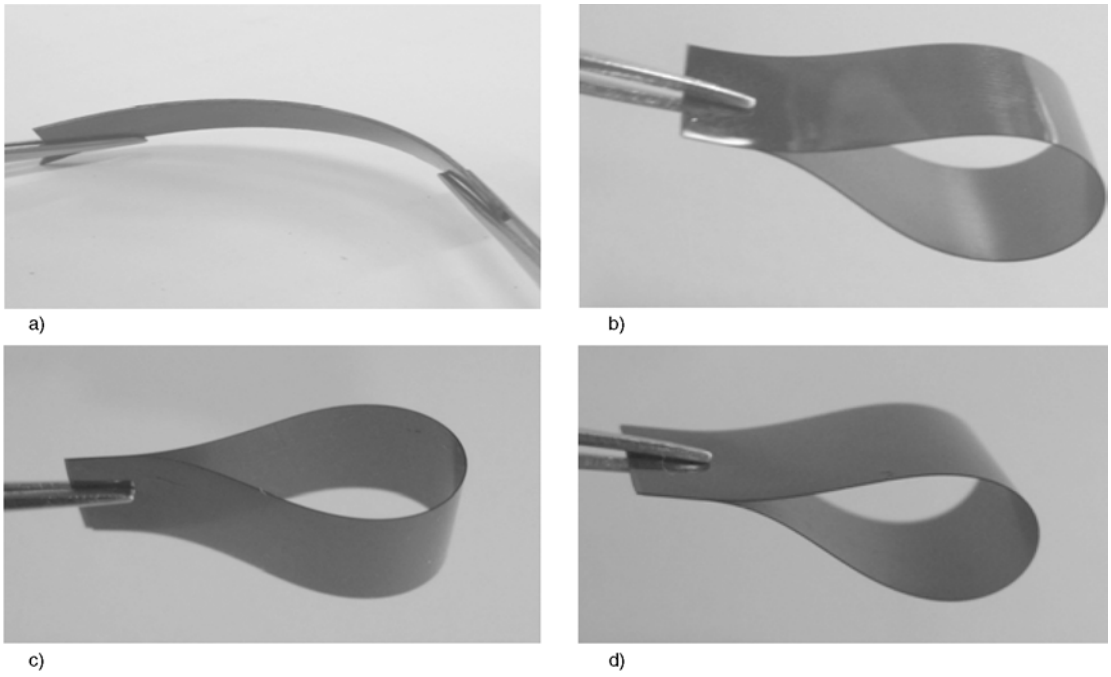

Figure 7. Visual appearances of isomeric biphenyltetracarboxylic dianhydrides-modified PBA-a films of BA-a:BPDA = 1.5:1 mole: (a) PBA-a, (b) PBA-a:a-BPDA, (c) PBA-a:i-BPDA, (d) PBA-a:s-BPDA

ness. The toughness enhancement of the PBA-a copolymer specimens, actually, due to ester carbonyl linkages (C=O) formed in the PBA-a copolymer network. Moreover, the formation of the esters might result in the breaking of the internal hydrogen bonding of the PBA-a. The new hydrogen-bonding tends to be random; therefore, the total polymer network structure could be more flexible. In addition, the great toughness of the PBA-a copolymers in Figures 7b–7d is similar to that of the commercial polyimide films such as UPILEX®S film presented by Ube Industries, Ltd. and Kapton®H films [39].

3.5. Thermal stability of PBA-a:dianhydride isomer copolymers

Figure 8 depicted the TGA thermogram results of three kinds of representative isomeric biphenyltetracarboxylic dianhydride-modified PBA-a, i.e., PBA-a:a-BPDA, PBA-a:i-BPDA, and PBA-a:s-BPDA copolymer films consisted of BA-a equal to 1.5 mole and dianhydride isomer equal to 1 mole. The degradation temperature (T_d), expressed as the 5% weight loss under nitrogen atmosphere in TGA of the neat PBA-a, was determined to be 334°C. The T_d values at 5% weight loss of the all sort of PBA-a:isomeric biphenyltetracarboxylic dianhydrides copolymer films were higher than that of the neat PBA-a films, i.e., 379°C for PBA-a:a-BPDA, 365°C for PBA-a:i-BPDA, and 402°C for PBA-a:s-BPDA. This is due to the effect of the ester carbonyl linkage formation in the PBA-a copolymer network as the T_d of polyester reported ~353–550°C [40, 41] which had higher thermal stability than that of the neat PBA-a. In addition, the improved crosslink density of the PBA-a with an addition of the isomeric biphenyltetracarboxylic dianhydrides via esterification reaction between the hydroxyl group of the polybenzoxazine and the anhydride group of the isomeric dianhydrides as mentioned previously as well as additional hydrogen bonding between –OH group and C=O group in the copolymers. Moreover, we can see that T_d at 5% weight loss in TGA falls in the same order as T_g: i.e., T_d at 5% weight loss of the PBA-a copolymers with respect to the structure of isomeric biphenyltetracarboxylic dianhydride component increases in the order of i-BPDA < a-BPDA < s-BPDA which shows the similar trend in polyimides based on isomeric biphenyltetracarboxylic dianhydrides [42]. Interestingly, T_g-thermal energy absorption relationship shows that the molecular chain with greater mobility or lower T_g may absorb more thermal energy and less thermal stability than a chain with less mobility.

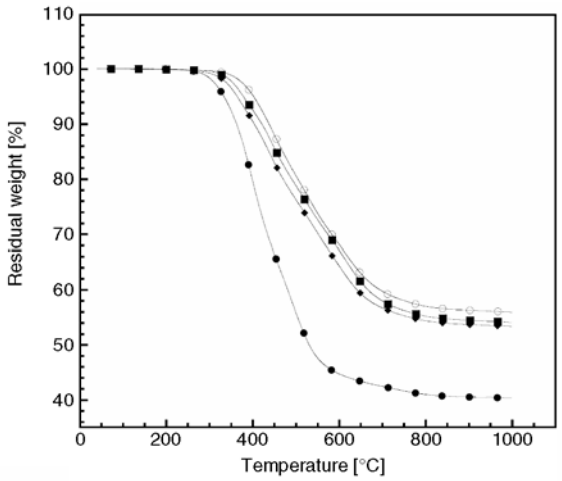

Figure 8. TGA thermograms of isomeric biphenyltetracarboxylic dianhydrides-modified PBA-a films of BA-a:BPDA = 1.5:1 mole: (●) PBA-a, (■) PBA-a:a-BPDA, (◆) PBA-a:i-BPDA, (○) PBA-a:s-BPDA

Additionally, the amount of carbonized residue (char yield) at 800°C under nitrogen for the PBA-a and all kind of the PBA-a:isomeric biphenyltetracarboxylic dianhydride copolymer films also showed in Figure 8. Their PBA-a:isomeric biphenyltetracarboxylic dianhydride copolymer films were 54, 55 and 60% for i-BPDA, a-BPDA, and s-BPDA-modified PBA-a, respectively, which was much great than that of the neat PBA-a (i.e. 38% at 800°C). The high char yield of these PBA-a copolymers due to their higher aromatic content in the molecular structure and enhanced crosslink density through inter hydrogen bonding in the copolymers of the resulting PBA-a copolymers as previously reported in [16].

4. Conclusions

High temperature bisphenol-A-aniline type polybenzoxazine (PBA-a) copolymer films were prepared from mixtures of BA-a resin and a-BPDA, i-BPDA, or s-BPDA isomeric biphenyltetracarboxylic dianhydrides. The obtained network structures were due to reaction between the hydroxyl group of polybenzoxazine and the anhydride group of isomeric biphenyltetracarboxylic dianhydrides. The T_g value, crosslink density, and T_d value of PBA-a was enhanced by blending with the isomeric biphenylte-

tracarboxylic dianhydrides. Moreover, T_g and T_d values of polybenzoxazine copolymers with respect to the structure of isomeric aromatic carboxylic dianhydride were as follow: PBA-a:s-BPDA > PBA-a:a-BPDA > PBA-a:i-BPDA. The char yield of their copolymer films at 800°C under nitrogen is much higher than that of the neat polybenzoxazine. Therefore, the polybenzoxazine modified with the isomeric biphenyltetracarboxylic dianhydrides should be considered as good potential candidates for high-temperature resistant materials with outstanding mechanical integrity at high temperatures.

Acknowledgements

This research is supported by the Rachadaphiseksomphot Endowment Fund Part of the "Strengthen CU's Researcher's Project," and the Higher Education Research Promotion and National Research University Project of Thailand, Office of the Higher Education Commission (AM1076A). Additional fund was also provided by Research Grants of Faculty of Engineering and Research Grants of Graduate School, Srinakharinwirot University 2011 (C. Jubsilp). The authors would like to acknowledge Prof. Rikio Yokota of JAXA, Japan for the research fellowship of S.R. Bisphenol A is kindly provided by Thai Polycarbonate Co., Ltd. (TPCC).

References

[1] Ishida H.: Handbook of benzoxazine resins. Elsevier, New York (2011).

[2] Ghosh N. N., Kiskan B., Yagci Y.: Polybenzoxazines – New high performance thermosetting resins: Synthesis and properties. Progress in Polymer Science, **32**, 1344–1391 (2007).
DOI: 10.1016/j.progpolymsci.2007.07.002

[3] Santhosh Kumar K. S., Reghunadhan Nair C. P.: Polybenzoxazines: Chemistry and properties. Rapra, Shawbury (2010).

[4] Reghunadhan Nair C. P.: Advances in addition-cure phenolic resins. Progress in Polymer Science, **29**, 401–498 (2004).
DOI: 10.1016/j.progpolymsci.2004.01.004

[5] Cao G. P., Chen W. J., Wei J. J., Li W. T., Liu X. B.: Synthesis and characterization of a novel bisphthalonitrile containing benzoxazine. Express Polymer Letters, **8**, 512–518 (2007).
DOI: 10.3144/expresspolymlett.2007.73

[6] Ishida H., Low H. Y.: A study on the volumetric expansion of benzoxazine-based phenolic resin. Macromolecules, **30**, 1099–1106 (1997).
DOI: 10.1021/ma960539a

[7] Ishida H.: Process for preparation of benzoxazine compounds in solventless systems. U.S. Patent 5543516, USA (1996).

[8] Rimdusit S., Pirstpindvong S., Tanthapanichakoon W., Damrongsakkul S.: Toughening of polybenzoxazine by alloying with urethane prepolymer and flexible epoxy: A comparative study. Polymer Engineering and Science, **45**, 288–296 (2005).
DOI: 10.1002/pen.20273

[9] Jubsilp C., Takeichi T., Hiziroglu S., Rimdusit S.: Effect of resin compositions on microwave processing and thermophysical properties of benzoxazine-epoxy-phenolic ternary systems filled with silicon carbide (SiC) whisker. Polymer Engineering and Science, **49**, 1022–1029 (2009).
DOI: 10.1002/pen.21358

[10] Grishchuk S., Mbhele Z., Schmitt S., Karger-Kocsis J.: Structure, thermal and fracture mechanical properties of benzoxazine-modified amine-cured DGEBA epoxy resins. Express Polymer Letters, **3**, 273–282 (2011).
DOI: 10.3144/expresspolymlett.2011.27

[11] Kimura H., Ohtsuka K., Matsumoto A.: Curing reaction of bisphenol-A based benzoxazine with cyanate ester resin and the properties of the cured thermosetting resin. Express Polymer Letters, **5**, 1113–1122 (2011).
DOI: 10.3144/expresspolymlett.2011.108

[12] Rimdusit S., Kunopast P., Dueramae I.: Thermomechanical properties of arylamine-based benzoxazine resins alloyed with epoxy resin. Polymer Engineering and Science, **51**, 1797–1807 (2011).
DOI: 10.1002/pen.21969

[13] Rimdutsit S., Bangsen W., Kasemsiri P.: Chemorheology and thermomechanical characteristics of benzoxazine-urethane copolymers. Journal of Applied Polymer Science, **121**, 3669–3678 (2011).
DOI: 10.1002/app.34170

[14] Tiptipakorn S., Damrongsakkul S., Ando S., Hemvichain K., Rimdusit S.: Thermal degradation behaviors of polybenzoxazine and silicon-containing polyimide blends. Polymer Degradation and Stability, **92**, 1265–1278 (2007).
DOI: 10.1016/j.polymdegradstab.2007.03.021

[15] Takeichi T., Guo Y., Rimdusit S.: Performance improvement of polybenzoxazine by alloying with polyimide: Effect of preparation method on the properties. Polymer, **46**, 4909–4916 (2005).
DOI: 10.1016/j.polymer.2005.03.096

[16] Jubsilp C., Takeichi T., Rimdusit S.: Property enhancement of polybenzoxazine modified with dianhydride. Polymer Degradation and Stability, **96**, 1047–1053 (2011).
DOI: 10.1016/j.polymdegradstab.2011.03.021

[17] Rimdusit S., Jubsilp C.: Polymer from modification of polybenzoxazine with anhydride. Thailand Patent 0701003695, Thailand (2007).

[18] Rajput A. B., Ghosh N. N.: Preparation and characterization of novel polybenzoxazine–polyester resin blends. International Journal of Polymeric Materials, **60**, 27–39 (2010).
DOI: 10.1080/00914037.2010.504153

[19] Spontón M., Ronda J. C., Galià M., Cádiz V.: Studies on thermal and flame retardant behaviour of mixtures of bis(*m*-aminophenyl)methylphosphine oxide based benzoxazine and glycidylether or benzoxazine of bisphenol A. Polymer Degradation and Stability, **93**, 2158–2165 (2008). DOI: 10.1016/j.polymdegradstab.2008.08.004

[20] Zhou H., Chen C., Kanbara R., Sasaki T., Yokota R.: Synthesis and properties of copolyimides derived from isometric biphenyltetracarboxylic dianhydrides (a-BPDA and i-BPDA) and oxydiphthalic dianhydride (ODPA) with 4,4′-oxydianiline (4,4′-ODA). High Performance Polymer, **17**, 213–224 (2005). DOI: 10.1177/0954008305044856

[21] Tong Y., Huang W., Luo J., Ding M.: Synthesis and properties of aromatic polyimides derived from 2,2′,3,3′-biphenyltetracarboxylic dianhydride. Journal of Polymer Science Part A: Polymer Chemistry, **37**, 1425–1433 (1999). DOI: 10.1002/(SICI)1099-0518(19990515)37:10<1425::AID-POLA4>3.0.CO;2-G

[22] Hergenrother P. M., Watson K. A., Smith Jr J. G., Connell J. W., Yokota R.: Polyimides from 2,3,3′,4′-biphenyltetracarboxylic dianhydride and aromatic diamines. Polymer, **43**, 5077–5093 (2002). DOI: 10.1016/S0032-3861(02)00362-2

[23] Liu C., Shen D., Sebastián R. M., Marquet J., Schönfeld R.: Mechanistic studies on ring-opening polymerization of benzoxazines: A mechanistically based catalyst design. Macromolecules, **44**, 4616–4622 (2011). DOI: 10.1021/ma2007893

[24] Gerber M. K., Pratt J. R., St Clair T. L.: Materials, chemistry, and characterization. in 'Polyimide' (eds.: Feger C., Khojasteh M. M., MacGrath J. M.) Elsevier, Amsterdam, 487–496 (1989).

[25] Stuart B. H.: Infrared spectroscopy: Fundamentals and applications. Wiley, Chichester (2004).

[26] Dunkers J., Zarate E. A., Ishida H.: Crystal structure and hydrogen-bonding characteristics of *N,N*-bis(3,5-dimethyl-2-hydroxybenzyl)methylamine, A benzoxazine dimer. The Journal of Physical Chemistry, **100**, 13514–13520 (1996). DOI: 10.1021/jp961293e

[27] Settle F. A.: Handbook of instrumental techniques for analytical chemistry. Prentice Hall, New Jersey (1997).

[28] Colthup N. B., Daly L. H., Wiberley S. E.: Introduction to infrared and raman spectroscopy. Academic Press, London (1990).

[29] Trappe V., Burchard W., Steinmann B.: Anhydride-cured epoxies via chain reaction. 1. The phenyl glycidyl ether/phthalic acid anhydride system. Macromolecules, **24**, 4738–4744 (1991). DOI: 10.1021/ma00017a002

[30] Jain R., Choudhary V., Narula A. K.: Curing and thermal behavior of DGEBA in presence of dianhydrides and aromatic diamine. Journal of Applied Polymer Science, **105**, 3804–3808 (2007). DOI: 10.1002/app.26620

[31] Rocks J., Rintoul L., Vohwinkel F., George G.: The kinetics and mechanism of cure of an amino-glycidyl epoxy resin by a co-anhydride as studied by FT-Raman spectroscopy. Polymer, **45**, 6799–6711 (2004). DOI: 10.1016/j.polymer.2004.07.066

[32] Ghaemy M., Riahy M. H.: Kinetics of anhydride and polyamide curing of bisphenol A-based diglycidyl ether using DSC. European Polymer Journal, **32**, 1207–1212 (1996). DOI: 10.1016/S0014-3057(96)00066-3

[33] Chiang W-Y., Chan S-C.: Preparation and properties of UV-autocurable BTDA-based epoxy-multiacrylate resins. Effects of the degree of polymerization and the epoxy type. Journal of Applied Polymer Science, **43**, 1827–1836 (1991). DOI: 10.1002/app.1991.070431006

[34] Nielsen L. E.: Cross-linking–effect on physical properties of polymers. Journal of Macromolecular Science Part C: Polymer Reviews, **3**, 69–103 (1969). DOI: 10.1080/15583726908545897

[35] Fryd M.: Structure–Tg relationship in polyimides. in 'Polyimides: Synthesis, characterizations and properties' (ed.: Mittal K. L.) Plenum Press, New York, Vol 1, 377–383 (1984).

[36] Ding M.: Isomeric polyimides. Progress in Polymer Science, **32**, 623–668 (2007). DOI: 10.1016/j.progpolymsci.2007.01.007

[37] Hasegawa M., Sensui N., Shindo Y., Yokota R.: Structure and properties of novel asymmetric biphenyl type polyimides. Homo- and copolymers and blends. Macromolecules, **32**, 387–396 (1999). DOI: 10.1021/ma9808629

[38] Li F., Ge J. J., Honigfort P. S., Fang S., Chen J-C., Harris F. W., Cheng S. Z. D.: Dianhydride architectural effects on the relaxation behaviors and thermal and optical properties of organo-soluble aromatic polyimide films. Polymer, **40**, 4987–5002 (1999). DOI: 10.1016/S0032-3861(98)00721-6

[39] Hergenrother P. M.: High performance polymers and composites. Wiley, New York (1991).

[40] Evans S. J., Haines P. J., Skinner G. A.: The thermal degradation of polyester resins II. The effects of cure and of fillers on degradation. Thermochimica Acta, **291**, 43–49 (1997). DOI: 10.1016/S0040-6031(96)03102-4

[41] Sato H., Kikuchi T., Koide N., Furuya K.: Thermal degradation and combustion process of liquid crystalline polyesters studied by directly coupled thermal analysis-mass spectrometry. Journal of Analytical and Applied Pyrolysis, **37**, 173–183 (1996). DOI: 10.1016/0165-2370(96)00944-8

[42] Inoue H., Okamoto H., Hiraoka Y.: Effect of the chemical structure of acid dianhydride in the skeleton on the thermal property and radiation resistance of polyimide. International Journal of Radiation Applications and Instrumentation Part C: Radiation Physics and Chemistry, **29**, 283–288 (1987). DOI: 10.1016/1359-0197(87)90033-6

eXPRESS Polymer Letters Vol.6, No.10 (2012) 783–793
Available online at www.expresspolymlett.com
DOI: 10.3144/expresspolymlett.2012.84

Preparation and thermal properties of mesoporous silica/phenolic resin nanocomposites via *in situ* polymerization

C. B. Yu[1,2], *C. Wei*[1*], *J. Lv*[1], *H. X. Liu*[1], *L. T. Meng*[1]

[1]Key Laboratory of New Processing Technology for Nonferrous Metals & Materials Ministry of Education, and School of Materials Science and Engineering, Guilin University of Technology, 541004 Guilin, China
[2]College of Chemistry and Chemical Engineering, Guangxi University, 530004 Nanning, China

Received 21 February 2012; accepted in revised form 29 April 2012

Abstract. In order to enhance the adhesion between inorganic particles and polymer matrix, in this paper, the mesoporous silica SBA-15 material was synthesized by the sol-gel method. The surface of SBA-15 was modified using γ-glycidyloxypropyltrimethoxysilane (GOTMS) as a coupling agent, and then mesoporous silica/phenolic resin (SBA-15/PF) nanocomposites were prepared via *in situ* polymerization. The structural parameters and physical properties of SBA-15, SBA-15-GOTMS (SBA-15 surface treated using GOTMS as coupling agents) and E-SBA-15/PF (SBA-15/PF nanocomposites extracted using ethanol as solvent) were characterized by X-ray diffraction (XRD), N_2 adsorption-desorption, Fourier transform infrared spectroscopy (FTIR), scanning electron microscopy (SEM), transmission electron microscopy (TEM) and thermogravimetric analysis (TGA). The thermal properties of the nanocomposites were studied by differential scanning calorimetry (DSC) and thermogravimetric analysis (TGA). The results demonstrated that the GOTMS were successfully grafted onto the surface of SBA-15, and chemical bonds between PF and SBA-15-GOTMS were formed after *in situ* polymerization. In addition, it is found that the *in situ* polymerization method has great effects on the textural parameters of SBA-15. The results also showed that the glass transition temperatures and thermal stability of the PF nanocomposites were obviously enhanced as compared with the pure PF at silica contents between 1–3 wt%, due to the uniform dispersion of the modified SBA-15 in the matrix.

Keywords: *thermal properties, SBA-15, phenolic resin*

1. Introduction

Organic-inorganic hybrid materials, especially polymer matrix composites with inorganic nanoscale building blocks, have drawn the widespread attention of researchers owing to the promise of combining the superior mechanical and thermal properties of inorganic phases with the flexibility and processibility of organic polymers [1, 2]. The comprehensive performances of the composites depended on many factors, such as the intrinsic properties of the polymers, the processing technology of the composites, the dispersion of the nanoparticles in the polymer matrix, and the interfacial compatibility between nanoparticles and the polymer matrix [3]. Commonly used inorganic nanoscale additives include carbon nanotubes, nanoparticles, layered silicates and clays. Mesoporous molecular sieve, a new class of nanoscale materials which possess large specific surface areas and tunable pore sizes between 2 and 50 nm, have provided the possibility of incorporating diverse organic guest species into ordered mesoporous structures [4–5]. Although mesoporous molecular sieve have been widely stud-

*Corresponding author, e-mail: 1005668130@qq.com

ied as catalysts, absorbents, chemical sensing, and electronic device materials, using mesoporous molecular sieve as polymer additive attracted less attention [6–8]. Recently, mesoporous silica reinforced polymer composites have attracted considerable interests due to the possibility of improving the mechanical and thermal properties of polymers [9–17], and have even generated certain properties, for example, low dielectric constant [10, 12–14, 16, 17], low thermal expansion property [18–21], excellent friction and wear performance [22], and so on. It is a key factor that the incorporation of guest-monomer or polymer into the channels of mesoporous materials contributed to the dispersion of the additives in polymer matrix and the advancement of the properties of as-prepared composites. Run *et al.* [3] reported the preparation of MCM-48/PMMA composites by injecting MMA monomers into the mesoporous particles under high temperature and low pressure. They found that the physical properties and thermal stability of MCM-48/PMMA composites were improved significantly with the increase of the content of MCM-48.

Phenolic resins (PF), classified as resol and novolac by synthetic conditions and curing mechanism, are important technical materials and are irreplaceable in many areas, especially in thermal insulation, coating, adhesive, aeronautic utilities, and composite materials, because of their excellent thermal stability, high char yield, and good solvent resistance, etc [23]. The rapid growth of PF applications requires extensive research to improve their comprehensive properties. Moreover, it is demonstrated that many properties of PF can be easily improved by preparing PF composites [24]. Recently, researchers tried to prepare the PF nanocomposites by addition of nanoscale materials, including carbon naotubes [25, 26], expanded graphite [23] and layered silicates [27, 28]. There is a considerable amount of literature on the preparation and properties of polymer-mesoporous silica nanocomposites by using epoxy [10–13, 18, 22] and polyolefin resins [3, 6, 7] as polymer matrix. However, there are still few reports about the composite materials based on PF and mesoporous silica. In addition, though the researchers have paid much attention to the properties of the nanocomposites, systematic studies of structural variations of mesoporous silica in the process of the nanocomposites preparation have been rarely reported.

In this study, the novel SBA-15/PF composites were prepared via *in situ* condensation polymerization of phenol and formaldehyde in the presence of SBA-15. The mesoporous silica SBA-15 with large surface area, uniform hexagonal channels, large pore sizes and pore volume was synthesized by sol-gel method. In order to improve the interface compatibility between SBA-15 and PF matrix, surface modification of SBA-15 by coupling agent was conducted. Then, the modified SBA-15 was dispersed in phenol monomer by ultrasonic irradiation before polymerization. The structure of the SBA-15 by surface treatment and *in situ* polymerization methods and the effects of SBA-15 loading on the thermal properties of SBA-15/PF nanocomposites were investigated in detail.

2. Experimental

2.1. Materials

$EO_{20}PO_{70}EO_{20}$ (where EO stands for ethylene oxide, PO for propylene oxide, Pluronic P123) was commercially obtained from Sigma-Aldrich Co., Ltd. (USA). Tetraethoxysilane (TEOS) used as silica source and γ-glycidyloxypropyltrimethoxysilane (GOTMS) used as coupling agent were purchased from Aladdin Chemistry Co. Ltd. (Shanghai, China). Phenol and formaldehyde monomers were ordered from Xilong Chemical Co. Ltd. (Guangdong, China). Oxalic acid was purchased from Shanghai Chemical Reagent Company (Shanghai, China) and used as catalytic agent. All chemicals were of reagent-grade and used as received without further purification.

2.2. Synthesis of mesoporous silica materials

Mesoporous silica materials, SBA-15, was firstly synthesized by templating with the $EO_{20}PO_{70}EO_{20}$ triblock copolymers via a sol-gel process according to literature [29, 30]. Typically, 2 g of Pluronic P123 and 37 wt% HCl solution (10 mL) were dissolved in deionized water (80 g) with stirring at 35°C for 6 h. Then 4.2 g of TEOS was dropped into the homogenous clear solution with stirring at 35°C for 24 h. After that, the solution was then removed to an autoclave and hydrothermally treated by putting in a 100°C oven for another 24 h. The obtained par-

ticles were collected by filtration, washed 3times with deionized water, and dried at 60°C in air. The resulting products were calcined at 550 C for 6 h to remove the template.

2.3. Preparation of organically modified SBA-15 (SBA-15-GOTMS)

The typical procedure for the preparation of organically modified SBA-15 is described as follows: the SBA-15 was dispersed in toluene under ultrasonic irradiation and stirring for 30 min, and then the calculated amount of GOTMS was added to the mixture. The weight ratio between SBA-15 and GOTMS was 5:1. The mixture was refluxed at 120°C for 6 h under vigorous stirring. After the mixture was filtrated with Buchner funnel, the product was washed several times using acetone and dried in the vacuum oven at 60°C.

2.4. Preparation of SBA-15/PF nanocomposites

The SBA-15-GOTMS was first dispersed in phenol by ultrasonic irradiation and high temperature and high pressure treatment. In a typical procedure, the calculated amount of SBA-15-GOTMS was dispersed in phenol by ultrasonic irradiation in a beaker at 50°C for 1 h. Subsequently, the mixture was transferred into an autoclave, sealing reactor, then put it into an oven at 200°C for 12 h, following by natural cooling and reserve.

The novolac-type phenolic nanocomposites were synthesized in a 250 mL three-necked reactor equipped with a reflux condenser, stainless-steel stirrer, and thermometer. The reagents, phenol containing SBA-15, formaldehyde (in 37 wt% water solution) (P: F molar ratio = 1.15:1) and oxalic acid (2 wt% of phenol), were fed into a flask reactor. The mixture was first stirred under 85°C for 5 h in water bath, and then keep on reacting in order to remove the water and free phenol at 160–180°C for an additional 1 h under 0.03–0.05 MPa pressure. When Weissenberg effect was observed, SBA-15/PF nanocomposite was prepared [31]. The final products, i.e. SBA-15/PF nanocomposites which included various SBA-15 additives from 0 to 3 wt% were prepared as well.

2.5. Preparation of E-SBA-15/PF hybrid materials

SBA-15/PF nanocomposite containing 3 wt% SBA-15, was dissolved in a large volume of ethanol in a glass flask. The mixture was refluxed at 60°C for 12 h under stirring, and then centrifugal separated and washed for several times to remove most of the polymer from the external surface of the SBA-15 particles, and the residual sample named as E-SBA-15/PF (extracted SBA-15/PF) was dried in vacuum at 80°C for 6h before analyses [3]. Following the E-SBA-15/PF was calcined at 500°C for 6 h to remove most of the organic compounds, the as-prepared powder materials were named after CE-SBA-15/PF. The experiment details of the process of hybrid materials are shown in Figure 1.

2.6. Characterization

X-ray powder diffraction (XRD) was carried out with a PANalytical X′Pert PRO X-ray Diffractometer (Holland). The X-ray beam was nickel-filtered Cu-Kα radiation (λ = 0.154 nm), the diffraction patterns being collected in the 2θ range 0.5–8.0° at a scanning rate of 0.2°/min. N_2 adsorption-desorption isotherms were obtained at 77 K using a Quantachrome NOVA 1200e gas-adsorption analyzer (USA). Before the adsorption measurements, all samples were outgassed for 12 h at 353 K in the degas port of the adsorption analyzer. The average pore radius and pore volume were determined by applying the BJH (Barrett, Joyner and Halenda) method. The specific surface area was calculated

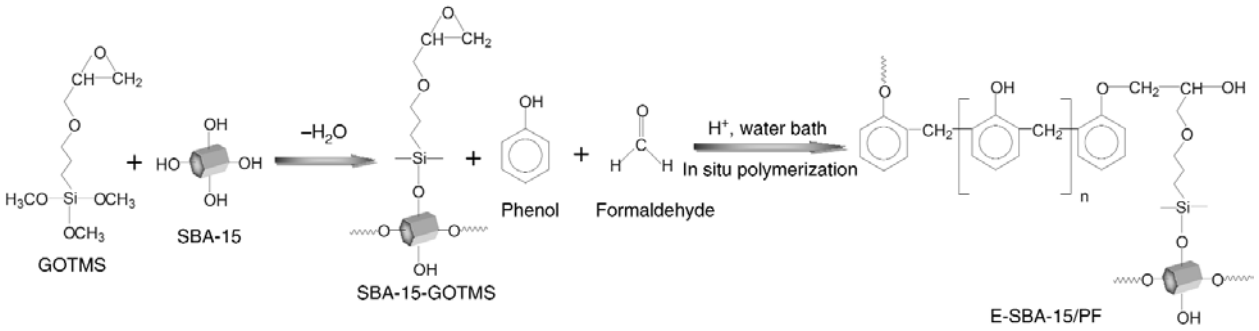

Figure 1. Scheme of possible reaction of the surface modification and in-situ polymerization

using the BET (Brunauer, Emmet and Teller) model. Fourier-transform infrared spectroscopy (FTIR) spectra were recorded using a Nexus-470 FTIR spectrometer (Nicolet, USA), and the sample powder was pressed into a pellet with KBr. Differential scanning calorimetry (DSC) was performed with DSC 204 (NETZSCH, Germany) between 10 and 100°C at a heating rate of 10°C/min under a nitrogen atmosphere. Thermogravimetric analysis (TGA) was carried out on a STA 449C analyzer (NETZSCH, Germany) at a heating rate of 10°C/min from 50 to 800°C under a nitrogen atmosphere. Scanning electron microscopy (SEM) observation was conducted with a JSM-6380 LV microscope (Japan) operating at 5 kV. Samples were sputter coated with a thin carbon layer under vacuum situation. Energy dispersive X-ray (EDX) spectroscopy image of the silicon element mapping was recorded using S-4800 scanning electron microscope (Hitachi, Japan). Transmission electron microscopy (TEM) was taken on JEM-2100 electron microscope (JEOL, Japan) operating at 120 kV. The sample powders were dispersed in ethanol under sonication, and then an aliquot was put on a copper grid and the solvent was evaporated in an oven.

3. Results and discussion

3.1. Characterization of the surface modified SBA-15 and its nanocomposites

In order to improve the interfacial adhesion between the SBA-15 and the PF matrix, the surface modification of SBA-15 was carried out. In this study, the GOTMS was used as coupling agent, which is capable of linking SBA-15 covalently to the PF resin by silylation of the mesoporous silica [12]. Then, SBA-15/PF composites were prepared via *in situ* polymerization in the presence of SBA-15-GOTMS. The FTIR spectra of GOTMS, SBA-15 and SBA-15-GOTMS are illustrated in Figure 2a. It can be seen that the GOTMS shows two epoxy group characteristic peaks at 915 and 820 cm^{-1}, a weak O–CH_2 and CH_3 bending vibrations at 1465 cm^{-1} [32] and two peaks at 2960 and 2850 cm^{-1} corresponding to the asymmetric and symmetric stretching vibrations of C–H in –CH_2 and –CH_3, respectively. For unmodified SBA-15, a wide absorption peak at around 3450 cm^{-1} and a weak peak at 965 cm^{-1} may be assigned to Si–OH stretching and bending vibrations, a strong absorption peak at 1082 cm^{-1} and a weak peak at 798 cm^{-1} associated with Si–O–Si asymmetric and symmetric stretching vibrations can be observed, respectively. However, the surface modified mesoporous silica materials (SBA-15-GOTMS) possess many characteristic absorption peaks derived from SBA-15 and GOTMS. It can be clearly seen that both Si–O–Si and Si–OH characteristic absorption peaks are kept, and the epoxy group peak at 915 and 820 cm^{-1} are overlapped by a series of intensive peaks at 798–1082 cm^{-1} which belong to Si–O–Si and Si–OH [12]. Additionally, the adsorptions peak shifts from 2960 to 2930 cm^{-1}, which can be attributed to asymmetric stretching vibrations of C–H, and it implies the –CH_3 is absent in the SBA-15-GOTMS. All these results suggest that the GOTMS has been attached to the surface of SBA-15 through condensation between the silanol groups of hydrolyzed GOTMS and SBA-15. Figure 2b shows the FTIR spectra of PF, SBA-15-GOTMS and E-SBA-15/PF hybrid materials. The E-SBA-15/PF exhibit many characteristic absorp-

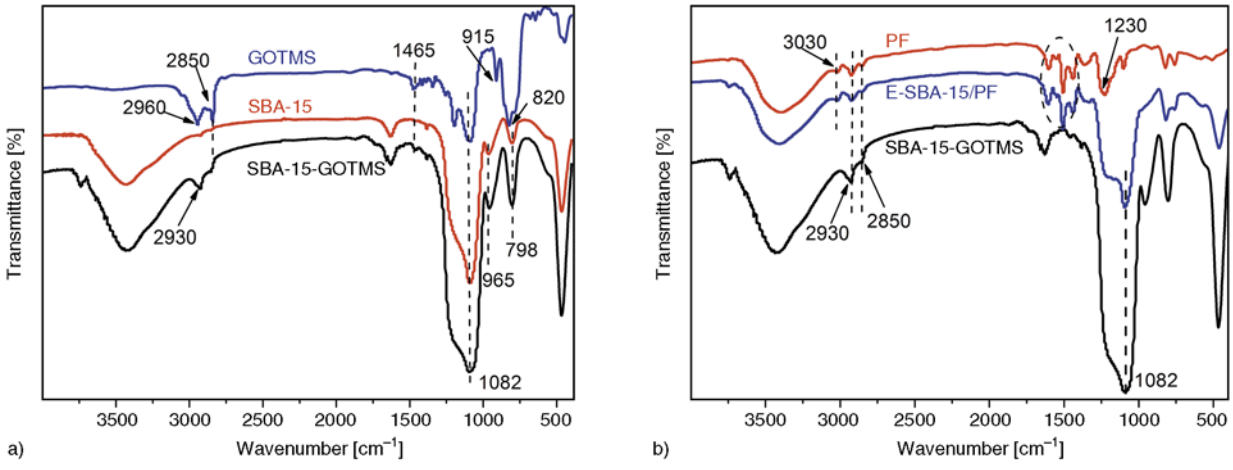

Figure 2. FTIR spectra of GOTM, SBA-15, and SBA-15-GOTMS (a), PF, SBA-15-GOTMS and E- SBA-15/PF (b)

tion peaks both of PF and SBA-15-GOTMS. Among them, the peaks at 1400–1600 cm^{-1}, corresponding to the phenyl rings, and 3030 cm^{-1}, corresponding to C–H stretching vibration of phenyl rings, are presented in the E-SBA-15/PF hybrid materials as well as pure PF. A strong absorption peak at 1082 cm^{-1} is attributed to the Si–O–Si stretch vibration appears in the FTIR spectra of the SBA-15-GOTMS and E-SBA-15/PF hybrid materials. But the peak at 1230 cm^{-1}, corresponding to stretching vibration of phenolic C–O–C [33], is overlapped by an intensive peak at 1000–1300 cm^{-1} belonging to the Si–O–Si characteristic peak. The results demonstrate that SBA-15-GOTMS has been covalently bonded with PF chain during *in situ* polymerization. The presence of covalent conjugation could improve the interfacial adhesion between SBA-15-GOTMS and PF.

The nitrogen adsorption-desorption isotherms along with the corresponding pore-size distribution curves of SBA-15, SBA-15-GOTMS and E-SBA-15/PF are shown in Figure 3. The SBA-15 exhibits a classical Langmuir IV-type isotherm with H_1 type vertical hysteresis loop, and the capillary condensation occurs at a high relative pressure, which is conformable to the literature [29]. In addition, the H_1 type hysteresis loop of the SBA-15 is relatively wide. We think this may be caused by a wide distribution of the pore volume SBA-15. The curves of SBA-15-GOTMS and E-SBA-15/PR show rarely adsorption steps and H_1 type hysteresis loop (Figure 3a), and the pore volumes decreased from 1 to 0.71 and 0.04 $cm^3 \cdot g^{-1}$, respectively. The detailed structural parameters of the SBA-15 and its hybrid materials are listed in Table 1. The results indicate that GOTMS has been conjugated to SBA-15 by chemical bond, and the condensation polymerization of PF has been successfully carried out inside the channels of SBA-15, leading to occupation most of channel space of SBA-15. Therefore, the pore volume of E-SBA-15/PF is very small after the polymerization. Moreover, the three samples exhibited great differences of the distribution of pore size. The distribution of pore size of SBA-15-GOTMS and E-SBA-15/PF are broader than that of SBA-15 (Figure 3b), which may be attributed to the fact that the mesoporous channels were plugged up in various extents after the coupled treatment and polymerization occurred [4, 34]. On the other hand, this also indicated the successful reaction within the channels of SBA-15.

Table 1. Textural parameters of SBA-15, SBA-15-GOTMS and E-SBA-15 /PF

Material	BET Surface area [m^2/g]	Total pore volume [cm^3/g]	Average pore diameter [nm]
SBA-15	707	1.00	6.6
SBA-15-GOTMS	619	0.71	2.0
E-SBA-15 /PF	46	0.04	1.6

Figure 4 shows the XRD patterns of mesostructure silica. There are three well-defined peaks at 2θ values between 0.5 and 8° which can be indexed as (100), (110), and (200) Bragg reflections, suggested the typical hexagonal (p6mm) SBA-15 [30]. After treating SBA-15 by GOTMS, the XRD pattern of the resulted SBA-15-GOTMS shows the p6mm structural feature as well, although the diffraction peaks increased slightly in 2θ values. The three characteristic XRD peaks of SBA-15-GOTMS can still be observed after treatment by coupling agent, demonstrate that hexagonal SBA-15 was undam-

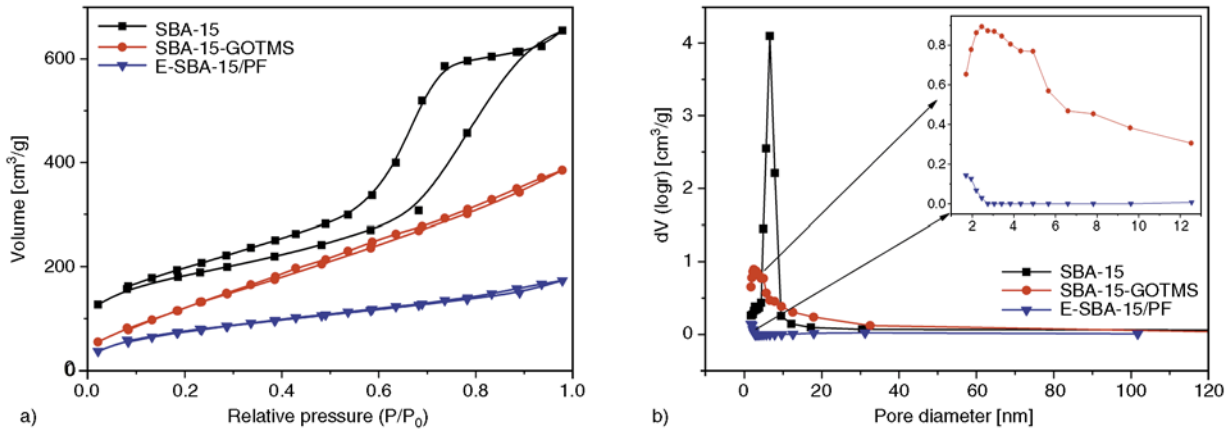

Figure 3. Nitrogen sorption isotherms (a) and pore diameter distribution (b) of SBA-15, SBA-15-GOTMS and E-SBA-15/PF

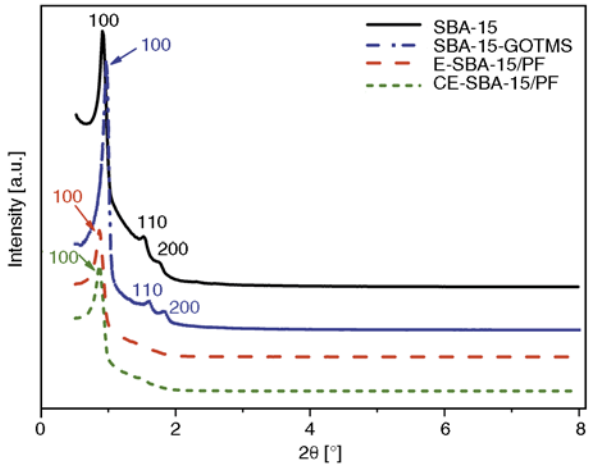

Figure 4. X-ray powder diffraction of SBA-15, SBA-15-GOTMS, E-SBA-15/PF and CE-SBA-15/PF

aged. From the XRD pattern of E-SBA-15/PF and CE-SBA-15/PF, we can see that the intensity of (100) diffraction peak was distinctly decreased, meanwhile the peaks at higher angles are not observed, suggesting that the ordered structure of SBA-15 has been little changed in short-range but great changed in long-range. This may be explained by the following reasons: the SBA-15 were uniformly dispersed throughout the polymer matrix during the *in situ* polymerization process, and meanwhile interpenetrating organic-inorganic network structure may be formed, leading to the decrease of long range regularity of SBA-15.

Thermogravimetric analysis (TGA) curves of SBA-15, SBA-15-GOTMS, PF and E-SBA-15/PF are shown in Figure 5. It can be seen that only 1.8 wt% weight loss was found for unmodified SBA-15 below 800°C, while 13.48 and 34.02 wt% weight loss were observed between 50–800°C for SBA-15-GOTMS and E-SBA-15/PF, respectively. All these

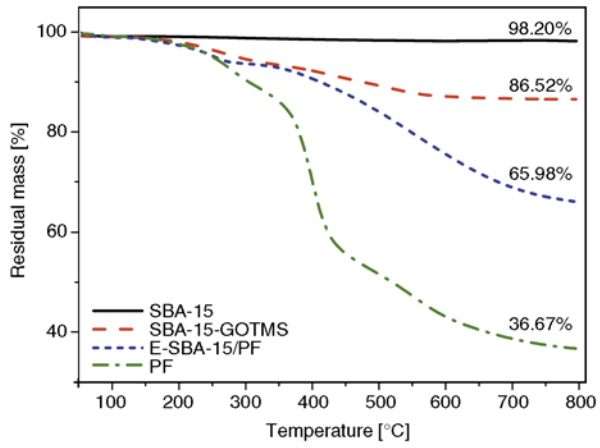

Figure 5. TGA thermograms of SBA-15, SBA-15-GOTMS, PF and E-SBA-15/PF

results demonstrate that the GOTMS has been successfully grafted onto the surface of the SBA-15 and the chemical reaction has occurred between SBA-15-GOTMS and PF resin via *in situ* polymerization. From the TGA curves, the reacting masses of GOTMS grafted onto SBA-15 can be approximately calculated, which is 11.68 wt%. Taking into consideration that the carbon residue of PF is up to 36.67 wt% at 800°C, the masses of PF reacted with SBA-15-GOTMS (RMp) during *in situ* polymerization can be estimated using the Equation (1) [35]:

$$RM_p = \frac{W_{SBA-15-GOTMS,T} - W_{E-SBA-15/PF,T}}{1 - W_{PF,T}} \quad (1)$$

where RM_p is the masses of PF reacted with SBA-15-GOTMS by *in situ* polymerization; $W_{PF,T}$, $W_{SBA-15-GOTMS,T}$ and $W_{E-SBA-15/PF,T}$ are the residual weight percent of PF, SBA-15-GOTMS and E-SBA-15/PF, respectively, at temperature T. The value of RM_p was 32.43 wt% of SBA-15 according to the Equation (1). Meanwhile, it could be seen from the TGA curves of E-SBA-15/PF that a platform arose at 250–350°C as compared with PF, suggested that the thermal stability of E-SBA-15/PF was greatly enhanced, which confirmed that there was a strong interaction between SBA-15-GOTMS and PF resin.

3.2. Morphology

Figure 6 shows the SEM micrographs of the SBA-15, SBA-15-GOTMS and E-SBA-15/PF. It can be clearly observed that the SBA-15 consist of many rope-like shapes with relatively uniform sizes of 1–2 μm, which are aggregated each other and form clusters. The morphology characteristic of SBA-15 is well in accordance with previous literature [29]. After surface modification, SBA-15-GOTMS shows the similar particle morphology as SBA-15, suggested the high stability of ordered structure of SBA-15. Figure 6c shows the SEM image of E-SBA-15/PF (the extracted SBA-15/PF), which reveals that both the surface and interface of SBA-15 attached some PF resins but the SBA-15 could still be distinguished easily. Furthermore, the larger orderly agglomerates of the SBA-15 have been broken, and some holes among SBA-15 appeared resulting from the extracted PF matrix. The lose of orderly structure of the SBA-15 seen from the SEM image and the above XRD analysis may be attributed to

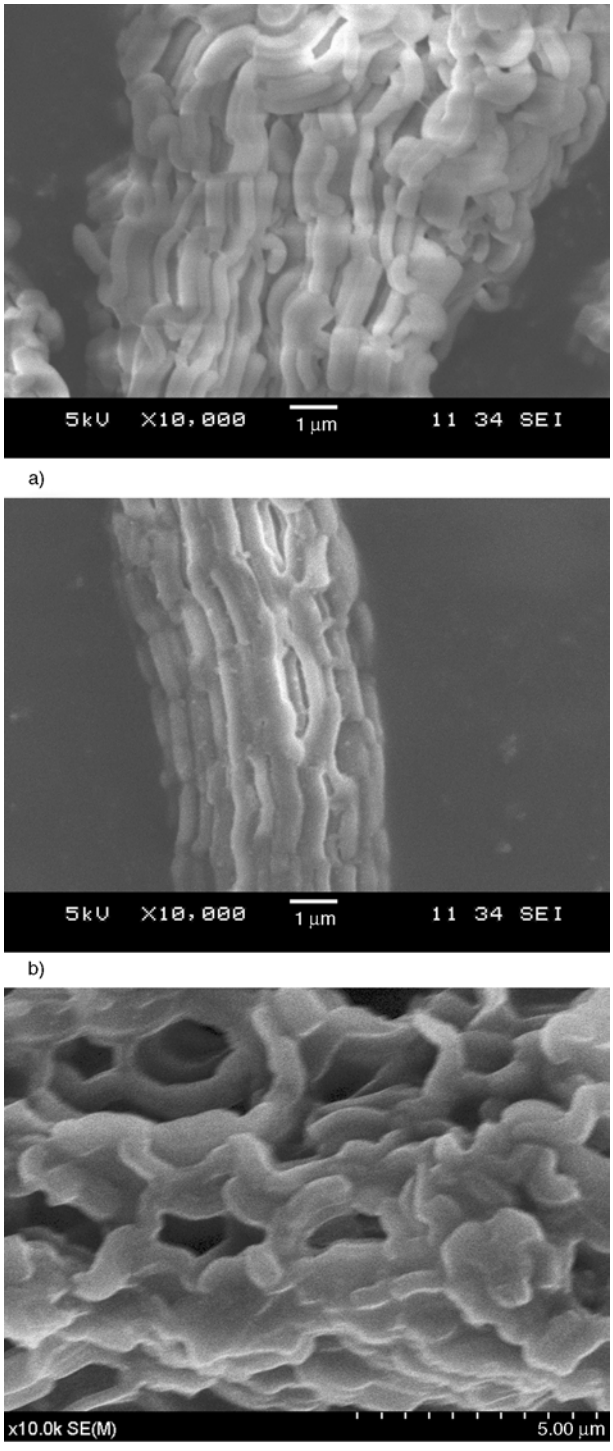

Figure 6. SEM images of SBA-15 (a), SBA-15-GOTMS (b) and E-SBA-15/PF (c)

the formation of chemical bonds Between SBA-15 and PF during *in situ* polymerization. This effect could contribute to the homogeneous dispersion of mesoporous silica in the PF matrix.

To further observe the variation of morphology of SBA-15 before and after *in situ* polymerization, the TEM images of the SBA-15 and CE-SBA-15/PF

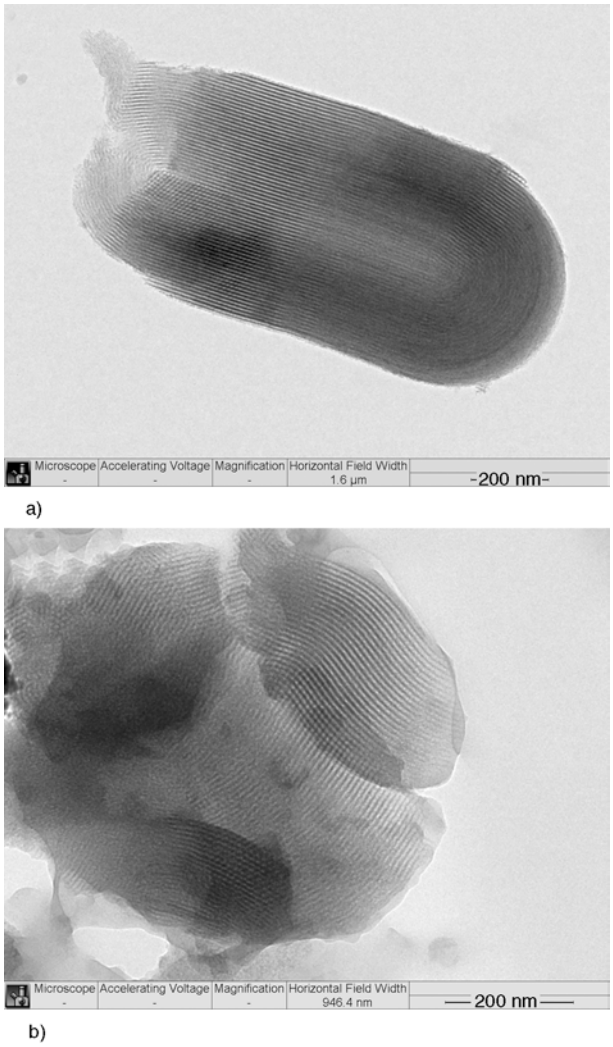

Figure 7. TEM images of the SBA-15 (a) and CE-SBA-15/PF (b) hybrid material

are presented as shown in Figure 7. The images of the SBA-15 show large domains of well-ordered structure with 1D channels, which are similar to results reported in literatures [29–30]. It can be seen from Figure 7b that the large domain regularity of CE-SBA-15/PF has decreased, and there are still the 1D channels of mesoporous materials in the relatively small domain, which is consistent with the XRD analysis. This results can further confirm that the effect of the *in situ* polymerization on the ordered structure of SBA-15.

In order to further study the dispersion of SBA-15 in the PF matrix, EDX mapping of SBA-15/PF composite materials were carried out. Figure 8 show Si mapping of SBA-15/PF composite materials with various contents of SBA-15. It can be clearly seen that lots of white spots associated with silicon atoms were uniformly distributed in black background

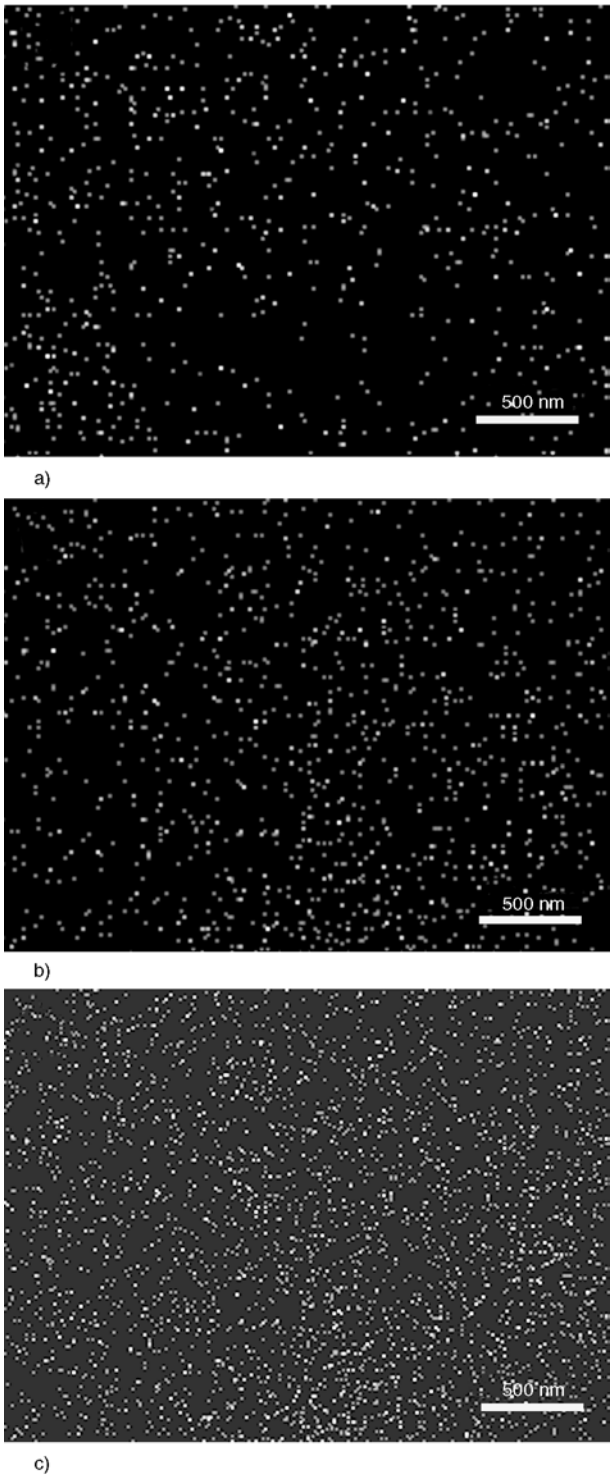

Figure 8. Si-mapping images studies of EDX on SBA-15/PF composites (a) 1%, (b) 2% and (c) 3%

associated with polymer matrix at ×20 000 magnification (scale bar = 500nm), indicating that the SBA-15 was well dispersed throughout the PF matrix. Moreover, with the increasing of SBA-15 content, the density of silicon atoms was distinctly increased.

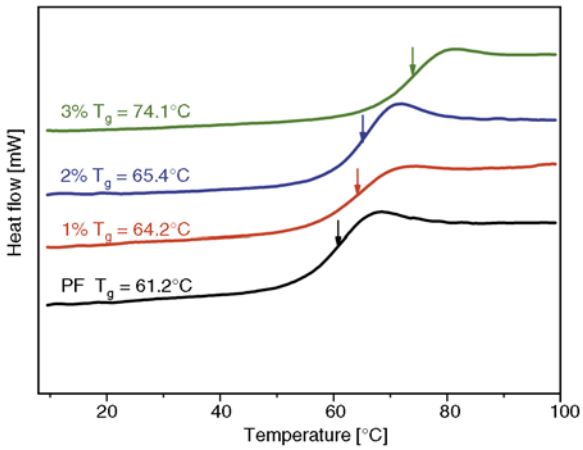

Figure 9. DSC curves and T_g values for PF and SBA-15/PF nanocomposites

3.3. Thermal properties

The thermal properties of polymer nanocomposites have drawn much attention because of the demand of many application fields of the nanocomposites. Furthermore, the improvement of the thermal properties of polymer nanocomposites can also demonstrate the uniform dispersion of fillers and the presence of intensive interactions between fillers and polymers to a certain extent. Figure 9 shows the variation of the glass transition temperature (T_g) with SBA-15 loading as determined by conventional DSC for the unmodified and modified PF. T_g of the pure PF is about 61.2°C, whereas all the SBA-15/PF nanocomposite show substantially higher T_g values than that of pure PF. Moreover, T_g of nanocomposites is enhanced with the increase of SBA-15 contents. It is worth noting that the T_g of the nanocomposite containing 3 wt% SBA-15 is increased by 12.9°C in contrast to pure PF. The significant enhancement of T_g may be attributed to the strong interactions between the polymer chains and SBA-15 which was formed by *in situ* polymerization. More importantly, the *in situ* polymerization of PF monomers within the pore channels of SBA-15, may trap some polymer chains or fractions. These interactions between PF and SBA-15 will impede the movement of polymer chains and result in the increases of T_g significantly with addition of SBA-15. Figure 10 and Table 2 show the results of the thermal stabilities of the SBA-15, pure PF and its nanocomposites by using TGA in the range of 50–800°C.

Table 2. Thermal stabilities of SBA-15, PF and SBA-15/PF nanocomposites

Material	$T_{d,5}$ [°C[	$T_{d,10}$ [°C[	Char yield at 800°C [wt%]
pure PF	263	312	37.7
SBA-15	–	–	98.2
1 wt% SBA-15/PF	266	317	39.1
2 wt% SBA-15/PF	279	337	42.0
3 wt% SBA-15/PF	364	380	49.7

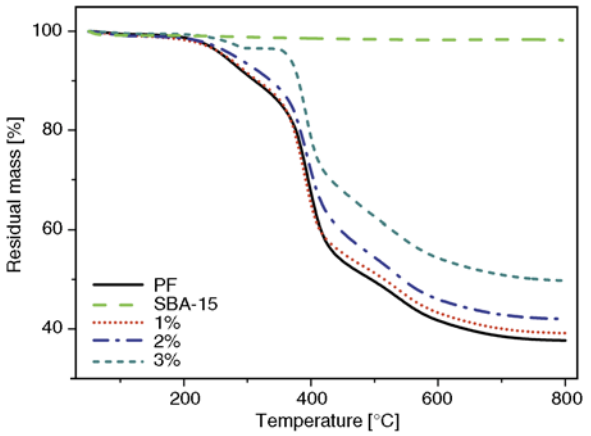

Figure 10. TGA curves of SBA-15, PF and SBA-15/PF nanocomposites

Thermal stabilities of the nanocomposites are expressed by their 5 and 10% weight loss decomposition temperatures, $T_{d,5}$ and $T_{d,10}$. As expected, the SBA-15/PF nanocomposites show better thermal stability than the pure PF. Moreover, the $T_{d,5}$ and $T_{d,10}$ of the nanocomposites increase with respect to the amount of SBA-15, for instance, the $T_{d,5}$ and $T_{d,10}$ of SBA-15/PF nanocomposites with 1 and 3 wt% SBA-15 increases from 263 and 312°C (neat PF) to 266 and 317°C (1 wt%) and 364 and 380°C (3 wt%), respectively. Meanwhile, for the TGA curves of SBA-15/PF nanocomposites with 3 wt% SBA-15 loading, a platform appeared in the range of 300–350°C. In addition, the char yield of the nanocomposites increased with the increase of SBA-15 content, and is higher than its SBA-15 content (Table 2), because the introduction of SBA-15 hindered the production of gaseous product and resulted in increase of the char retention. The obvious enhancement of the thermal stability of the nanocomposites can be attributed to the presence of strong interaction between SBA-15 and polymer matrix. The modified SBA-15 nanoparticles have abundant GOTMS on their surface and internal pore channel surface, and thus chemical bonding between the PF chains and SBA-15 can be formed after *in situ* polymerization. Hence, it's believed that PF chains not only bonded to the surface of the SBA-15, but also penetrated through the pore channel and were tethered to the channel surface. The favorable interaction leads to homogeneous disperse of SBA-15 in the PF matrix.

4. Conclusions

The PF nanocomposites containing SBA-15 type mesoporous silica modified by GOTMS have successfully been prepared via *in situ* polymerization. From the FTIR and TGA analysis, the GOTMS was chemically grafted onto the surface of SBA-15 and there were chemical reaction between SBA-15-GOTMS and PF chains during *in situ* polymerization. In addition, the variation of the textural parameters of SBA-15 was studied during the reaction process by XRD, N_2 adsorption-desorption, SEM, and TEM. The results show that both surface modification and *in situ* polymerization treatments have great influence on the textural parameters of SBA-15.

We also investigated the effect of SBA-15 loading on glass transition temperatures and thermal stability of the SBA-15/PF nanocomposites. With the increase of the SBA-15 content, the $T_{d,5}$, $T_{d,10}$ and T_g of PF nanocomposites were gradually improved as compared to that of the neat PF. It is especially exciting that the T_g and $T_{d,10}$ of the PF nanocomposites were increased by 12.9 and 68°C at 3 wt% SBA-15 loading, respectively. From the analysis of EDX mapping of SBA-15/PF composite materials, the uniform dispersion of the SBA-15 in the PF matrix may be the cause for the enhancement of thermal properties. Because of the excellent thermal properties of the new nanocomposites, it has great potential for friction composite materials and electronic packaging materials applications.

Acknowledgements

The authors would like to acknowledge National Natural Science Foundation of China (51163003), Guangxi Natural Science Foundation of China (2010GXNSFA013030 and 2012GXNSFBA053155) for financial support.

References

[1] Joseph J., Tseng C-Y., Pan C-J., Chen H-M., Lin C-W., Pillai K. C., Hwang B-J.: Growing well-defined monodispersed silica in polyimide host membranes using a surfactant assisted sol-gel process. Polymer, **51**, 5663–5668 (2010).
DOI: 10.1016/j.polymer.2010.09.064

[2] Zou H., Wu S., Shen J.: Polymer/silica nanocomposites: Preparation, characterization, properties, and applications. Chemical Reviews, **108**, 3893–3957 (2008).
DOI: 10.1021/cr068035q

[3] Run M. T., Wu S. Z., Zhang D. Y., Wu G.: A polymer/mesoporous molecular sieve composite: Preparation, structure and properties. Materials Chemistry and Physics, **105**, 341–347 (2007).
DOI: 10.1016/j.matchemphys.2007.04.070

[4] Choi M., Kleitz F., Liu D., Lee H. Y., Ahn W-S., Ryoo R.: Controlled polymerization in mesoporous silica toward the design of organic–inorganic composite nanoporous Materials. Journal of the American Chemical Society, **127**, 1924–1932 (2005).
DOI: 10.1021/ja044907z

[5] Ariga K., Vinu A., Yamauchi Y., Ji Q., Hill J. P.: Nanoarchitectonics for mesoporous materials. Bulletin of the Chemical Society of Japan, **85**, 1–32 (2012).
DOI: 10.1246/bcsj.20110162

[6] Zhang F-A., Lee D-K., Pinnavaia T. J.: PMMA/mesoporous silica nanocomposites: Effect of framework structure and pore size on thermomechanical properties. Polymer Chemistry, **1**, 107–113 (2010).
DOI: 10.1039/B9PY00232d

[7] Zhang F-A., Lee D-K., Pinnavaia T. J.: PMMA–mesocellular foam silica nanocomposites prepared through batch emulsion polymerization and compression molding. Polymer, **50**, 4768–4774 (2009).
DOI: 10.1016/j.polymer.2009.08.007

[8] Shi J-L., Hua Z-L., Zhang L-X.: Nanocomposites from ordered mesoporous materials. Journal of Materials Chemistry, **14**, 795–806 (2004).
DOI: 10.1039/B315861f

[9] Fujiwara M., Shiokawa K., Zhu Y.: Preparation of mesoporous silica/polymer sulfonate composite materials. Journal of Molecular Catalysis A: Chemical, **264**, 153–161 (2007).
DOI: 10.1016/j.molcata.2006.09.016

[10] Suzuki N., Kiba S., Yamauchi Y.: Low dielectric property of novel mesoporous silica/polymer composites using smart molecular caps: Theoretical calculation of air space encapsulated inside mesopores. Microporous and Mesoporous Materials, **138**, 123–131 (2011).
DOI: 10.1016/j.micromeso.2010.09.020

[11] Lu S., Chun W., Yu J., Yang X.: Preparation and characterization of the mesoporous SiO_2–TiO_2/epoxy resin hybrid materials. Journal of Applied Polymer Science, **109**, 2095–2102 (2008).
DOI: 10.1002/app.27856

[12] Lin J. J., Wang X. D.: New type of low-dielectric composite based on *o*-cresol novolac epoxy resin and mesoporous silicas: Fabrication and performances. Journal of Materials Science, **43**, 4455–4465 (2008).
DOI: 10.1007/s10853-008-2655-5

[13] Lin J., Wang X.: Preparation, microstructure, and properties of novel low-κ brominated epoxy/mesoporous silica composites. European Polymer Journal, **44**, 1414–1427 (2008).
DOI: 10.1016/j.eurpolymj.2008.02.022

[14] Lin J., Wang X.: Novel low-κ polyimide/mesoporous silica composite films: Preparation, microstructure, and properties. Polymer, **48**, 318–329 (2007).
DOI: 10.1016/j.polymer.2006.10.037

[15] Yu X., Ding S., Meng Z., Liu J., Qu X., Lu Y., Yang Z.: Aerosol assisted synthesis of silica/phenolic resin composite mesoporous hollow spheres. Colloid and Polymer Science, **286**, 1361–1368 (2008).
DOI: 10.1007/s00396-008-1904-0

[16] Lee T., Park S. S., Jung Y., Han S., Han D., Kim I., Ha C-S.: Preparation and characterization of polyimide/mesoporous silica hybrid nanocomposites based on water-soluble poly(amic acid) ammonium salt. European Polymer Journal, **45**, 19–29 (2009).
DOI: 10.1016/j.eurpolymj.2008.09.022

[17] Hu J., Gu A., Liang G., Zhuo L., Yuan L.: Preparation and properties of mesoporous silica/bismaleimide/diallylbisphenol composites with improved thermal stability, mechanical and dielectric properties. Express Polymer Letters, **5**, 555–568 (2011).
DOI: 10.3144/expresspolymlett.2011.54

[18] Suzuki N., Kiba S., Yamauchi Y.: Fabrication of mesoporous silica KIT-6/polymer composite and its low thermal expansion property. Materials Letters, **65**, 544–547 (2011).
DOI: 10.1016/j.matlet.2010.10.027

[19] Suzuki N., Kiba S., Yamauchi Y.: Bimodal filler system consisting of mesoporous silica particles and silica nanoparticles toward efficient suppression of thermal expansion in silica/epoxy composites. Journal of Materials Chemistry, **21**, 14941–14947 (2011).
DOI: 10.1039/C1JM12405F

[20] Suzuki N., Kiba S., Yamauchi Y.: Fabrication of mesoporous silica/polymer composites through solvent evaporation process and investigation of their excellent low thermal expansion property. Physical Chemistry Chemical Physics, **13**, 4957–4962 (2011).
DOI: 10.1039/C0CP02071K

[21] Suzuki N., Kiba S., Kamachi Y., Miyamoto N., Yamauchi Y.: Mesoporous silica as smart inorganic filler: preparation of robust silicone rubber with low thermal expansion property. Journal of Materials Chemistry, **21**, 5338–5344 (2011).
DOI: 10.1039/C0JM03767B

[22] Romanes M. C., D'Souza N. A., Coutinho D., Balkus K. J., Scharf T. W.: Surface and subsurface characterization of epoxy-mesoporous silica composites to clarify tribological properties. Wear, **265**, 88–96 (2008). DOI: 10.1016/j.wear.2007.08.022

[23] Zhang X., Shen L., Xia X., Wang H., Du Q.: Study on the interface of phenolic resin/expanded graphite composites prepared via *in situ* polymerization. Materials Chemistry and Physics, **111**, 368–374 (2008). DOI: 10.1016/j.matchemphys.2008.04.028

[24] Abdalla M. O., Ludwick A., Mitchell T.: Boron-modified phenolic resins for high performance applications. Polymer, **44**, 7353–7359 (2003). DOI: 10.1016/j.polymer.2003.09.019

[25] Liu L., Ye Z.: Effects of modified multi-walled carbon nanotubes on the curing behavior and thermal stability of boron phenolic resin. Polymer Degradation and Stability, **94**, 1972–1978 (2009). DOI: 10.1016/j.polymdegradstab.2009.07.022

[26] Ye C., Gong Q-M., Lu F-P., Liang J.: Preparation of carbon nanotubes/phenolic-resin-derived activated carbon spheres for the removal of middle molecular weight toxins. Separation and Purification Technology, **61**, 9–14 (2008). DOI: 10.1016/j.seppur.2007.09.021

[27] Kaynak C., Tasan C. C.: Effects of production parameters on the structure of resol type phenolic resin/layered silicate nanocomposites. European Polymer Journal, **42**, 1908–1921 (2006). DOI: 10.1016/j.eurpolymj.2006.03.008

[28] Tasan C. C., Kaynak C.: Mechanical performance of resol type phenolic resin/layered silicate nanocomposites. Polymer Composites, **30**, 343–350 (2009). DOI: 10.1002/pc.20591

[29] Zhao D., Feng J., Huo Q., Melosh N., Fredrickson G. H., Chmelka B. F., Stucky G. D.: Triblock copolymer syntheses of mesoporous silica with periodic 50 to 300 angstrom pores. Science, **279**, 548–552 (1998). DOI: 10.1126/science.279.5350.548

[30] Zhao D., Huo Q., Feng J., Chmelka B. F., Stucky G. D.: Nonionic triblock and star diblock copolymer and oligomeric surfactant syntheses of highly ordered, hydrothermally stable, mesoporous silica structures. Journal of the American Chemical Society, **120**, 6024–6036 (1998). DOI: 10.1021/ja974025i

[31] Grenier-Loustalot M-F., Larroque S., Grenier P., Leca J-P., Bedel D.: Phenolic resins: 1. Mechanisms and kinetics of phenol and of the first polycondensates towards formaldehyde in solution. Polymer, **35**, 3046–3054 (1994). DOI: 10.1016/0032-3861(94)90418-9

[32] Ji X., Hampsey E., Hu Q., He J., Yang Z., Lu Y.: Mesoporous silica-reinforced polymer nanocomposites. Chemistry of Materials, **15**, 3656–3662 (2003). DOI: 10.1021/cm0300866

[33] Hernández-Padrón G., Rojas F., García-Garduño M., Canseco M. A., Castaño V. M.: Development of hybrid materials consisting of SiO_2 microparticles embedded in phenolic-formaldehydic resin polymer matrices. Materials Science and Engineering A, **355**, 338–347 (2003). DOI: 10.1016/S0921-5093(03)00101-1

[34] Hoffmann F., Cornelius M., Morell J., Fröba M.: Silica-based mesoporous organic–inorganic hybrid materials. Angewandte Chemie International Edition, **45**, 3216–3251 (2006). DOI: 10.1002/anie.200503075

[35] Yu J., Huang X., Wang L., Peng P., Wu C., Wu X., Jiang P.: Preparation of hyperbranched aromatic polyamide grafted nanoparticles for thermal properties reinforcement of epoxy composites. Polymer Chemistry, **2**, 1380–1388 (2011). DOI: 10.1039/C1PY00096a

eXPRESS Polymer Letters Vol.6, No.10 (2012) 794–804
Available online at www.expresspolymlett.com
DOI: 10.3144/expresspolymlett.2012.85

Effect of nanocellulose isolation techniques on the formation of reinforced poly(vinyl alcohol) nanocomposite films

Y. M. Zhou[1], *S. Y. Fu*[1*], *L. M. Zheng*[2], *H. Y. Zhan*[1]

[1]State Key Laboratory of Pulp and Paper Engineering, College of Light Industry and Food Science, South China University of Technology, Guangzhou, 510640 Guangdong, China
[2]School of Chemistry and Chemical Engineering, South China University of Technology, Guangzhou, 510640 Guangdong, China

Received 19 February 2012; accepted in revised form 1 May 2012

Abstract. Three techniques including acid hydrolysis (AH), 2,2,6,6-tetramethylpiperidine-1-oxyl radical (TEMPO)-mediated oxidation (TMO) and ultrasonication (US) were introduced to isolate nanocellulose from microcrystalline cellulose, in order to reinforce poly(vinyl alcohol) (PVA) films. Important differences were noticed in fiber quality of nanocellulose and film properties of PVA nanocomposite films. The TMO treatment was more efficient in nanocellulose isolation with higher aspect ratio, surface charge (–47 mV) and yields (37%). While AH treatment resulted in higher crystallinity index (88.1%) and better size dispersion. The fracture surface, thermal behavior and mechanical properties of the PVA nanocomposite films were investigated by means of scanning electron microscopy (SEM), differential scanning calorimetry (DSC), thermogravimetric analysis (TGA) and tensile testing. The results showed that both the TMO-derived and AH-derived nanocellulose could be dispersed homogeneously in the PVA matrices. AH/PVA films had higher elongation at break (51.59% at 6 wt% nanocellulose loading) as compared with TMO/PVA, while TMO/PVA films shown superior tensile modulus and strength with increments of 21.5% and 10.2% at 6wt% nanocellulose loading. The thermal behavior of the PVA nanocomposite films was higher improved with TMO-derived nanofibrils addition.

Keywords: *nanocomposites, isolation techniques, cellulose, reinforcements*

1. Introduction

Owing to environmentally friendly attributes, good mechanical properties, low density, biodegradability and abundant availability of renewable resources, the production of nanocellulose and their application in composites materials has gained increasing attention in recent times [1–2]. Nanocelluloses are recognized to be more effective in reinforcing polymers, due to the interaction between the nano-sized elements that form a percolated network connected by hydrogen bonding [3]. Two different types of nanocellulose can be isolated from a cellulosic source: nanocrystals and nanofibrils. Nanocrystals have a perfect crystalline structure and high modulus, close to the theoretical modulus of cellulose; nanofibrils are fibrillar units containing both amorphous and crystalline regions and have the ability to create entangled networks [4]. Different properties of these two types of nanocellulose will result in varying reinforcement of nanocomposites.

In order to utilize nanocellulose as a reinforcing phase to form nanocomposites, the strong hydrogen bonding between cellulose crystals must be separated and dispersed well in the polymer matrices [5]. Extensive research has been reported to extract nanocellulose from different sources [6–10]. Typical processes involve mechanical and chemical treatments. The chemical ways, mainly by strong

*Corresponding author, e-mail: shyfu@scut.edu.cn

acid hydrolysis, can remove the amorphous regions of cellulose fibers and produce cellulose nanocrystals [11–12]. While for mechanical methods, which include high intensity ultrasonication [13], high pressure refiner [14] or grinder treatment [15], the main product generated is not a single fiber and has been referred as nanofibrils. However, these two techniques of extracting nanocellulose from plants are time consuming and very costly [1]. It involves high consumption of energy for processes as mechanical treatments [16], which can cause dramatic decrease in both the yield and fibril length down to 100–150 nm and also introduces damage to the environment, as in the case of chemical treatments [17]. Current research has been focused on finding environmental conservation, high efficiency and low costs methods to isolate nanocellulose. Recently, individualized cellulose nanofibrils have been obtained using 2,2,6,6-tetramethylpiperidine-1-oxyl radical (TEMPO)-mediated oxidation for regioselective conversion of the cellulose primary hydroxyl groups to aldehydes and carboxylate ones. The mild reaction condition (room temperature and alkalescent medium), the characteristic of little fiber morphological change and the resultant diverse surface functionalities (carboxyl, aldehyde, and hydroxyl) lend the TEMPO-mediated oxidation technique significant potential in the fields of composites reinforcement [18–19].

Currently, very few references are available about the systematic study of the effect of nanocellulose isolation techniques on the quality of nanocellulose and its performance in reinforced nanocomposites. The main goal of this work is to employ three different techniques including acid hydrolysis (AH), TEMPO-mediated Oxidation (TMO) and ultrasonication (US) to isolate nanocellulose from microcrystalline cellulose (MCC) and to evaluate the quality of nanocellulose and the reinforcing ability of these nanocellulose in PVA matrices.

2. Experiment

2.1. Materials

Microcrystalline cellulose (MCC) with a mean diameter size of 20 μm, purchased from Xuanyuan Machinery (Shandong, China) was used as raw material. Poly(vinyl alcohol) (PVA, 99% hydrolyzed, M_w 85 000~124 000) was used as matrices. Sulfuric acid (98 wt%) was used for the acid hydrolysis of MCC. 2,2,6,6-tetramethylpiperidine-1-oxyl radical (TEMPO), sodium bromide (NaBr) and 6% sodium hypochlorite (NaClO) solution were used for the TEMPO-mediated oxidation of MCC. All chemicals were of laboratory grade (Sigma-Aldrich, China) and used without further purification.

2.2. Nanocellulose isolation

2.2.1. Acid hydrolysis (AH)

About 5 g MCC was mixed with 45 mL sulfuric acid (64 wt%), the mixture was hydrolyzed at 45ºC for 120 min with continuous stirring (500 rpm). The hydrolysis was quenched by adding 500 mL water to the reaction mixture and then the slurry was washed with distilled water for 20 min at 5000 rpm, using repeated centrifugation. The supernatant was removed from the sediment and replaced by new distilled water and mixed, the centrifugation step continued until the pH of the supernatant became 1. The last wash was conducted using dialysis with distilled water until the wash water maintained a constant pH of 7. The resultant suspension was stored at 4°C before further analysis or treatments.

2.2.2. TEMPO-mediated oxidation (TMO)

About 5 g MCC was suspended in 500 mL distilled water containing TEMPO (0.080 g, 0.5 mmol) and NaBr (0.5 g, 5 mmol). The TEMPO-mediated oxidation was started by adding 6% NaClO solution (25.0 mmol) with continuous stirring (500 rpm) at room temperature. The pH was maintained at 10 by adding 0.5 M NaOH using a pH stat until no NaOH consumption was observed. The TEMPO-oxidized cellulose thus obtained was then ultrasonicated for 20 min, using an ultrasonic homogenizer (KBS-1200, China) with an output power of 1200 W. The slurry was washed with distilled water by repeated centrifugation (5000 rpm, 20 min) and then centrifuged at 12 000 rpm to separate large particles. After that, the samples were dialyzed against distilled water until the pH reached 7. The resultant suspension was stored at 4°C before further analysis or treatments.

2.2.3. Ultrasonication (US)

About 5 g MCC was dispersed in 500 mL distilled water under continuous stirring for a whole day, then ultrasonicated for 60 min using an ultrasonic homogenizer (KBS-1200, China) with an output

power of 1200 W, equipped with a sonication probe of 20 mm. In order to avoid overheating, the beaker with the cellulose suspension was put in an ice bath with controlled temperature. Two hours after the ultrasonication process ended, nanocellulose was obtained from the water suspension by decanting the supernatant into other vessels. The resultant suspension with pH of 7 was stored at 4°C before further analysis or treatments.

2.3. Nanocomposite films preparation

PVA water solution (10 wt%) and nanocellulose suspension (2 wt%, relative to the PVA mass) were mixed under continuous stirring (500 rpm) at 80ºC for 3 hours, then dispersed by ultrasonic treatment (KBS-1200, China) for about 2 min with 50% power level. Films were cast onto a PTFE plate with controlled leveling, the mixture in the plate were degassed in a vacuum desiccator, and then evaporated at 25°C and relative humidity of 30% until films were formed, the films were heat treated in an oven at 80ºC for more than 12 h. Films with three levels of nanocellulose loading (2, 6 and 10 wt%) were manufactured. The thicknesses of the films were controlled to be approximately 150 μm.

2.4. Characterization

2.4.1. Morphology and crystallinity analysis

Morphology of the nanocellulose and fractured surface of the PVA nanocomposite films were examined using scanning electron microscopy (Nova, NanoSEM 430, FEI Company) with an accelerating voltage of 15 kV. For nanocellulose observation, a droplet of the nanocellulose suspensions (0.1 wt%) was put on a glass grid and dried under vacuum before SEM analysis. The dried nanocellulose and the fractured surface of the films (after tensile tests) were coated with gold on an ion sputter coater, various magnification levels were used to obtain images. More than three images were taken and chosen to observe the morphology of all samples.

Wide-angle X-ray diffraction (WXRD) data was collected using a X-ray diffractometer (Rigaku D/max-III A, Japan) equipped with Cu K_α radiation (λ = 0.1541 nm) at the operating voltage and current of 45 kV and 100 mA, respectively. Diffractograms were collected in a 2θ range of 4~50° at a rate of 1°/min with a resolution of 0.05°.

2.4.2. Wet particle size and surface charge analysis

Nanocellulose particle size analysis was conducted by dynamic light scattering (DLS) using a Zetasizer NanoZS instrument (Malvern, UK), under the following conditions: dispersant water, material refractive index 1.47, dispersion refractive index 1.33, viscosity 0.8872 cP, temperature 25°C and general calculation model for irregular particles. Three measurements of 10 s each were taken and the averaging was done.

The zeta-potential (estimated as surface charge) tests of the nanocellulose particles were conducted with the Zetasizer NanoZS Instrument (Malvern, UK). Experiments were performed in a cuvette consisting of 4 ml 0.1 wt% nanocellulose suspension, solutions were all adjusted at pH values of 7.

2.4.3. Thermal properties

The differential scanning calorimetry (DSC) of PVA nanocomposite films was performed on a DSC Q200 (TA Instruments, USA) from 25 to 300°C at a heating rate of 10°C/min under nitrogen flow. Approximately 8 mg samples were used. The thermogravimetric analysis (TGA) were performed using a TGA Q500 (TA Instruments, USA). About 5~10 mg samples were heated from 30 to 600°C with a heating rate of 10°C/min under a nitrogen atmosphere. The weight change was recorded as a function of the heating temperature.

2.4.4. Mechanical properties

The mechanical tests were performed using a testing machine (Instron 5567, USA) with a crosshead speed of 5 mm/min. The crosshead extensions were used as specimen deformations. The films were cut to dog bone shapes with width of 15 mm for the narrow portion and total length of 50 mm (gauge length was 25 mm). The thickness of the films was calculated before the test. The values of tensile modulus, tensile strength and elongation at break of the samples were evaluated and reported as the average values of five measurements of each composition. Prior to testing, films were kept in a humidity chamber desiccator with a 50% relative humidity (RH) and 25°C for 5 days (according to the ASTM D1708 standard [20]).

3. Results and discussion

3.1. Morphological properties

The SEM morphology of untreated MCC and nanocellulose (isolated from acid hydrolysis (AH), TEMPO-mediated oxidation (TMO) or ultrasonication (US) are shown in Figure 1. Nanocelluloses isolated from AH technique have individual crystallites and disperse uniformly showing needle shaped structures (namely nanocrystals), with diameters of 30~40 nm and lengths of 200~400 nm. While the TMO-derived nanocellulose are interconnected webs with tiny nanofibers (namely nanofibrils), with diameters of 40~80 nm and the lengths are ranging from 200 nm to several micrometers, which have a wide range of aspect ratio, most are more than 50 as evident from the measurements of randomly selected features, nanofibrils of this aspect ratio are suitable for polymer reinforcement, in order to allow sufficient stress transfer, and thereby act as an effective reinforcing agent [21]. However, in the case of samples prepared with the US treatment, pieces of undefibrilated MCC and many microfibril bundles are observed.

3.2. XRD analysis

Figure 2 shows the X-ray diffraction of the MCC and nanocellulose (isolated from AH, TMO or US). In all curves, peaks are observed at 2θ =14.8, 16.6 and 22.9°, corresponding to a cellulose I structure,

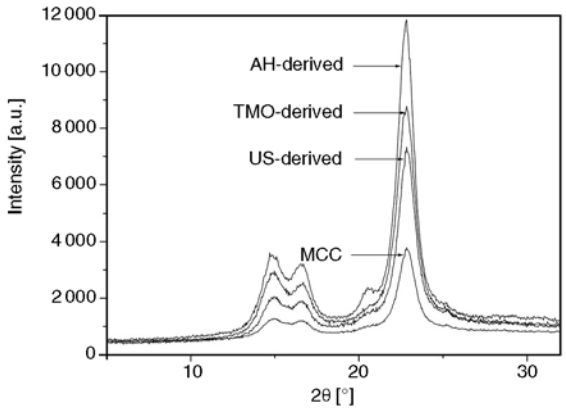

Figure 2. X-ray diffraction patterns of MCC and nanocellulose (isolated from different treatments)

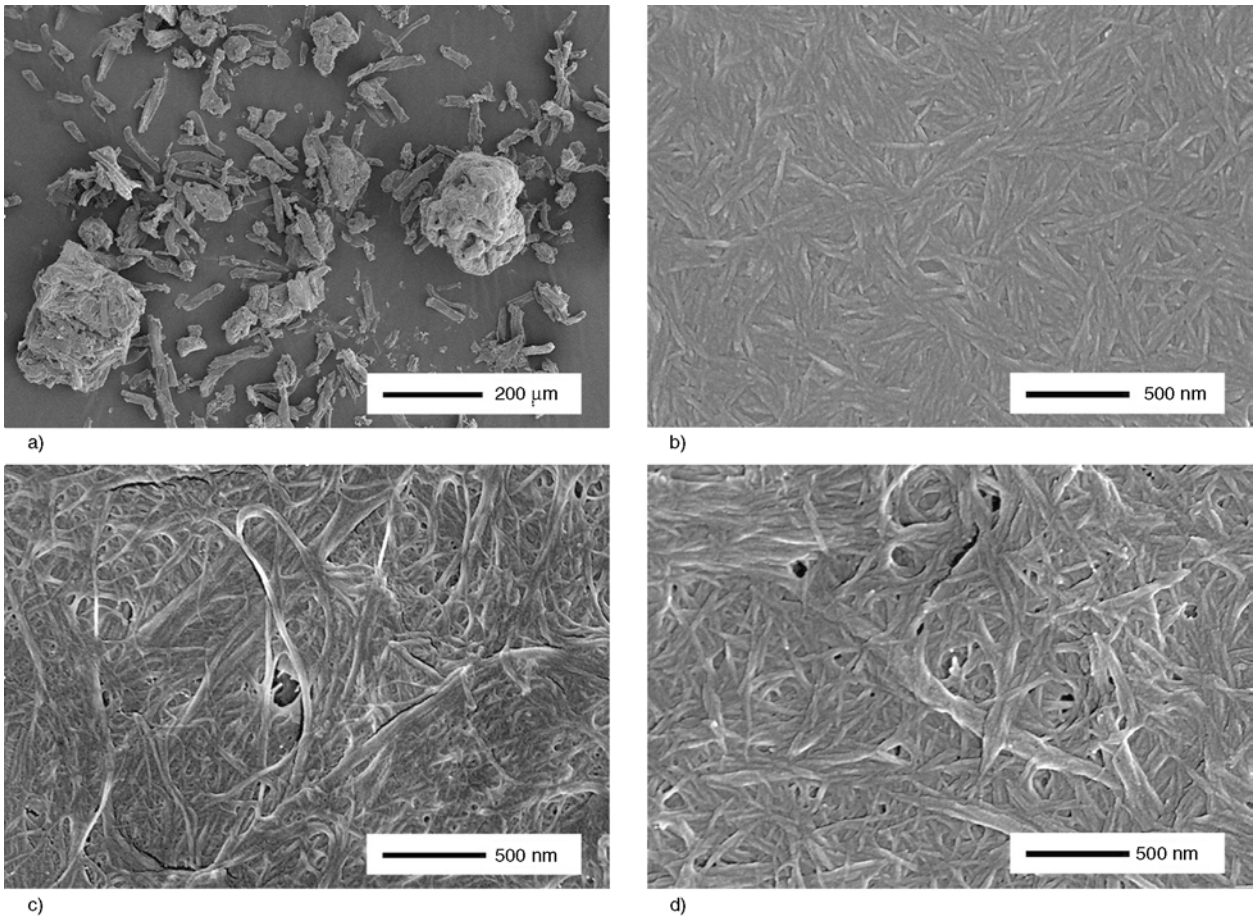

Figure 1. SEM images of (a) untreated MCC, (b) AH-derived nanocellulose, (c) TMO-derived nanocellulose and (d) US-derived nanocellulose. (mag 100× for (a), (mag 100000× for (b), (c), (d))

Table 1. Parameters of MCC and nanocellulose (isolated from different treatments)

Nanocellulose	MCC	AH-derived	TMO-derived	US-derived
X_c [%]	79.5±2.0	88.1±1.8	86.4±2.0	86.5±2.1
Yield [%]	–	28.6±8.0	37.4±8.3	12.7±3.2
Zeta [mV]	–8.3±3.4	–38.2±3.4	–46.5±3.4	–23.1±3.4
Particle size [nm]	~μm	115±35	210±54	623±93

Results expressed as mean±standard deviation

which means that all the three techniques have no effect on the crystal form of the native cellulose. The intensity of the peaks is higher for all the nanocellulose samples, showing that nanocellulose samples are more crystalline than MCC. The crystallinity index (X_c) of the cellulose can be calculated using the Equation (1) [22]:

$$X_c = \frac{I_{crystalline} - I_{amorphous}}{I_{crystalline}} \cdot 100 \quad (1)$$

where $I_{crystalline}$ is the intensity of the peak at 2θ about 22.9°representing crystalline material and $I_{amorphous}$ is the intensity of the peak at 2θ about 18° representing amorphous material in cellulosic fibers. The values of the crystallinity index obtained are shown in Table 1. The cellulose X_c is of the order AH-derived > TMO-derived > US-derived > MCC. The maximum X_c (88.1%) was obtained when AH process was carried out for the treatment of MCC, due to the removal of the majority of amorphous regions during the harsh process and resulted in needle shaped individual crystallites. On the other hand, there is an increase of diffraction intensities in the crystalline peak around $2\theta = 20.5°$ of AH-derived nanocellulose, which may be attributed to the higher-ordered region of cellulose chains. For TMO and US treatments, the nanocellulose X_c values are also high (86.4 and 86.5%, respectively), it has been reported that TMO process produces no change in crystallinity of cellulose even at a high oxidation level of 10 mmol NaClO/g cellulose [23]. The X_c increase of the TMO-derived nanocellulose in this study may be attributed to the partial removal of amorphous regions, due to the harsh ultrasonication treatment of oxidized samples.

3.3. Yields analysis

The yield results of the nanocellulose (isolated from AH, TMO or US) are shown in Table 1. In cellulosic plant fibers, cellulose is present in an amorphous state, but also associates to crystalline domains through both inter-molecular and intra-molecular hydrogen bonding [24]. AH is a well-known harsh process conducted to the disintegration of amorphous regions and degradation of crystalline parts generating a low yield of 28.6%. This kind of procedure affects the total integrity of fibers. While for US method, the mechanical treatment alone cannot be effective to separate the strong hydrogen bonding of native fibers. This is why the yield of US-derived nanocellulose is as low as 12.7% and pieces of undefibrilated MCC still remained. While TMO is a method of combination of chemical and mechanical treatments, the mild reaction condition of room temperature, alkalescent medium and characteristic of regioselective oxidation [18–19] maintain partially amorphous regions left in the axial direction of the starting material, which result in a higher yield of 37.4%, as well as higher aspect ratio of the final TMO-derived nanofibrils.

3.4. Surface charge analysis

Zeta potential (estimated as surface charge) can be measured by tracking the moving rate of negatively or positively charged particles across an electric field. Usually a value less than –15m V represents the onset of agglomeration. Values greater than –30 mV generally signifies that there is sufficient mutual repulsion which results in colloidal stability [25]. The zeta potential data of the nanocellulose suspension (isolated from AH, TMO or US) are shown in Table 1, attributed to the esterification of cellulose hydroxyl groups to sulfonate groups during the AH process and the regioselective conversion of the cellulose primary hydroxyl groups to carboxyl ones during the TMO process, the AH and TMO-derived nanocellulose possess high negative charge of –38.2 and –46.5 mV, respectively. For TMO-derived nanofibrils, the highest surface charge imparts electrostatic repulsive forces to the system, preventing the binding between nanofibrils-nanofibrils, and thus homogeneous nanocellulose suspension is obtained. The uniform dispersion of nanocellulose is critical to improve the mechanical properties of the final nano-

composite products, promoting the actual formation of hydrogen bonding between the PVA and nanocellulose (nanocrystals or nanofibrils), which also leads to a higher efficiency of the stress transfer from the matrices to the fibers. In contrast, the US generated nanocellulose has only a weak charge of –23.1 mV originated from its inherent hydroxyl groups, the formation of larger insoluble precipitates was revealed by SEM image (Figure 1).

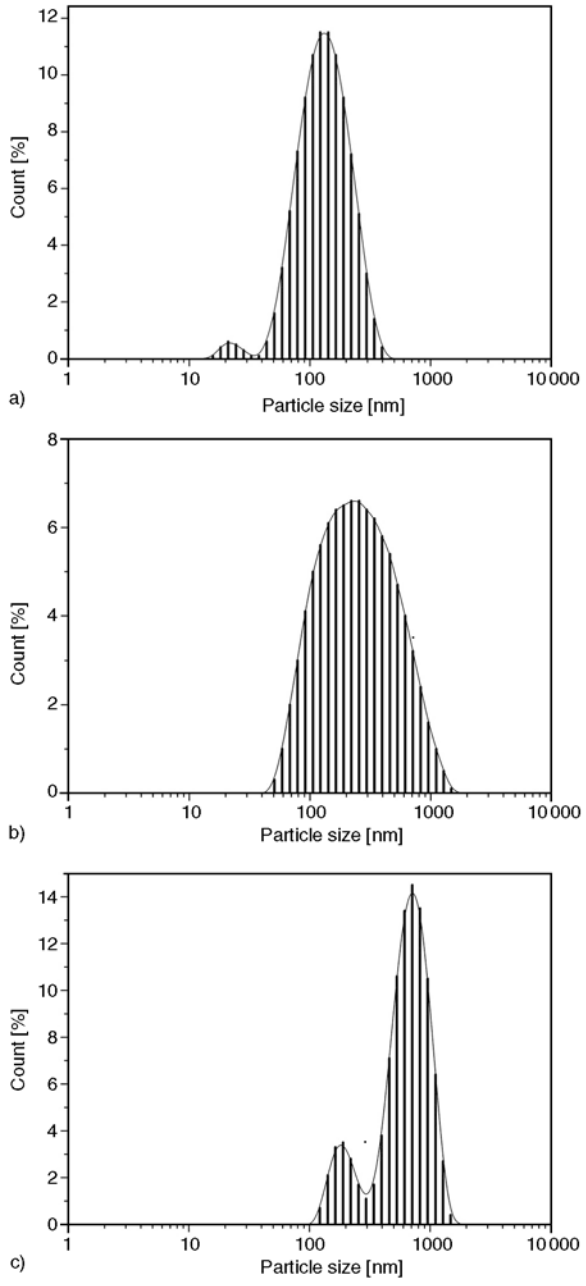

Figure 3. Size dispersion of (a) AH-derived nanocellulose, (b) TMO-derived nanocellulose, (c) US-derived nanocellulose

3.5. Size dispersion analysis

Dynamic light scattering (DLS) analysis has been employed to find the statistical distribution of the particles present in nanocellulose. After measuring millions of particles, an average particle size of the nanocellulose (isolated from AH, TMO or US) were found to be 115, 210 and 623 nm (Table 1), respectively. Larger particle size than those determined for samples in SEM analysis were obtained in DLS measurements, because of the rapid aggregation of nanocellulose in water suspension. The size dispersion of the different nanocellulose particles are shown in Figure 3. Because of the concentrated acid (64 wt% H_2SO_4) hydrolysis used to harshly destroy the majority of cellulose hydrogen bonding, the AH reaction is homogeneous and more complete, that resulted in a narrower nanocellulose size distribution, besides, the strong surface charge (–38.2 mV) also prevents the nanocellulose particles from agglomerating. The TMO-derived nanocellulose particles display a relatively poor size dispersion, mainly due to the mild reaction condition compared to the AH treatment. For US treatment, the lack of surface charge (–23.1 mV) induced continuing agglomerate of insoluble nanocellulose particles, resulted in a wide size dispersion.

3.6. Thermal properties

Thermal characterization of neat PVA and PVA nanocomposite films was carried out using DSC and TGA measurements. From the analysis of DSC traces (Figure 4), the glass rubber transition temperature (T_g), the melting temperature (T_m), heat of

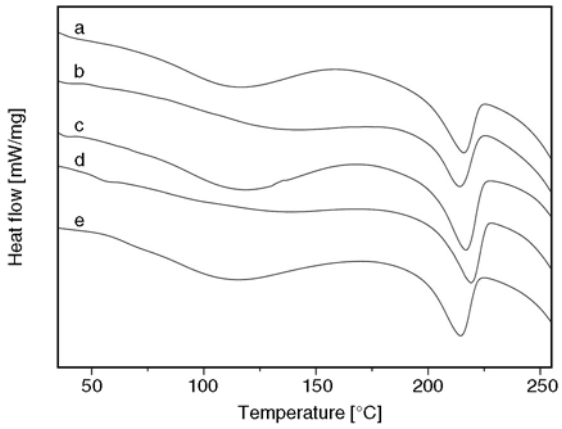

Figure 4. DSC curves of (a) neat PVA, (b) MCC/PVA, (c) AH/PVA, (d) TMO/PVA and (e) US/PVA films (6 wt% filler loading)

Table 2. TGA data of neat PVA and PVA nanocomposite films (6 wt% filler loading)

Samples	Neat PVA	MCC/PVA	AH/PVA	TMO/PVA	US/PVA
T_g [°C]	70.3	68.0	75.1	76.9	71.2
T_m [°C]	215.9	214.1	218.8	219.1	214.5
ΔH_m [J/g]	81.1	76.8	88.5	84.9	80.6
X_c [%]	54.1	54.5	62.8	60.2	57.1
T_{10} [°C]	239.3	239.2	252.8	254.9	245.8
T_{50} [°C]	283.4	304.5	306.8	314.9	300.4
T_d [°C]	270.4	271.1	277.2	287.8	264.0

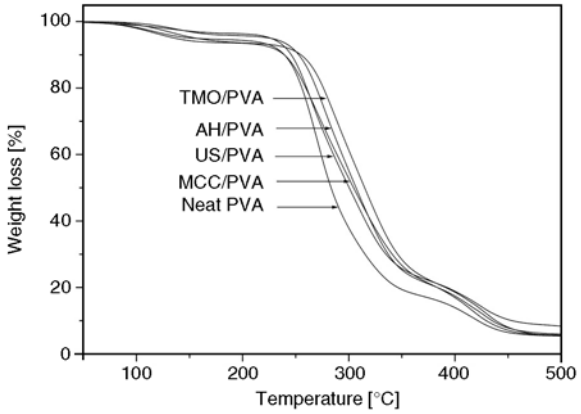

Figure 5. TGA curves of neat PVA and PVA nanocomposite films (6 wt% filler loading)

fusion (ΔH_m) and degree of crystallinity (X_c) were evaluated and compared. The resulting experimental data are listed in Table 2. The glass transition temperature (T_g) of PVA nanocomposites is increased with the addition of AH-derived and TMO-derived nanocellulose. The strong hydrogen bonding formation between the PVA matrices and nanocellulose is expected to restrict the segmental mobility of polymer chains and thereby increase T_g. The features of Tm, ΔH_m, and X_c are also enhanced as compared to neat PVA films. The increase in X_c is possibly due to the nucleating effect of the nano-sized fibers. This enhancement of the Xc of the PVA matrices probably results, at least partially, in the improvement of the mechanical properties for TMO/PVA films as reported later. On the contrary, the thermal behavior is not obviously enhanced for US/PVA films and even tends to decrease upon MCC addition. It means that the presence of large agglomerate and microfibril bundles induce steric hindrance effects restricting the growth of crystalline PVA regions. It results in both a lower melting point and lower degree of crystallinity.

The thermal stability of the neat PVA and PVA nanocomposite films examined by TGA are shown in Figure 5. All samples show major weight loss in the range of 30~550°C. For PVA nanocomposite films, a slight increase of the major degradation temperatures ($T_{10°C}$, $T_{50°C}$ and T_d) (Table 2) is observed, in the sequence of TMO/PVA > AH/PVA > US/PVA > MCC/PVA > neat PVA, thus further confirming the enhanced thermal stability due to a strong hydrogen bonding between the TMO-derived nanocellulose and the PVA matrices. The reason maybe that despite the regioselective oxidation of the cellulose primary hydroxyl groups to carboxylate ones in TMO treatments, the total amount of the strong hydrogen bonding in film formation is not affected. In contrast, the hydrogen bonding between the AH-derived nanocellulose and PVA matrices is decreased, due to the esterification of hydroxyl groups to sulfonate groups during the AH process. The US/PVA nanocomposite films have relatively lower degradation temperature. Because the specific surface area of US-derived nanocellulose is not as high as the AH-derived or TMO-derived ones, resulting in fewer hydroxyl groups on the nanocellulose surface, besides, the easy formation of larger insoluble precipitates will also accelerate this process, these two factors resulted in lower thermal stability of the final composites.

3.7. SEM and mechanical properties

The fractured surface after tensile tests of neat PVA and PVA nanocomposite films were examined using SEM as shown in Figure 6. As compared to the neat PVA films, the morphology of the AH/PVA and TMO/PVA films can be easily identified. The nanocellulose appears as white dots, these white dots could correspond to the nanocrystals (AH-derived) or nanofibrils (TMO-derived). No large aggregates and a homogeneous distribution of the nanocellulose in the PVA matrix are observed in both AH/PVA and TMO/PVA films, implying good adhesion between fillers and matrix. This should be attributed to the formation of a rigid hydrogen-bonded

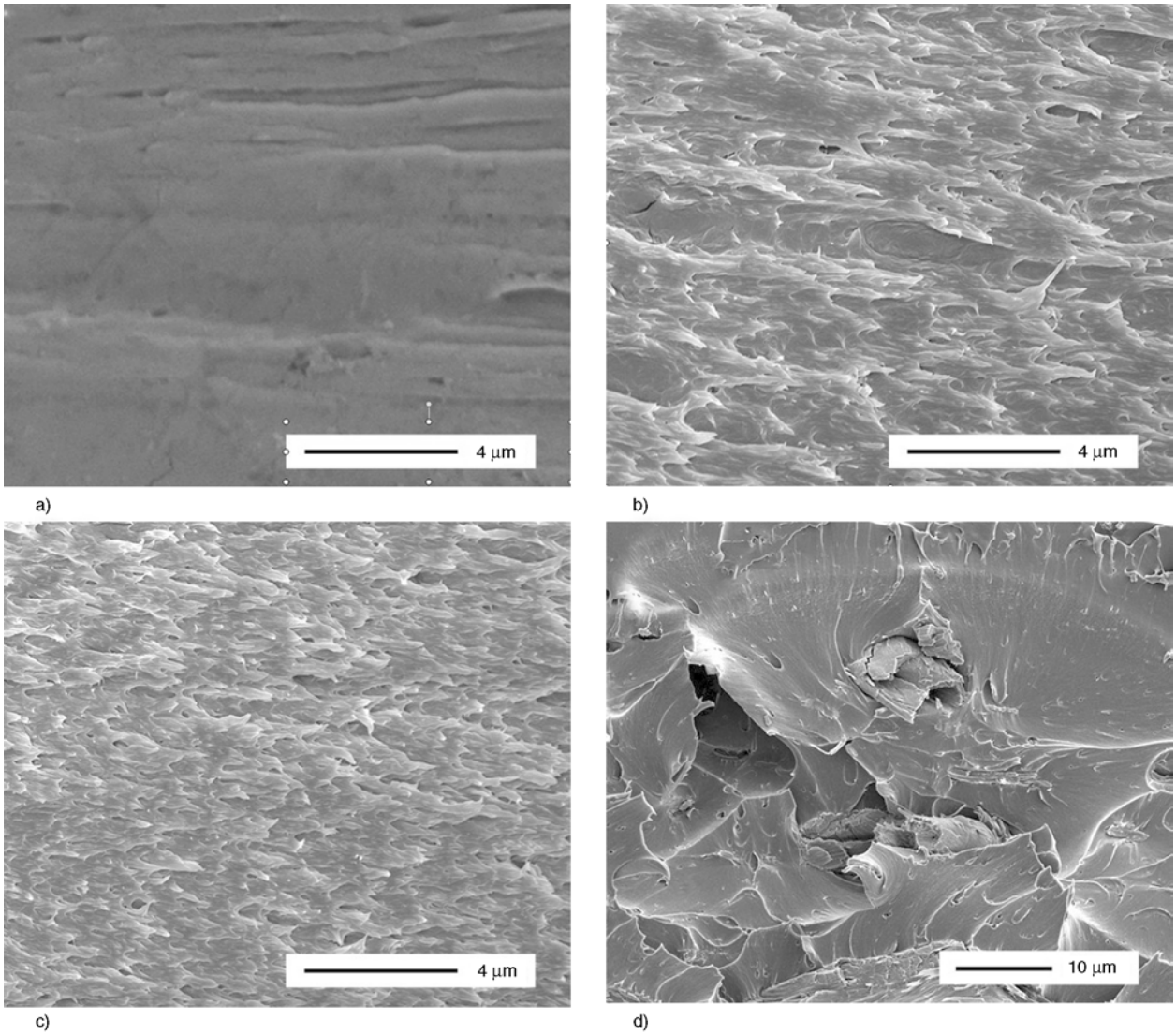

Figure 6. SEM images of fractured surface of (a) neat PVA, (b) AH/PVA, (c) TMO/PVA and (d) US/PVA films.(mag 20000× for (a), (b), (c), (mag 10000× for (d))

network of nanocellulose that is governed by percolation theory. Such an even and uniform distribution of the fillers in the matrix could play an important role in improving the mechanical performance of the resulting nanocomposite films as discussed later. However, some microfibril bundles are observed in fractured surface of US/PVA films, because of lack of bulk charge on the US-derived nanofibrils, which makes the nanofibrils to contact and interact extensively with each other leading to the formation of loose and bulky aggregates in PVA matrices.

The tensile modulus, tensile strength and elongation at break of neat PVA and PVA nanocomposite films (2, 6, and 10 wt% loading) are shown in Figures 7, 8 and 9, respectively. It is found that the modulus and strength are both higher for TMO/PVA nanocomposite films, with increments of 21.5 and 10.2% at the 6 wt% nanofibrils loading, respectively. The higher aspect ratio and the stronger hydrogen bonding of TMO-derived nanofibrils in the PVA matrix are the main reasons to explain this phenomenon. Whereas the elongation at break of TMO/PVA films is lower for a given loading level as compared with AH/PVA nanocomposite films. The difference is most probably ascribed to the possibility of entanglements of nanofibrils contrarily to rod-like nanocrystals. The US/PVA films are better than MCC/PVA films for modulus and elongation but similar to strength, the increase in tensile modulus or elongation of US/PVA films is less than the one reinforced by AH or TMO-derived nanocellulose. The reason is that in the US-derived nanocellulose is easy to produce larger insoluble agglomerates and always have some bigger fibrils (> 1 μm),

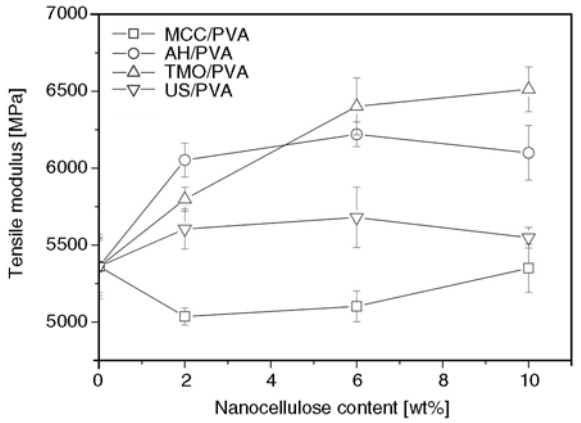

Figure 7. Tensile modulus of neat PVA and PVA nanocomposite films (2, 6 and 10 wt% filler loading)

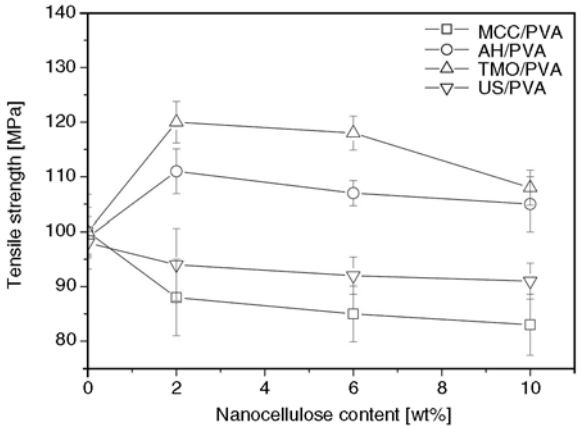

Figure 8. Tensile strength of neat PVA and PVA nanocomposite films (2, 6, and 10 wt% filler loading)

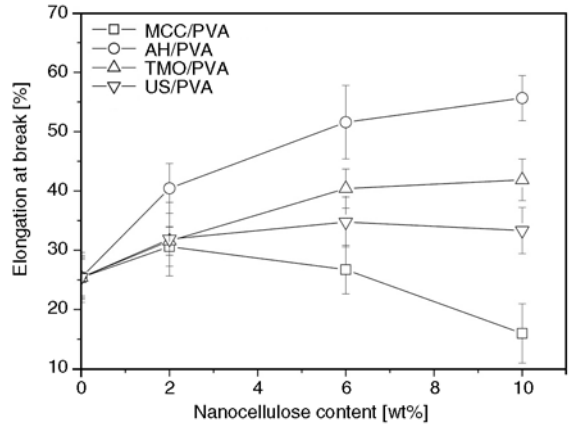

Figure 9. Elongation at break of neat PVA and PVA nanocomposite films (2, 6 and 10 wt% filler loading)

and because of the resulting lower aspect ratio the matrix strain exceeds that of the fibers throughout the whole length of the fibers. In such cases, the fibers do not provide efficient reinforcement, because they carry much less load than longer fibers in the same system, and hence, the composites fails before the full reinforcing potential of the fiber is attained. Besides, the fibrils may not be even and fine enough, which have more defects and low mechanical property than those of smaller nanofibrils and nanocrystal [26]. Adding more nanocellulose (10 wt%) did not increase furher tensile modulus, strength or elongation, the nanocellulose agglomeration at higher concentration is the most important factor.

4. Conclusions

Three different techniques (acid hydrolysis (AH), TEMPO-mediated oxidation (TMO) and ultrasonication (US)) were employed to isolate nanocellulose from microcrystalline cellulose. The resulting nanocellulose was used to reinforce Poly(vinyl alcohol) (PVA) films. The characterization of nanocellulose indicated that nanocellulose with higher aspect ratio, surface charge (–47 mV) and yields (37%) was obtained by TMO treatment. While AH treatment resulted in higher crystallinity index (88.1%) and better size dispersion. Both the TMO-derived and AH-derived nanocellulose could homogeneous disperse in the PVA matrixes. The TMO/PVA films were better than AH/PVA films for tensile modulus and strength but lower for elongation. The thermal behavior of the PVA nanocomposite films was higher improved with TMO-derived nanofibrils addition. Comparing to AH and US techniques, because of the mild reaction condition, the environmental friendly attribute, the good quality of resulted nanofibrils and the superior properties of the final reinforced nanocomposites the TMO technique has significant potential in the field of composites reinforcement.

Acknowledgements

This work was supported by Major State Basic Research Development Program of China (No.2010CB732206) and Doctoral Program Foundation of Institutions of Higher Education of China (20090172110022).

References

[1] Spagnol C., Rodrigues F. H. A., Pereira A. G. B., Fajardo A. R., Rubira A. F., Muniz E. C.: Superabsorbent hydrogel composite made of cellulose nanofibrils and chitosan-*graft*-poly(acrylic acid). Carbohydrate Polymers, **87**, 2038–2045 (2012).
DOI: 10.1016/j.carbpol.2011.10.017

[2] Cheng Q., Wang S., Rials T.: Poly(vinyl alcohol) nanocomposites reinforced with cellulose fibrils isolated by high intensity ultrasonication. Composites Part A: Applied Science and Manufacturing, **40**, 218–224 (2009).
DOI: 10.1016/j.compositesa.2008.11.009

[3] Dubief D., Samain E., Dufresne A.: Polysaccharide microcrystals reinforced amorphous poly(β-hydroxyoctanoate) nanocomposite materials. Macromolecules, **32**, 5765–5771 (1999).
DOI: 10.1021/ma990274a

[4] Eichhorn S. J., Dufresne A., Aranguren M., Marcovich N. E., Capadona J. R., Rowan S. J., Weder C., Thielemans W., Roman M., Renneckar S., Gindl W., Veigel S., Keckes J., Yano H., Abe K., Nogi M., Nakagaito A. N., Mangalam A., Simonsen J., Benight A. S., Bismarck A., Berglund L. A., Peijs T.: Review: Current international research into cellulose nanofibres and nanocomposites. Journal of Materials Science, **45**, 1–33 (2010).
DOI: 10.1007/s10853-009-3874-0

[5] Lee S-Y., Mohan D. J., Kang I-A., Doh G-H., Lee S., Han S. O.: Nanocellulose reinforced PVA composite films: Effects of acid treatment and filler loading. Fibers and Polymers, **10**, 77–82 (2009).
DOI: 10.1007/s12221-009-0077-x

[6] Abraham E., Deepa B., Pothan L. A., Jacob M., Thomas S., Cvelbar U., Anandjiwala R.: Extraction of nanocellulose fibrils from lignocellulosic fibres: A novel approach. Carbohydrate Polymers, **86**, 1468–1475 (2011).
DOI: 10.1016/j.carbpol.2011.06.034

[7] Mandal A., Chakrabarty D.: Isolation of nanocellulose from waste sugarcane bagasse (SCB) and its characterization. Carbohydrate Polymers, **86**, 1291–1299 (2011).
DOI: 10.1016/j.carbpol.2011.06.030

[8] Morán J. I., Alvarez V. A., Cyras V. P., Vázquez A.: Extraction of cellulose and preparation of nanocellulose from sisal fibers. Cellulose, **15**, 149–159 (2008).
DOI: 10.1007/s10570-007-9145-9

[9] Siqueira G., Tapin-Lingua S., Bras J., da Silva Perez D., Dufresne A.: Morphological investigation of nanoparticles obtained from combined mechanical shearing, and enzymatic and acid hydrolysis of sisal fibers. Cellulose, **17**, 1147–1158 (2010).
DOI: 10.1007/s10570-010-9449-z

[10] Siqueira G., Tapin-Lingua S., Bras J., da Silva Perez D., Dufresne A.: Mechanical properties of natural rubber nanocomposites reinforced with cellulosic nanoparticles obtained from combined mechanical shearing, and enzymatic and acid hydrolysis of sisal fibers. Cellulose, **18**, 57–65 (2011).
DOI: 10.1007/s10570-010-9463-1

[11] Nickerson R. F., Habrle J. A.: Cellulose intercrystalline structure. Industrial and Engineering Chemistry Research, **39**, 1507–1512 (1947).
DOI: 10.1021/ie50455a024

[12] Cao X., Chen Y., Chang P. R., Muir A. D., Falk G.: Starch-based nanocomposites reinforced with flax cellulose nanocrystals. Express Polymer Letters, **2**, 502–510 (2008).
DOI: 10.3144/expresspolymlett.2008.60

[13] Wang S., Cheng Q.: A novel process to isolate fibrils from cellulose fibers by high-intensity ultrasonication, Part 1: Process optimization. Journal of Applied Polymer Science, **113**, 1270–1275 (2009).
DOI: 10.1002/app.30072

[14] Chakraborty A., Sain M., Kortschot M.: Cellulose microfibrils: A novel method of preparation using high shear refining and cryocrushing. Holzforschung, **59**, 102–107 (2005).
DOI: 10.1515/HF.2005.016

[15] Abe K., Iwamoto S., Yano H.: Obtaining cellulose nanofibers with a uniform width of 15 nm from wood. Biomacromolecules, **8**, 3276–3278 (2007).
DOI: 10.1021/bm700624p

[16] Nakagaito A. N., Yano H.: The effect of morphological changes from pulp fiber towards nano-scale fibrillated cellulose on the mechanical properties of high-strength plant fiber based composites. Applied Physics A: Materials Science and Processing, **78**, 547–552 (2004).
DOI: 10.1007/s00339-003-2453-5

[17] de Souza Lima M. M., Borsali R.: Rodlike cellulose microcrystals: Structure, properties, and applications. Macromolecular Rapid Communications, **25**, 771–787 (2004).
DOI: 10.1002/marc.200300268

[18] Saito T., Kimura S., Nishiyama Y., Isogai A.: Cellulose nanofibers prepared by TEMPO-mediated oxidation of native cellulose. Biomacromolecules, **8**, 2485–2491 (2007).
DOI: 10.1021/bm0703970

[19] Saito T., Nishiyama Y., Putaux J-L., Vignon M., Isogai A.: Homogeneous suspensions of individualized microfibrils from TEMPO-catalyzed oxidation of native cellulose. Biomacromolecules, **7**, 1687–1691 (2006).
DOI: 10.1021/bm060154s

[20] ASTM 1708-2002a: Standard test method for tensile properties of plastics by use of microtensile specimens (2002).

[21] Cheng Q., Wang S., Rials T. G., Lee S-H.: Physical and mechanical properties of polyvinyl alcohol and polypropylene composite materials reinforced with fibril aggregates isolated from regenerated cellulose fibers. Cellulose, **14**, 593–602 (2007).
DOI: 10.1007/s10570-007-9141-0

[22] Thygesen A., Oddershede J., Lilholt H., Thomsen A. B., Ståhl K.: On the determination of crystallinity and cellulose content in plant fibres. Cellulose, **12**, 563–576 (2005).
DOI: 10.1007/s10570-005-9001-8

[23] Johnson R. K., Zink-Sharp A., Renneckar S. H., Glasser W. G.: A new bio-based nanocomposite: Fibrillated TEMPO-oxidized celluloses in hydroxypropylcellulose matrix. Cellulose, **16**, 227–238 (2009).
DOI: 10.1007/s10570-008-9269-6

[24] Fengel D., Wegner G.: Wood-chemistry, ultrastructure, reactions. Walter de Gruyter, Berlin (1989).

[25] Khouri S.: Experimental characterization and theoretical calculations of responsive polymeric systems. Master's thesis University of Waterloo, Waterloo, Canada (2010).

[26] Cheng Q., Wang S., Harper D. P.: Effects of process and source on elastic modulus of single cellulose fibrils evaluated by atomic force microscopy. Composites Part A: Applied Science and Manufacturing, **40**, 583–588 (2009).
DOI: 10.1016/j.compositesa.2009.02.011

eXPRESS Polymer Letters Vol.6, No.10 (2012) 805–813
Available online at www.expresspolymlett.com
DOI: 10.3144/expresspolymlett.2012.86

Effect of tool geometry on friction stir spot welding of polypropylene sheets

*M. K. Bilici**

Marmara University, Technical Education Faculty, Department of Materials Technology, 34722 Istanbul, Turkey

Received 8 February 2012; accepted in revised form 3 May 2012

Abstract. The effects of tool geometry and properties on friction stir spot welding properties of polypropylene sheets were studied. Four different tool pin geometries, with varying pin angles, pin lengths, shoulder diameters and shoulder angles were used for friction stir spot welding. All the welding operations were done at the room temperature. Lap-shear tensile tests were carried out to find the weld static strength. Weld cross section appearance observations were also done. From the experiments the effect of tool geometry on friction stir spot weld formation and weld strength were determined. The optimum tool geometry for 4 mm thick polypropylene sheets were determined. The tapered cylindrical pin gave the biggest and the straight cylindrical pin gave the lowest lap-shear fracture load.

Keywords: *processing technologies, industrial applications, mechanical properties, polymer welding, friction stir spot welding*

1. Introduction

The friction stir welding (FSW) process was developed by TWI in 1991 for joining aluminium alloys [1]. Subsequently this welding process has been used for joining magnesium [2], titanium [3] and copper alloys [4], stainless steels [5], steels [6] and thermoplastics [7]. Friction stir spot welding (FSSW) is a version of the FSW process. It was developed in the automotive industry as an alternative for resistance spot welding of aluminium sheets in 2001 [8].

The FSSW process consists of three phases; plunging, stirring and retracting as shown in Figure 1. The process starts with the spinning of the tool at a high rotational speed. Then the tool is forced into the workpiece until the shoulder of the tool plunges into the upper workpiece. The plunge movement of the tool causes material to expel as shown in Figures 1a and 1b. When the tool reaches the predetermined depth, the plunge motion ends and the stirring phase starts. In this phase, the tool rotates in the workpieces without plunging. Frictional heat is generated in the plunging and the stirring phase and, thus, the material adjacent to the tool is heated and softened. The softened upper and lower workpiece materials mix together in the stirring phase. The shoulder of the tool creates a compressional stress on the softened material. A solid-state joint is formed in the stirring phase. When a predetermined bonding is obtained, the process stops and the tool is retracted from the workpieces. The resulting weld has a characteristic keyhole in the middle of the

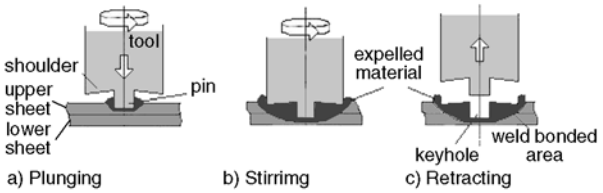

Figure 1. Three phases of friction stir spot welding process, (a) plunging, (b) stirring and (c) retracting

*Corresponding author, e-mail: mkbilici@marmara.edu.tr

joint as shown in Figure 1c. FSSW has been successfully applied to aluminium [9, 10], magnesium [11] and steel [12] sheets, but there are very few publications on polymer FSSW applications [13–16].

The welding parameters and the tool geometry affect friction stir welding and friction stir spot welding stir zonestir zone formation and weld strength [17]. The tool consists of two parts [18]: the shoulder and the pin. The pin generates friction heat, deforms the material around it and stirs the heated material [19]. In FSSW of metals the diameters of the pin [20], the pin angle [21], pin thread orientation [22], pin length [23] and pin profile [24] were found important in stir zonestir zone formation. The shoulder of the tool generates heat during the welding process, forges the heated material, prevents material expulsion and assists material movement around the tool [25]. The diameters of the shoulder and its concavity are also important in friction stir spot welding [26].

Based on the observations of the FSSW macrostructures, the weld zone of a FSSW joint is schematically illustrated in Figure 2. From the appearance of the weld cross section, two geometrical characteristics of the weld may be identified [27, 28]. The first is the thickness of the weld stir zonestir zone (x) which is an indicator of the weld bond area (Figure 2). The weld bond area increases with the stir zonestir zone thickness. The second is the thickness of the upper sheet under the shoulder indentation (y). These gerometircal characteristics determine the strength of a FSSW joint [18, 19]. There are numerous papers concerning the FSSW parameters which affect the joint geometry and the weld strength [16, 29, 30].

The quality of a spot weld is usually determined by a lap-shear test [31]. Standard lap-shear tests are used to find the joint strength of a resistance spot weld [32]. A standard for mechanical strength test for FSSW joints is not available presently. Therefore, in this study, the lap-shear test was used to determine the weld strength.

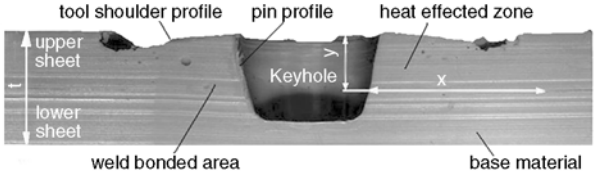

Figure 2. Schematic illustration of the cross section of a friction stir spot weld. *x:* stir zone thickness, *y:* the thickness of the upper sheet and *t:* total materials thickness

In FSW of metals improper welding parameters and tool geometry cause low mechanical strength and weld defects [33]. Therefore, in FSSW the welding parameters (tool rotational speed, dwell time, delay time, plunge depth and plunge rate) and the tool geometry (pin diameter, pin length, pin angle, pin profile, shoulder diameter and shoulder concavity angle) must be selected optimally [34]. There are a few studies about the FSSW tool geometry effects on thermoplastic sheets [13]. Thus, this study was intended to explain the tool geometry effects on FSSW of polypropylene sheets. The weld stir zone formation and lap-shear fracture loads were examined to reveal the tool effects.

2. Experiments

In this investigation 4 mm thick polypropylene sheets were used. Polypropylene sheets were purchased from SIMONA AG, Gemany (Tensile yield stress 34 MPa or lap shear fracture load 4500 N). 60 × 150 mm lap-shear specimens were cut from the sheets. In order to develop the FSSW tests, a properly designed clamping fixture was utilized to fix the specimens. The steel plates comprising the fixture ensure a uniform pressure distribution on the fixed specimens. Additionally, proper backing sheets were used in order to obtain the desired lap joints. A specimen had a 60 × 60 mm overlap area. The specimens were welded in a milling machine. The tools used in welding operations were machined from SAE 1040 steel and heat treated to 40 Rockwell C Hardness Conversion. The tool dimensions are shown in Figure 3. Four different tool pin profiles (straight cylindrical, tapered cylindrical, threaded cylindrical and square) were used to fabricate the joints (Fig-

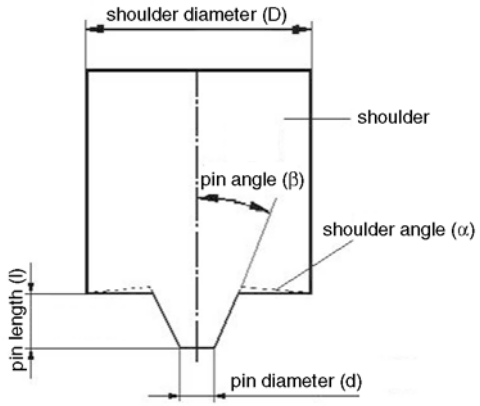

Figure 3. FSSW tool design showing geometric parameters

Table 1. The FSSW tool dimensions

Dimensions	Symbol	Units	Ranges
Shoulder diameter	*D*	millimeter [mm]	10–35
Pin length	*l*	millimeter [mm]	3.8–6.5
Pin angle	α	°	0–25
Shoulder angle	β	°	0–12

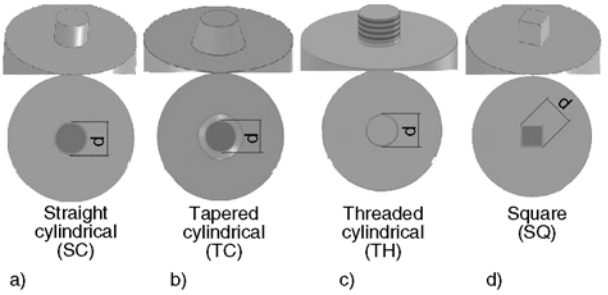

Figure 4. FSSW tool profile and pin size (*d*): a) straight cylindrical, b) tapered cylindrical, c) threaded cylindrical, d) square

ure 4). In straight cylindrical, tapered cylindrical and threaded cylindrical pins, the pin diameters was determined by measuring the bottom diameter of the pin. In the square pin, the pin diameter was determined by measuring the diagonal lengh of the bottom of the pin. A standard M8 thread cylindrical pin was formed. Then, the pin of the tool was milled to a 7.5 mm diameter. The tool dimensions and their ranges employed in this study are given in Table 1.

In this study, the welding parameters were selected from a previous publication. Optimum parameters obtained previously were selected for the experiments. The welding parameters were constant as 900 rpm tool rotational speed, 105 seconds dwell time and 50 seconds delay before retracting the tool. The rotating tool plunged into the upper sheet with a 0.33 mm/s plunge rate down to a 0.20 mm depth at an accuracy of ±0.02 mm [35]. The stirring phase of FSSW started with the completion of the tool plunging. In this phase, the tool rotated without plunging. The duration of this phase is called the dwell time. Upon reaching of the predetermined dwell time, the rotation of the tool was immediately stopped. The tool stayed in the weld zone for 50 seconds and then it was retracted. All the welding operations were done at the room temperature. Before welding each specimen the pin and the shoulder of the tool were cooled to the room temperature.

Welded lap-shear specimens were tested on an Instron machine at a constant crosshead speed of 5 mm/s. The fracture load was recorded during the test. The lap-shear fracture load was obtained by averaging the strengths of 5 individual specimens, which were welded with identical welding parameters. As a result of these experiments, the effect of tool properties on the lap-shear fracture load were investigated.

Weld cross section appearence observations of the joints were done with a video spectral comparator at 12.88X magnification. For macroscopic structure studies, thin slices (30 μm) were cut from the welded specimens using a Leica R6125 model rotary type microtome. These thin slices were investigated using a VSC-5000 model video spectral comparator. The photographs of the cross sections were obtained. So, the effect of tool properties on weld stir zone formation were investigated.

3. Results and discussion

The importance of the tool pin profile was shown in Figure 5. In these tests, each tool had a 7.5 mm pin diameter, a 5.5 pin length, 6° shoulder angle and 30 mm shoulder diameter. The tapered cylindrical pin had a 15° pin angle. The maximum fracture load was obtained with the tapered cylindrical pin (4032 N). The straight cylindrical pin profile gave the lowest fracture load (3305 N). The reason of this difference can be easily explained with the weld stir zone thicknesses which are shown in Figure 6. The straight cylindrical pin and tapered cylindrical pins have the same pin diameter (7.5 mm), but the weld stir zone thickness obtained by these pins are different. The stir zone thickness of the straight cylindrical is 7.5 mm as shown in Figure 6a. The 15° tapered cylindrical pin has a 8.4 mm weld stir zone thickness (Figure 6b).

These two photographs show that the tapered pin produced a bigger weld area. The lap-shear fracture

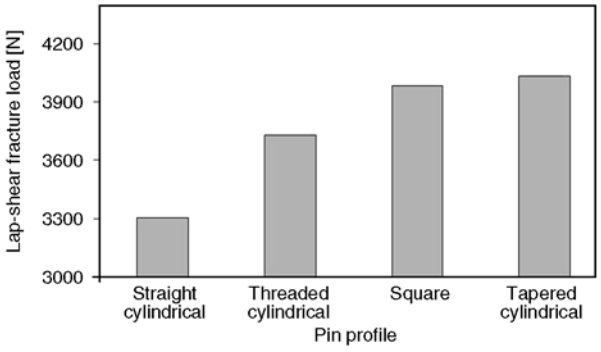

Figure 5. Lap shear fracture loads of different pin profiles

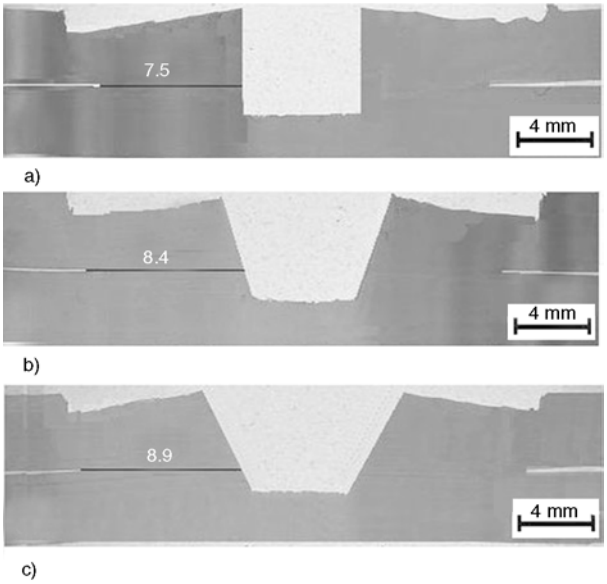

Figure 6. The effect of pin angle on weld stir zone formation. (a) straight cylindrical pin, (b) 15° pin angled tapered cylindrical pin and (c) 25° pin angled tapered cylindrical pin.

force of a FSSW joint is directly proportional to the stir zone thickness and the weld bond area [30]. In FSSW of thermoplastics the welding force effect of a pin increases with the pin angle [13]. The tapered pin produces more friction heat and a bigger weld thickness as shown in Figure 6. The heat produced in the weld area is directly propertional to the welding force [36, 37]. A high welding force produces more heat and a bigger weld area which causes a high weld strength [24]. Therefore, the tapered pin produces a higher welding force than the straight cylindrical pin [13]. Therefore, the strength of the 15° tapered pin is higher than that of the straight cylindrical pin. In Figure 5, it is shown that the threaded cylindrical pin's weld has a lower fracture load than the tapered pin's weld. This is an unexpected result. It was reported that the thread geometry [38], thread orientation [22] and thread pitch size [37] were important in metal FSSW operations. The effect of the lap-shear tensile fracture load and the tool pin angle on welding zone are shown in Figure 7 and Figure 6. Each tool had a 7.5 mm pin diameter, a 5.5 mm pin length, 6° shoulder angle, 30 mm shoulder diameter and from 0 to 25° pin angle. The photographs illustrate that the size of the keyhole which formed in the welding zone was directly dependent on the pin profile. The wall slope of the keyhole changed with the pin angle of the tool. The stir zone thickness is 7.5 mm for the

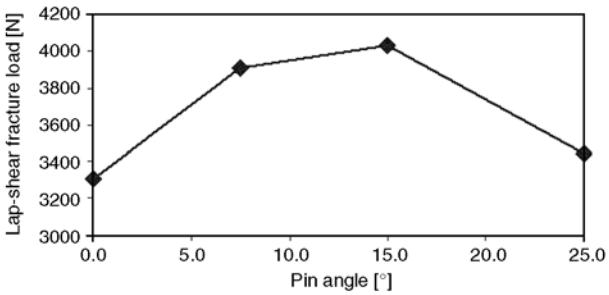

Figure 7. The effect of pin angle on the lap-shear fracture load

straight cylindrical pin, 8.4 mm for the 15° pin angled tapered pin and 8.9 mm for the 25° pin angled tapered pin. The tapered pins created thicker stir zone s than the straight cylindrical pin. The straight cylindrical pin which had a 0° pin angle gave the least fracture load. The fracture load increased with the pin angle up to 15° and then the fracture load reduced with the bigger pin angle. The stir zone thickness increased with the pin angle as shown in Figure 6. Although the 25° tapered cylindrical pin has a 8.9 mm weld stir zone thickness, weld strength was lower than the others. The 25° tapered cylindrical pin has produced more heat than the other tools. So, excessive heat and pressure will cause breakage of the chain structure. An excessive pin angle causes extra high friction heating which lowers the weld strength FSSW of thermoplastics.

In order to determine the effect of the thread pitch length on polypropylene FSSW, four different threaded cylindrical pins were produced. These pins are shown in Figure 8. The diameter of the each pin was 7.5 mm. The pitch length was varied between 0.8–2.0 mm. The pin length was 5.5 mm at each

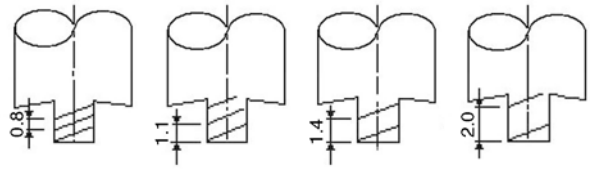

Figure 8. The geometry pitch length of theraded pins

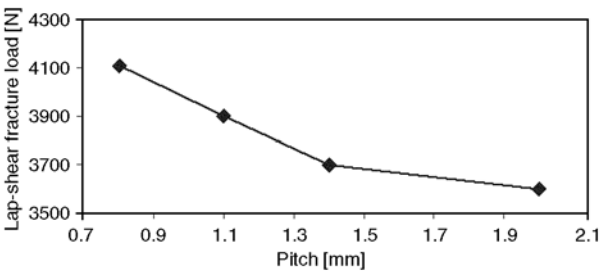

Figure 9. The effect of pitch length on lap shear fracture load

tool. The 30 mm tool shoulder diameter, 0° pin angle and 6° shoulder angle were constant in the tools. The effect of pitch length on lap-shear fracture load is shown in Figure 9. The fracture load decreased with the pitch length. During FSSW operations material expulsion increased with the pitch. This lowers the weld strength. The threaded cylindrical pin shown in Figure 5 had a 1.25 mm pitch. The fracture load obtained with the 0.8 mm pitch (Figure 9) is higher than the result of the 15° tapered pin and 1.25 mm pitch thread pin (Figure 5 and 9). That is why this pin gives a lower strength than the pin of 0.8 mm pitch. Increasing the threaded pitch punctures the materials as a drill [39]. So, shavings of material flow upward. In the FSSW process the most important point is that the shavings of the material must remain between the upper surface and the shoulder. If such conditions are not provided in the FSSW operation, welding will not occur. Therefore, threaded pitch was found to be important for the properties for FSSW.

Figure 10 shows the effect of the pin length on the weld fracture load. The tools used for these tests had a 30 mm shoulder diameter, 6° shoulder angle, 15° pin angle and 7.5 mm pin diameter. The pin length was varied between 3.8–6.5 mm. The fracture load was nearly zero when the weld was made with the 3.8 mm pin length tool. A weld was not formed between the sheets. The pin worked as a drill. The pin hardly plunged into the lower workpiece. Most of the drilled material of the upper sheet was expelled out, so a very small weld stir zone formed which gave a very small fracture load. The fracture load increased with the pin length up to 5.5 mm. The maximum lap-shear fracture load was obtained with the tool which had a 5.5 mm pin length. The pins which were longer than 5.5 mm gave smaller fracture loads. The weld cross sections

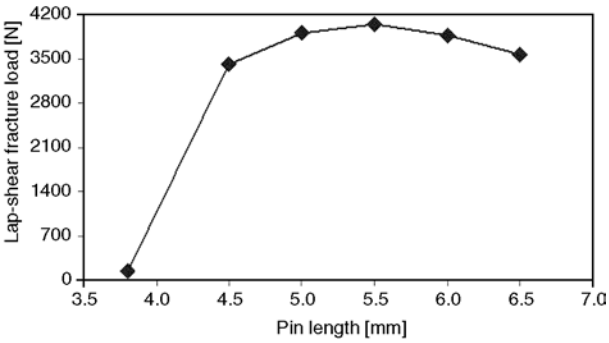

Figure 10. The effect of the pin length on the lap-shear fracture load

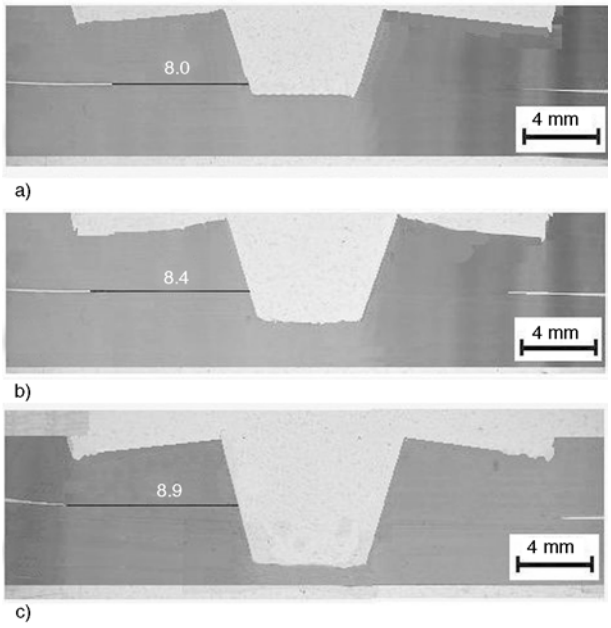

Figure 11. The effect of the pin length on the weld cross sections. (a) 4.5 mm pin length, (b) 5.5 mm pin length and (c) 6.5 mm pin length.

of these welds are shown in Figure 11. Therefore, it expelled the drilled material out of the welding zone. A small stir zone formed with this pin and only a 100 N fracture load was obtained as shown in Figure 11. The optimum pin length was determined as 5.5 mm. Longer pin lengths produced bigger weld bond area but lowered the fracture load. The weld strength and the weld stir zone thickness increased with the pin length (Figure 11).

Figure 12 illustrates the effect of the shoulder diameter on the lap-shear fracture load. All the tools used for these tests had a 6o shoulder angle, 15° pin angle, 7.5 mm pin diameter and 5.5 mm pin length. The shoulder diameter was varied between 10 and 35 mm. The lap-shear tensile force increased with the shoulder diameter up to 30 mm. Then the lap-shear fracture load reduced slightly with the increased shoul-

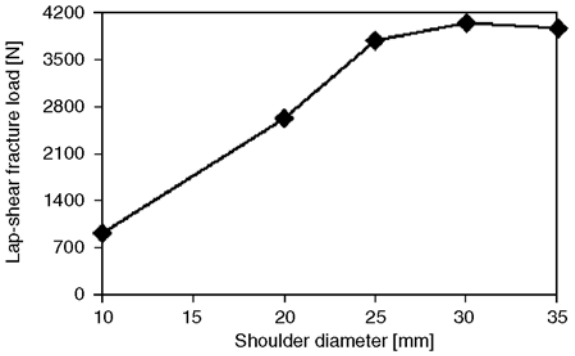

Figure 12. The effect of the shoulder diameter on the lap-shear fracture load

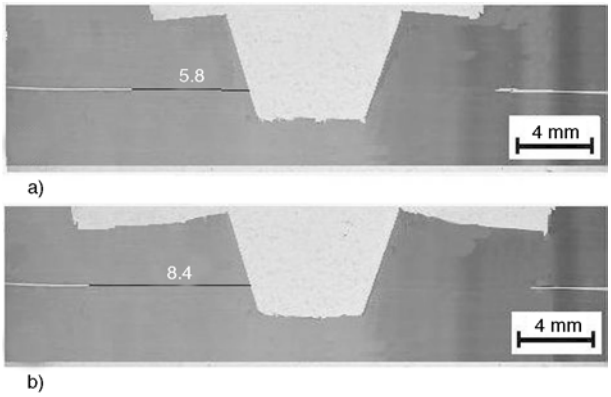

Figure 13. The effect of the shoulder diameter on the weld cross sections. (a) 20 mm shoulder diameter and (b) 30 mm shoulder diameter.

der diameter. The load increased with the shoulder diameter because a big shoulder produced more friction heat [13] and a bigger stir zone thickness [33] as shown in Figure 12. The best load was obtained with the 30 mm shoulder diameter. The weld stir zone thickness increased with the shoulder diameter as shown in Figure 13. The shoulder diameter is understood to be very important for produced the heat and pressure. FSSW process must be selected the most suitable diameter of the shoulder for weld quality.

The effect of the shoulder concavity angle on the weld strength was shown in Figure 14. Each tool used for these tests had a 30 mm shoulder diameter, 15° pin angle, 7.5 mm pin diameter and 5.5 mm pin length. The shoulder concavity angle was varied between 0.8–2.0 mm. The fracture load increased with the shoulder angle. The best load was obtained with the 6° shoulder angle. Increasing the shoulder angle beyond the 6° angle caused a decrease in the weld strength. Therefore, a very small stir zone thickness and a small fracture load were obtained. If the shoulder angle is above this angle a smaller weld strength was obtained. The flat shoulder didn't produce a healthy weld stir zone, because during the stirring period of the welding operation the stirred

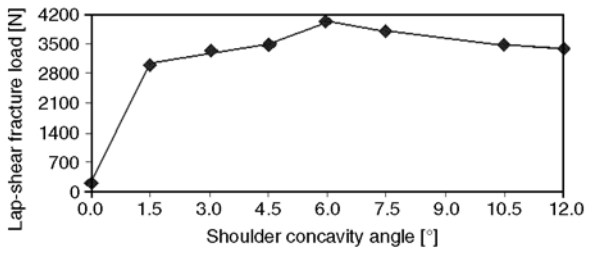

Figure 14. The effect of the shoulder angle on the lap-shear fracture load

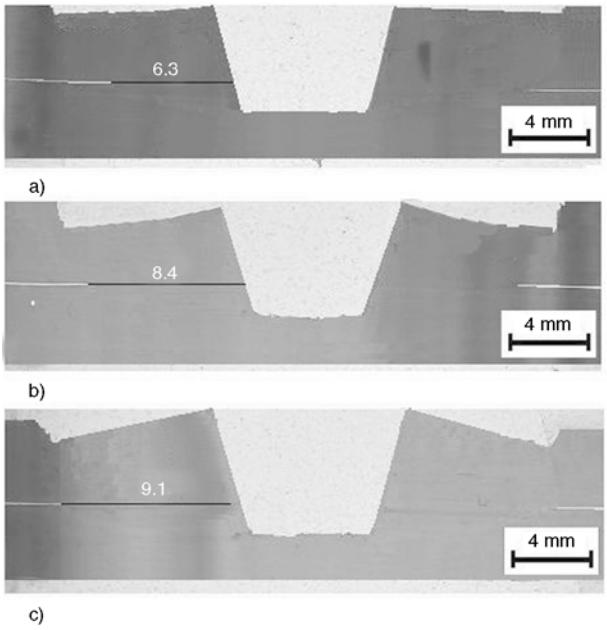

Figure 15. The effect of the shoulder angle on the joint cross section, (a) 1.5° shoulder angle tool, (b) 6° shoulder angle tool and (c) 12° shoulder angle tool

material was expelled out. A zero degree angle of the shoulder mustn't be used in FSSW experiments. In this study each mechanical test diagram shows an extremum. The lap-shear fracture load increases with the pin angle (Figure 15), the pin length (Figure 10), the shoulder diameter (Figure 12) and the shoulder concavity angle (Figure 14). All these diagrams indicate that there is an optimum value for each tool geometry variable. When the variable value exceeds the critical value, the weld strength starts decreasing. The size of the weld increased continously with the pin geometry variable (Figures 6, 11, 13 and 15). For example, the weld stir zone thickness increased with the pin angle (Figure 6). The lap-shear fracture load reached its highest value with the 15° pin angle (Figure 7). The fracture load of the 25° pin is less than the 15° pin. Although the 25° pin had a bigger weld thickness than the 15° pin (Figure 6), a lower fracture load was obtained with it. The reason of this strength difference is due to the chain scission [40]. Chain scission lowers the strength of a thermoplastic material [41]. If a molten thermoplastic material is heated to a high temperature and then a high pressure is applied to it, a decrease in the molecular weight of the material occurs [40]. The mechanical properties of thermoplastics decrease with lowering the molecular weight [42]. In FSSW the welding tool produces a compressive pressure

in the weld zone [27]. In FSSW of thermoplastics the material in the weld area melts [13]. Very high temperatures were recorded in FSW of plastics [15, 43]. High melt temperatures and high welding forces cause chain scission in the welding zone of the plastics which lowers the weld strength [44].

The physical properties of a polymer are strongly dependent on the size or length of the polymer chain. For example, as chain length is increased, melting and boiling temperatures increase quickly. Weld strength also tends to increase with chain length, as does the viscosity, or resistance to flow, of the polymer in its melt state. FSSW process produces high temperature and pressure. But excessive heat and pressure will cause to break the chain structure. Most of molten material was expelled out, so a very small weld stir zone formed which gave a very small fracture load. Thus, a reduction in weld strength occurs. In the friction stir welding is very important to check the excessive heat and pressure. Furtermore, tool geometry is very important in the production of heat and pressure.

4. Conclusions

The following results were derived from this study:

- The biggest tensile strength were obtained with threaded tool (Pitch length 0.8 mm, 7.5 mm pin diameter, 5.5 mm pin length, 30 mm shoulder diameter and 6° shoulder angle.
- In polypropylene FSSW, the weld tool geometry affects stir zone formation and weld lap-shear fracture load.
- The optimum straight tool geometry for 4 mm thick sheets was determined as 7.5 mm pin diameter, 15° pin angle, 5.5 mm pin length, 30 mm shoulder diameter and 6° shoulder angle.
- The weld strength obtained with a threaded pin decreases with the pitch. Pitch length of threaded pins are very important for the weld quality and the weld strength.
- Chain scission can occur in polypropylene FSSW, if excessive high friction heating is created in the weld zone.
- Excessive heat and pressure will cause to break the chain structure. So, the importance of controlling excessive heat and pressure was emerged.

Acknowledgements

This work was supported by Scientific Research Project Program of Marmara University (Project No. FEN-C-DRP-010710-230).

References

[1] Thomas W. M., Nicholas E. D.: Friction stir welding for the transportation industries. Materials and Design, **18**, 269–273 (1997). DOI: 10.1016/S0261-3069(97)00062-9

[2] Chowdhury S. M., Chen D. L., Bhole S. D., Cao X.: Tensile properties of a friction stir welded magnesium alloy: Effect of pin tool thread orientation and weld pitch. Materials Science and Engineering A, **527**, 6064–6075 (2010). DOI: 10.1016/j.msea.2010.06.012

[3] Knipling K. E., Fonda R. W.: Texture development in the stir zone of near-α titanium friction stir welds. Scripta Materialia, **60**, 1097–1110 (2009). DOI: 10.1016/j.scriptamat.2009.02.050

[4] Meran C.: The joint properties of brass plates by friction stir welding. Materials and Design, **27**, 719–726 (2006). DOI: 10.1016/j.matdes.2005.05.006

[5] Zhu X. K., Chao J. Y.: Numerical simulation of transient temperature and residual stresses in friction stir welding of 304L stainless steel. Journal of Materials Processing Technology, **6**, 125–133 (2004). DOI: 10.1016/j.jmatprotec.2003.10.025

[6] Chung Y. D., Fujii H., Ueji R., Tsuji N.: Friction stir welding of high carbon steel with excellent toughness and ductility. Scripta Materialia, **63**, 223–226 (2007). DOI: 10.1016/j.scriptamat.2010.03.060

[7] Kiss Z., Czigány T.: Microscopic analysis of the morphology of seams in friction stir welded polypropylene. Express Polymer Letters, **6**, 54–62 (2012). DOI: 10.3144/expresspolymlett.2012.6

[8] Hancock R.: Friction welding of aluminium cuts energy cost by 99%. Welding Journal, **83**, 40 (2004).

[9] Lin P-C., Pan J., Pan T.: Failure modes and fatigue life estimations of spot friction welds in lap-shear specimens of aluminum 6111-T4 sheets. Part 1: Welds made by a concave tool. International Journal of Fatigue, **30**, 74–89 (2008). DOI: 10.1016/j.ijfatigue.2007.02.016

[10] Merzoug M., Mazari M., Berrahal L., Imad A.: Parametric studies of the process of friction spot stir welding of aluminium 6060-T5 alloys. Materials and Design, **31**, 3023–3028 (2010). DOI: 10.1016/j.matdes.2009.12.029

[11] Chen Y. C., Nakata K.: Effect of tool geometry on microstructure and mechanical properties of friction stir lap welded magnesium alloy and steel. Materials and Design, **30**, 3913–3919 (2009). DOI: 10.1016/j.matdes.2009.03.007

[12] Khan M. I., Kuntz M. L., Su P., Gerlich A., North T., Zhou Y.: Resistance and friction stir spot welding of DP600: A comparative study. Science and Technology of Welding and Joining, **12**, 175–182 (2007). DOI: 10.1179/174329307X159801

[13] Bilici M. K., Yükler A. I.: Influence of tool geometry and process parameters on macrostructure and static strength in friction stir spot welded polyethylene sheets. Materials and Design, **33**, 145–152 (2012). DOI: 10.1016/j.matdes.2011.06.059

[14] Arici A., Mert S.: Friction stir spot welding of polypropylene. Journal of Reinforced Plastics and Composites, **27**, 2001–2004 (2008). DOI: 10.1177/0731684408089134

[15] Oliveria P. H. F., Amancio-Filho S. T., dos Santos J. F., Hage E.: Preliminary study on the feasibility of friction spot welding in PMMA. Materials Letters, **64**, 2098–2101 (2010). DOI: 10.1016/j.matlet.2010.06.050

[16] Bilici M. K., Yükler A. I., Kurtulmuş M.: The optimization of welding parameters for friction stir spot welding of high density polyethylene sheets. Materials and Design, **32**, 4074–4079 (2011). DOI: 10.1016/j.matdes.2011.03.014

[17] Rodrigues D. M., Loureiro A., Leitao C., Leal R. M., Chaparro B.M., Vilaça P.: Influence of friction stir welding parameters on the microstructural and mechanical properties of AA 6016-T4 thin welds. Materials and Design, **30**, 1913–1921 (2009). DOI: 10.1016/j.matdes.2008.09.016

[18] Mishra R. S., Ma Z. Y.: Friction stir welding and processing. Materials Science and Engineering R: Reports, **50**, 1–78 (2005). DOI: 10.1016/j.mser.2005.07.001

[19] Su P., Gerlich A., North T. H.: Friction stir spot welding of aluminum and magnesium alloy sheets. SAE Technical Paper. 2005-01-1255 (2005). DOI: 10.4271/2005-01-1255

[20] Kulekci M. K., Şik A., Kaluç E.: Effects of tool rotation and pin diameter on fatigue properties of friction stir welded lap joints. The International Journal of Advanced Manufacturing Technology, **36**, 877–882 (2008). DOI: 10.1007/s00170-006-0901-z

[21] Hirasawa S., Badarinarayan H., Okamoto K., Tomimura T., Kawanami T.: Analysis of effect of tool geometry on plastic flow during friction stir spot welding using particle method. Journal of Materials Processing Technology, **210**, 1455–1463 (2010). DOI: 10.1016/j.jmatprotec.2010.04.003

[22] Chowdhury S. M., Chen D. L., Bhole S. D., Cao X.: Effect of pin tool thread orientation on fatigue strength of friction stir welded AZ31B-H24 Mg butt joints. Procedia Engineering, **2**, 825–833 (2010). DOI: 10.1016/j.proeng.2010.03.089

[23] Tozaki Y., Uematsu Y., Tokaji K.: Effect of tool geometry on microstructure and static strength in friction stir spot welded aluminium alloys. International Journal of Machine Tools and Manufacture, **47**, 2230–2236 (2007). DOI: 10.1016/j.ijmachtools.2007.07.005

[24] Vijay S. J., Murugan N.: Influence of tool pin profile on the metallurgical and mechanical properties of friction stir welded Al–10 wt.% TiB_2 metal matrix composite. Materials and Design, **31**, 3585–3589 (2010). DOI: 10.1016/j.matdes.2010.01.018

[25] Yang Q., Mironov S., Sato Y. S., Okamoto K.: Material flow during friction stir spot welding. Materials Science and Engineering A, **527**, 4389–4398 (2010). DOI: 10.1016/j.msea.2010.03.082

[26] Badarinarayan H., Yang Q., Zhu S.: Effect of tool geometry on static strength of friction stir spot-welded aluminum alloy. International Journal of Machine Tools and Manufacture, **49**, 142–148 (2009). DOI: 10.1016/j.ijmachtools.2008.09.004

[27] Gerlich A., Yamamoto M., North T. H.: Local melting and cracking in Al 7075-T6 and Al 2024-T3 friction stir spot welds. Science and Technology of Welding and Joining, **12**, 472–480 (2007). DOI: 10.1179/174329307X213873

[28] Tozaki Y., Uematsu Y., Tokaji K.: Effect of processing parameters on static strength of dissimilar friction stir spot welds between different aluminium alloys. Fatigue and Fracture of Engineering Materials and Structures, **30**, 143–148 (2007). DOI: 10.1111/j.1460-2695.2006.01096.x

[29] Badarinarayan H., Shi Y., Li X., Okamoto K.: Effect of tool geometry on hook formation and static strength of friction stir spot welded aluminum 5754-O sheets. International Journal of Machine Tools and Manufacture, **49**, 814–823 (2007). DOI: 10.1016/j.ijmachtools.2009.06.001

[30] Feng Z., Santella M. L., David S., Steel R. J., Packer S. M., Pan T., Kuo M., Bhatnagar R. S.: Friction stir spot welding of advanced high-strength steels – A feasibility study. SAE Technical Paper, 2005-01-1248 (2005). DOI: 10.4271/2005-01-1248

[31] Goodarzi M., Marashi S. P. H., Pouranvari M.: Dependence of overload performance on weld attributes for resistance spot welded galvanized low carbon steel. Journal of Materials Processing Technology, **209**, 4379–4384 (2009). DOI: 10.1016/j.jmatprotec.2008.11.017

[32] ANSI/AWS C1.4:2009: Specification for resistance welding of coated and uncoated carbon and low alloy steels (2007).

[33] Elangovan K., Balasubramanian V.: Influences of tool pin profile and welding speed on the formation of friction stir processing zone in AA2219 aluminium alloy. Journal of Materials Processing Technology, **200**, 163–175 (2008). DOI: 10.1016/j.jmatprotec.2007.09.019

[34] Yuan W., Mishra R. S., Webb S., Chen Y. L., Carlson B., Herling D. R., Grant G. J.: Effect of tool design and process parameters on properties of Al alloy 6016 friction stir spot welds. Journal of Materials Processing Technology, **211**, 972–977 (2011).
DOI: 10.1016/j.jmatprotec.2010.12.014

[35] Bilici M. K.: Application of Taguchi approach to optimize friction stir spot welding parameters of polypropylene. Materials and Design, **35**, 113–119 (2012).
DOI: 10.1016/j.matdes.2011.08.033

[36] Awang M., Mucino V. H., Feng Z., David S. A.: Thermo-mechanical modeling of friction stir spot welding (FSSW). SAE International, 2006-01-1392 (2006).
DOI: 10.4271/2006-01-1392

[37] Ma N., Kunugi A., Hirashima T., Okubo K., Kamioka M.: FEM simulation for friction spot joining process. Welding International, **23**, 9–14 (2009).
DOI: 10.1080/09507110802348892

[38] Hattingh D. G., Blignault C., van Niekerk T. I., James M. N.: Characterization of the influences of FSW tool geometry on welding forces and weld tensile strength using an instrumented tool. Journal of Materials Processing Technology, **203**, 46–57 (2008).
DOI: 10.1016/j.jmatprotec.2007.10.028

[39] Boz M., Kurt A.: The influence of stirrer geometry on bonding and mechanical properties in friction stir welding process. Materials and Design, **25**, 343–347 (2004).
DOI: 10.1016/j.matdes.2003.11.005

[40] da Costa H. M., Ramos V. D., Rocha M. C. G.: Rheological properties of polypropylene during multiple extrusion. Polymer Testing, **24**, 86–93 (2005).
DOI: 10.1016/j.polymertesting.2004.06.006

[41] Capone C., Di Landro L., Inzoli F., Penco M., Sartore L.: Thermal and mechanical degradation during polymer extrusion processing. Polymer Engineering and Science, **47**, 1813–1819 (2007).
DOI: 10.1002/pen.20882

[42] Sung J. H., Lim S. T., Kim C. A., Chung H., Choi H. J.: Mechanical degradation kinetics of poly(ethylene oxide) in a turbulent flow. Korea-Australia Rheology Journal, **16**, 57–62 (2004).

[43] Aydin M.: Effects of welding parameters and pre-heating on the friction stir welding of UHMW-polyethylene. Polymer-Plastics Technology and Engineering, **49**, 595–601 (2010).
DOI: 10.1080/03602551003664503

[44] Gan Y. X., Salomon D., Reinbolt M.: Friction stir processing of particle reinforced composite materials. Materials, **3**, 329–350 (2010).
DOI: 10.3390/ma3010329

eXPRESS Polymer Letters Vol.6, No.10 (2012) 814–825
Available online at www.expresspolymlett.com
DOI: 10.3144/expresspolymlett.20187.87

Utilization of poly(methyl methacrylate) – carbon nanotube and polystyrene – carbon nanotube *in situ* polymerized composites as masterbatches for melt mixing

*M. Annala, M. Lahelin, J. Seppälä**

Aalto University School of Chemical Technology, Department of Biotechnology and Chemical Technology, Polymer Technology Research Group, P.O. Box 16100, FI-00076 Aalto, Finland

Received 15 March 2012; accepted in revised form 6 May 2012

Abstract. Carbon nanotubes (CNTs) were melt mixed directly or by using an *in situ* polymerized masterbatch into a matrix polymer, polystyrene (PS) or poly(methyl methacrylate) (PMMA). The mechanical properties of the composites were mostly determined by the amount of CNTs, and not by the use of directly melt mixed CNTs or the use of the masterbatch. In contrast, the electrical resistivity of the composites was dependent on the manner in which the CNTs were added to the matrix polymer. When there was increased interfacial adhesion between the components, as for PS and the CNTs, the use of directly melt mixed CNTs gave better resistivity results. Without strong interactions between the CNTs and the matrix, as with PMMA and CNTs, the use of a tailored masterbatch had a significant effect on properties of the final composites. The molecular weight and viscosity of masterbatches can be varied and when the PMMA-masterbatch had optimized viscosity with respect to the PMMA matrix, electrical resistivity of the final composites decreased noticeably.

Keywords: *polymer composites, nanocomposites, material testing, tailor-made polymers, carbon nanotubes*

1. Introduction

Carbon nanotubes (CNTs) are unique materials with superior mechanical, thermal and electrical properties. CNTs are of increasing interest both in the academic and industrial worlds for use as fillers in polymer composites in which low mass, electrical conductivity and mechanical strength are required. In general, the challenge for controlling and predicting nanocomposite properties lies in understanding interfacial phenomena between the particles and polymers. The dispersion of the CNTs in the matrix polymer and interfacial adhesion between the CNTs and polymers are the two major factors that determine the reinforcement effect of the CNTs. Compromises have to be made in order to obtain high reinforcement and electrical conductivity in the resulting composite. The orientation of the CNTs in composites has contradictory effects on the properties of the composite. Well-aligned CNTs in the composite improve mechanical properties [1, 2]. Tensile toughness of poly(methyl methacrylate) (PMMA) increased 170% after addition of 1 wt% CNTs, which were oriented in the matrix [1]. On the other hand, electrical conductivity decreases in well-aligned CNTs [3–5]. In PMMA composites with 2 wt% CNTs, the nanotube alignment decreased the electrical conductivity from 10^{-4} S/cm (unaligned) to 10^{-10} S/cm (aligned) [4]. Electrical conductivity of the composites is based on the continuous network of the conductive phase throughout the composite. There are many factors to be considered when the conductivity of a composite is to be optimized. The CNTs are mainly concentrated in the amorphous phase of the matrix, and when the crystallinity of the matrix

*Corresponding author, e-mail: jukka.seppala@aalto.fi

increases, the concentration of the CNTs increases in the amorphous phase by increasing the conductivity of the composite [6].

CNTs, having high surface energy and strong van der Waals interactions, are difficult to disperse in the matrix polymer on the nanoscale level through simple mixing. Conventional mixing in solution or melt mixing usually gives nanoscale dispersion of CNTs with poor stability [7]. Yet direct melt mixing and the use of a masterbatch are highly desired processing methods in many applications which require highly stabile dispersions.

Direct melt mixing is not sufficient for breaking up CNT agglomerates and dispersing the CNTs into the matrix polymer when interfacial interactions are poor between the CNTs and the matrix polymer. Chemically modified CNTs are more soluble than pristine nanotubes and are more easily incorporated into a matrix polymer, including when using melt mixing. Using functionalized CNTs and a compatibilizer, Jin *et al*. [8] have managed to improve the dispersion of the CNTs in a polypropylene matrix in melt mixing. Lin *et al*. [9] have studied the mixing conditions in different melt mixers and the effect of shear on CNT agglomerates during mixing. Isayev *et al*. [10] have prepared an ultrasonic-assisted extruder for direct melt mixing, which enhanced the dispersion of the CNTs in polyetherimide. When composites are prepared by melt processing, the crystallinity of the matrix polymer affects both the mechanical properties and electrical conductivity of the composite. Coleman *et al*. [11] have determined that rather than acting as reinforcing agents, the major role played by the CNTs in improving the mechanical properties of composites is to nucleate polymer crystallization. The same phenomena have been observed with polypropylene-CNT composites [6, 12]. In the case of the PP-CNT composite, the mechanical properties, elongation at break and impact strength, decreased as the amount of CNTs in the composite increased. With only a small amount of CNTs, 0.5 wt%, the mechanical properties were improved, which was attributed to increased matrix crystallinity. Yet the percolation threshold was at 8.0 wt% CNTs [13]. In addition, a polyamide 6-CNT composite was produced in which the crystallinity increased after addition of CNTs and mechanical properties were improved [14, 15].

To use a masterbatch, the CNTs are first dispersed in one polymer, and this composite is then melt blended with a second polymer. Melt mixing in extruders has provided a reasonably economical way to produce a wide range of polymer blends. The improvement in mechanical properties of a blend requires that the phase of the matrix polymer is continuous, and that there is sufficient adhesion between the phases. In melt mixing, phase separation can be controlled by adjusting the viscosity ratios [16] and shear rates [17] to achieve a morphology in which both phases are continuous or the CNT-rich polymer phase is continuous. In such blends, double percolation can be exploited to minimize the CNT content in the composite [18, 19]. In polyamide 6-CNT composites, the percolation threshold was between 4–6 wt% CNTs. When this composite was blended with acrylonitrile/butadiene/styrene (ABS), the CNTs were selectively located in the polyamide-6, and percolation threshold decreased to 2–3 wt% CNTs [18]. Depending on the conditions, the CNTs can reorganize during melt mixing by diffusion. The diffusivity of the CNTs is determined by the viscosity of the matrix polymer and thus the extent at which they can reorganize [20]. The thermodynamically-driven migration effect can be used to obtain well-dispersed CNTs in a matrix polymer. Pötschke *et al*. [21] have used a polyethylene-CNT masterbatch in extrusion with polycarbonate or polyamide. The CNTs diffused into matrix polymers that had lower interfacial energies with the CNTs. Electrical percolation was achieved at a lower CNT content than that needed with direct incorporation of the CNTs.

To obtain only mechanical improvements, Yuan *et al*. [22] prepared a polystyrene-CNT masterbatch by using *in situ* polymerization of styrene to coat the CNTs with polystyrene, and the masterbatch was diluted with melt mixing. They managed to enhance impact strength 250% compared with pure PS by adding 0.3 wt% CNTs to the composite, while maintaining the good dispersion of the CNTs. Tong *et al*. [23] coated the CNTs with polyethylene and after melt mixing with matrix polyethylene, the mechanical properties were similar to those of the matrix polymer; without coating the CNTs, poor mechanical properties obtained.

In this paper, we demonstrate the benefit of using the *in situ* polymerized composites as a master-

batch. We have previously used *in situ* polymerization to form stable dispersions of CNTs in two different types of polymers, polystyrene and poly (methyl methacrylate) [24]. The properties of the *in situ* polymerized masterbatch can be tailored based on the desired viscosity to form conductive paths in the final composites. The viscosity of a masterbatch can be optimized by changing the molecular weight of a masterbatch and/or by adding plasticizer. We show that the addition of a plasticizer is an easy way to alter the viscosity of materials. We studied the effect of CNTs, both type and amount of CNT, in *in situ* emulsion and combined emulsion/suspension polymerization of styrene and methyl methacrylate. Based on the results, the preparation method of masterbatches was selected in order to obtain high content of CNTs and appropriate molecular weight of the masterbatch. Significant improvements for lowering resistivity of PMMA-CNT composite was achieved by using *in situ* polymerized masterbatch.

2. Materials and methods

2.1. Materials

Monomers styrene (>99%, Fluka, Steinheim, Germany) and methyl methacrylate (MMA, >99%, Fluka, Steinheim, Germany) were treated with aluminum oxide (Fluka, Steinheim, Germany) to remove inhibitor, initiators potassium peroxodisulfate (KPS, Fluka, Steinheim, Germany) and azobisisobutyronitrile (AIBN, Fluka, Switzerland), surfactant sodium dodecyl benzene sulfate (DBSA, Fluka), buffer sodium hydrogen carbonate ($NaHCO_3$, Merck), plasticizer glycerol (>99%, Merck), and multi-walled carbon nanotubes (CNTs, NC7000, Nanocyl, Sambreville, Belgium) were used as received. CNTs has been manufactured via a chemical vapor deposition (CVD) process, the carbon purity is ~90%, average diameter ~9.5 nm, and average length ~1.5 μm according to manufacturer. All water used was distilled. Matrix polymers polystyrene (PS, Styron 678E, Styron Europe GmbH, Horgen, Switzerland) and poly(methyl methacrylate) (PMMA, IG840, LG Chemicals, Korea) were milled before melt mixing.

2.2. *In situ* – polymerization of masterbatches

The molecular weight of a polymer depends on the polymerization method and the amount of CNTs in the *in situ* polymerization reaction [24]. Therefore two polymerization techniques were used in order to control the molecular weights: emulsion polymerization with KPS as an initiator and combined emulsion/suspension polymerization with AIBN as an initiator. PMMA-masterbatch was prepared by using emulsion polymerization method with 10 wt% CNTs in order to get molecular weight that approaches the molecular weight of commercial PMMA matrix. High molecular weight PS-masterbatch was prepared by using the emulsion polymerization method with 12 wt% CNTs and low molecular weight PS-masterbatch by using combined emulsion/suspension method with 6 wt% CNTs.

At first, a seed emulsion was prepared. The CNTs, 0.5 g surfactant, 0.1 g buffer, and 90/100 mL water were introduced into a 250 mL three-neck round bottom flask, cooled in an ice bath, and the mixture was deoxygenated with argon. Ultrasonic irradiation was carried out with the probe of the ultrasonic horn immersed directly into the mixed system. The power output was set at 100 W and the system was irradiated 30 min. After ultrasonic treatment, the flask was transferred into an oil bath and fitted with a stirrer under argon atmosphere.

In the case of the emulsion polymerization, 0.09 g initiator (KPS) was dissolved in 10 mL water and the solution was fed into the seed emulsion before monomer feed. The monomer (5 mL) was added dropwise with a membrane pump at 0.03 mL/min to control the growing polymer particles in the emulsion. Polymerizations were conducted with a stirring rate of 300 rpm under argon atmosphere for 15–18 h at 60°C for PMMA-masterbatches and at 70°C for PS-masterbatches.

In the case of the combined emulsion/suspension polymerization, 0.045 g initiator (AIBN) was dissolved in 5 mL of styrene and the solution was fed into the seed emulsion with the membrane pump at 0.03 mL/min. Polymerization was conducted with stirring rate of 300 rpm under argon atmosphere for 3 h at 80°C.

The emulsions were dried at 50°C in an oven overnight. To adjust the viscosity of a masterbatch, a plasticizer (30 wt% or 50 wt% based on monomer content) was added to the emulsion before drying. The masterbatches with added plasticizer are referred to as plast30 and plast50, respectively.

2.3. Melt mixing

The composites were prepared with a corotating twin-screw midiextruder (DSM, Pforzheim, Germany; capacity = 16 cm^3; screw length L = 150 mm) under nitrogen atmosphere. In the case of PS composites, different screw speeds, 60/80/120 rpm, and mixing times, 5/10/15 min, were tested at 190°C. PMMA composites were mixed at 120 rpm for 10 min at 210°C. The CNT content in composites was 1–4 wt% and the CNTs were incorporated directly or by using a masterbatch. The masterbatches were in powder form after drying. In order to obtain favorable phase morphology of the masterbatches in the final composite, matrix polymers were milled. The particle size of the masterbatch varied from fine powder to coarse powder, because some agglomeration of polymer pearls occurred during drying. Therefore matrix polymers were milled to a fine powder with particle size less than 500 μm. The components were mixed together before feeding into the midiextruder. The samples were designated based on the content of CNTs in the composite, followed by how CNTs were incorporated, directly (CNTs) or with masterbatch (MB), and the matrix polymer.

2.4. Characterization

Molecular weights (M_w) and molecular weight distributions (D) were determined with respect to polystyrene standards by size exclusion chromatography (SEC, The Waters Associates system, USA). The samples were dissolved in tetrahydrofuran (THF) and THF was used as eluent. The samples were analyzed at room temperature.

Mechanical properties of the composites were characterized from hot-pressed samples (hot-press, Fontijne TP 400, the Netherlands). The used melting and pressing temperatures and times were 170°C/5 min for PS and 165°C/4 min for PMMA. The used pressure was 150 kN. Tensile tests were performed with an Instron 4202 testing machine (Instron, United Kingdom) using a test speed of 5 mm/min and with specimen type 1BA according to the standard ISO 527:1993(E).

The bulk resistivity of the composites was measured by the four-probe method (Keithley 2400 Sourcemeter, USA). Alligator clips were used as electrodes and the electrodes were placed in the middle of the tensile test specimen. The cross sectional area of the tensile test specimen was 0.075 cm^2. The distance between the clips was 1 mm. The measurement was repeated three times per sample and the electrical resistivity was determined as an average value.

Thermal analyses with differential scanning calorimetry (Mettler Toledo DSC 821, Switzerland) using a heating rate of 10°C/min from 25°C to 190°C with PS and to 220°C with PMMA were carried out to determine the glass transition temperatures, T_g.

The melt rheological properties of the masterbatches were determined indirectly from the final composites by using a rotation rheometer (Anton Paar Physica MCR 301, Austria) with parallel plate geometry, gap 0.4 mm, at 190°C for PS and at 210°C for PMMA, using dynamic oscillation frequency sweeps of 0.1–100 rad/s under nitrogen atmosphere. The morphology of the composites was characterized with a field emission scanning electron microscope (SEM, JSM-6335F JEOL, Tokyo, Japan). The extrudates were fractured after cooling in liquid nitrogen, and the fractured surfaces were sputter-coated with platinum under argon. The electron micrographs were taken using an acceleration voltage of 5.0 kV.

3. Results and discussion

We have investigated a number of parameters that can affect the final properties of CNT composites. The purpose was to obtain a conductive composite, and the mechanical properties were determined for chosen samples based on their electrical performance. Two different polymers were chosen as matrix polymers. The first was polystyrene, which has a compatible structure with CNTs, and interactions were based on π-stacking. The latter was poly(methyl methacrylate), which does not have favorable groups in the backbone or the side chain to form strong interactions with CNTs. All properties, i.e. resistivity and mechanical properties, were analyzed from unoriented CNT composite samples.

There are only limited possibilities to affect shear forces in the midiextruder to disperse the CNTs into the matrix polymer. Therefore, the particle size of the matrix polymers was reduced by milling in order to improve the dispersion of CNTs in the final composites. The effect of various mixing times and rotation speeds on the dispersion of CNTs was studied with polystyrene, which have strong interactions

Table 1. The electrical resistivity and mechanical properties of polystyrene samples; melt mixing parameters were 10 min and 120 rpm, if not marked otherwise

Sample	CNT content [wt%]	Electrical resistivity [Ω·cm]	Young's modulus [MPa]	Tensile strength [MPa]	Strain [%]
PS	–	10^{20}–10^{22} a)	1170±43	34±2	3.3±0.2
1 CNTs/PS	1	$>10^9$	1130±24	28±3	2.8±0.3
1 $MB_{PS,KPS}$/PS	1	$>10^9$	1210±48	31±4	3.0±0.1
2 CNTs/PS	2	$1.1\cdot10^5$	1170±58	20±8	2.1±0.7
2 $MB_{PS,KPS}$/PS	2	$2.0\cdot10^7$	1290±71	30±3	2.8±0.4
2 $MB_{PS,KPS}$/PS 5 min/120 rpm	2	$>10^9$	–	–	–
2 $MB_{PS,KPS}$/PS 5 min/60 rpm	2	$>10^9$	–	–	–
2 $MB_{PS,KPS}$/PS 10 min/60 rpm	2	$>10^9$	–	–	–
2 $MB_{PS,AIBN}$/PS	2	$2.6\cdot10^7$	1180±58	22±10	2.2±0.9
2 $MB_{PS,AIBN}$ plast30/PS	2	$1.1\cdot10^5$	990±30	18±3	2.2±0.5
3 CNTs/PS	3	650	1170±53	18±7	1.8±0.4
4 CNTs/PS	4	180	1220±26	28±1	2.5±0.1

a)The resistivity of pure PS is a literature value, from ref [25]

with the CNTs. Based on the conductivity of the composites, the most efficient combination of mixing time and rotation speed was 120 rpm and 10 min (Table 1). This combination was the best for preparing both the directly melt mixed CNT composites and the masterbatch composites of polystyrene.

In general, the resistivity decreased when the CNT content increased in the composites. PS composites were conductive with CNT loading of 1–2 wt% (Table 1). Due to the compatible structure of the CNTs and polystyrene, CNTs disperse more easily into the PS matrix, and the directly melt mixed PS-CNT composites were conductive with CNT loading of 1–2 wt%. By using a masterbatch, the same conductivity level with the same CNT loading was achieved in the final composite. However, the properties of a masterbatch affected greatly to the conductivity of the final PS composite. When the masterbatch was used, the properties of the masterbatch were needed to optimize in order to achieve the conductive composite.

The molecular weight of matrix polymers affects the mechanical and rheological properties [25, 26]. Therefore, the molecular weights were analyzed by rheometry. Based on the rheological model of the volume fraction (ϕ) and viscosity (η), phase continuity and inversion in polymer blends and simultaneous interpenetrating networks can be predicted (Equation (1)) [16]:

$$\frac{\eta_1}{\eta_2} = \frac{\phi_2}{\phi_1} \cong 1 \quad (1)$$

The matrix polymers have quite low molecular weights compared to the masterbatches (Table 2).

Table 2. Molecular weights (M_w), molecular weight distributions (PD), and glass transition temperatures (T_g)

Sample	CNT content [wt%]	M_w [g/mol]	PD	T_g [°C]
PS, powder	–	260 000	2.5	87
MB_{PS} (KPS)	12	1 450 000	3.3	89
MB_{PS} (AIBN)	6	630 000	3.4	107
MB_{PS} (AIBN) plast30	6	630 000	3.4	106
PMMA, powder	–	93 000	1.9	106
MB_{PMMA}	10	280 000	3.8	123
MB_{PMMA} plast30	10	280 000	3.8	118

The final PS composites with the high molecular weight PS-masterbatch were conductive below 3 wt% CNTs. However, directly melt mixed PS-CNT composites were already conductive below 2 wt% CNTs.

The morphology of the composite is affected by the viscosity of the masterbatch, thus rheological measurements were carried out. The viscosities of masterbatches could not be measured directly due to instrument limitations, therefore the measurements were performed with the final composites. Indirect measurements of rheological properties of the materials revealed that the addition of CNTs increased the viscosity and dynamic moduli of the composites (Figures 1–2). The viscosity of the final PS composites was highest when the masterbatches were used, as the higher molecular weight of the polymer induces a higher viscosity (Figure 1).

The viscosity of the PS matrix increased after addition of CNTs (Figure 1). There was also a notable difference between the high molecular weight PS-masterbatch and the low molecular weight PS-mas-

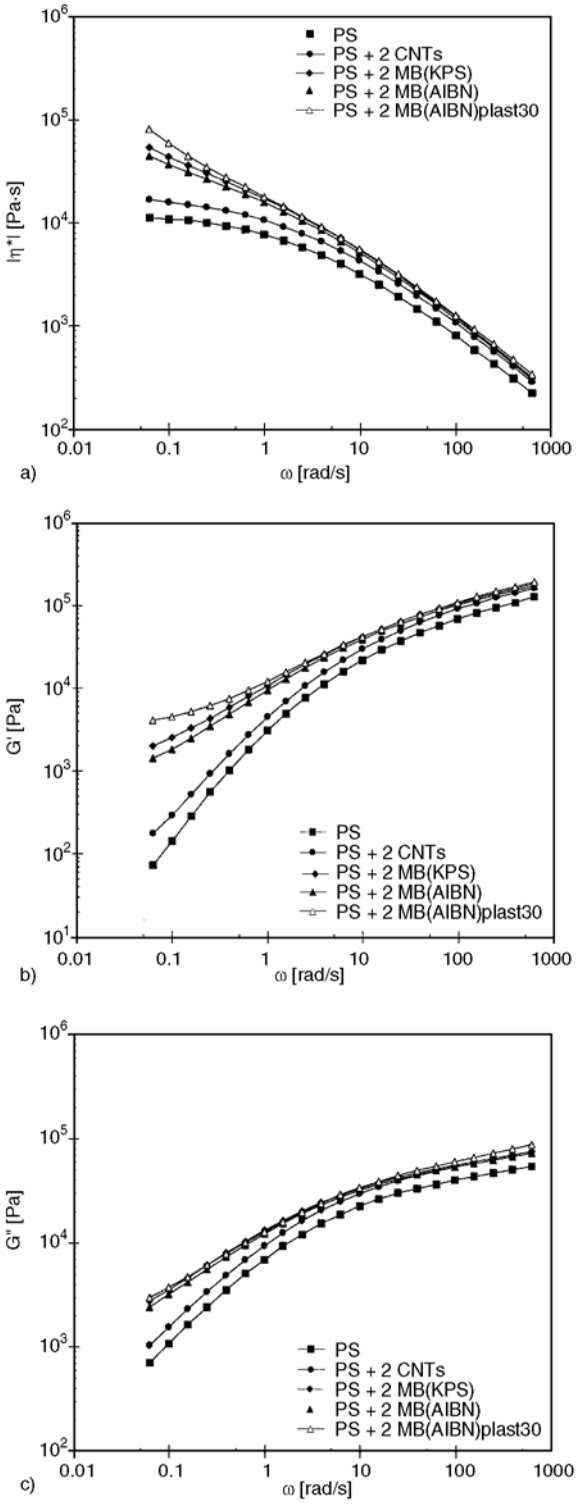

Figure 1. Complex viscosity (a), storage modulus (b), and loss modulus (c) of the final PS composites

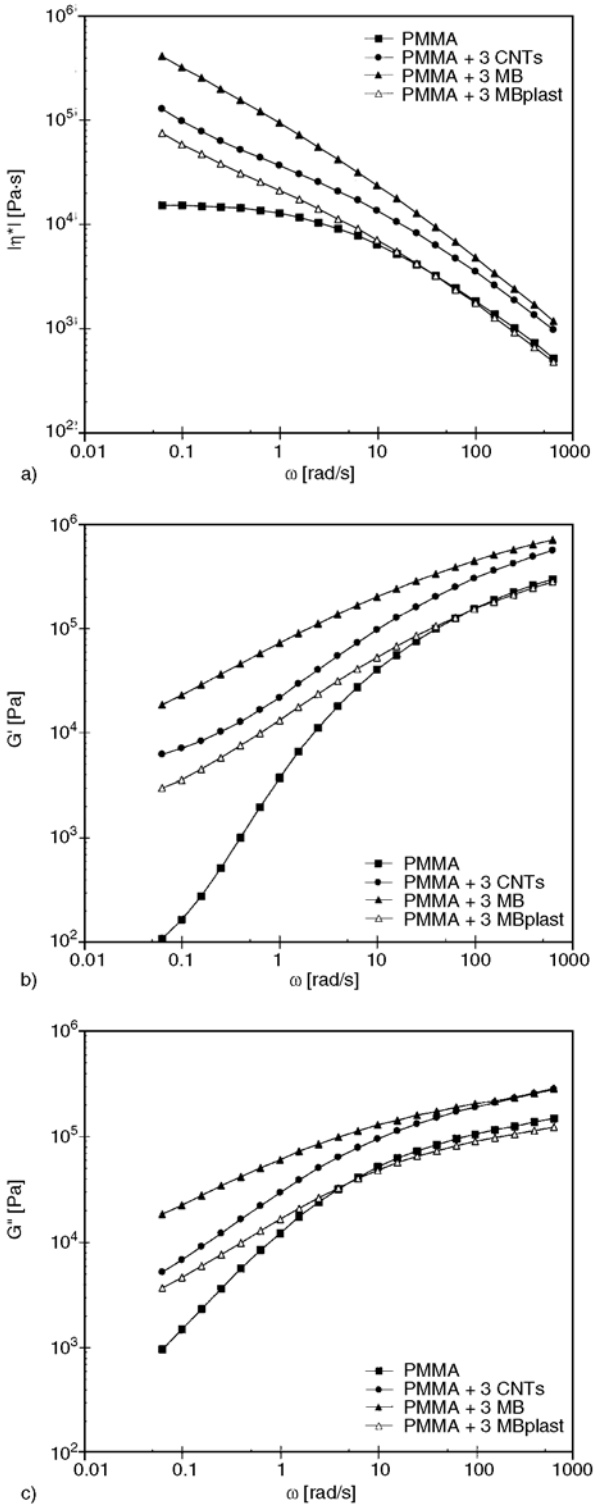

Figure 2. Complex viscosity (a), storage modulus (b), and loss modulus (c) of the final PMMA composites

terbatch. The difference was more pronounced at low frequency, where the viscosity of high molecular weight PS-masterbatch was higher than that of the lower molecular weight PS-masterbatch with the same amount of CNTs in the final composites.

The high molecular weight PS-masterbatch had the higher melt viscosity compared to the viscosity of the PS matrix. Based on the Equation 1, the masterbatch formed a discontinuous phase, because of the insufficient viscosity ratio of the components. In

order to improve the viscosity ratio of the components, the molecular weight of the PS-masterbatch was decreased by changing the *in situ* polymerization method. When the molecular weight of the PS-masterbatch was decreased and with higher polydispersity, the viscosity of the masterbatch slightly decreased. However, the resistivity of the final PS composite with the low molecular weight masterbatch was not decreased compared to the final PS composite with high molecular weight masterbatch (Table 1).

In the final PS composite with the low molecular weight masterbatch, the CNTs remained primarily in the PS-masterbatch phase due to the presence of AIBN initiator. The initiator can form additional bonding with CNTs [27], and some polymer pearls were tightly attached to CNTs preventing them from diffusing to the matrix polymer from the masterbatch (Figure 3). Therefore, the lower molecular weight decreased the viscosity of the masterbatch, but was offset by the presence of CNTs.

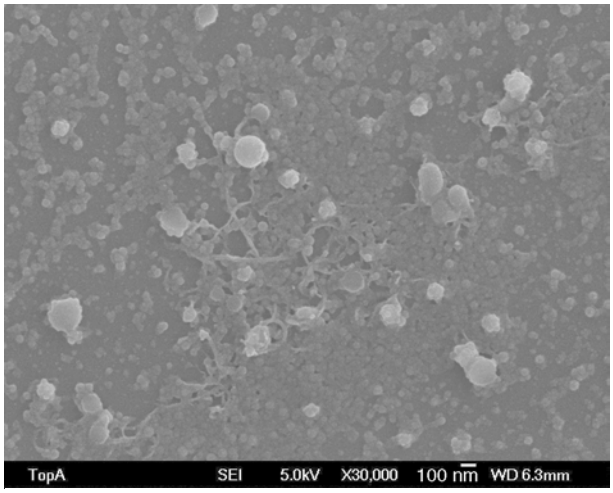

Figure 3. SEM micrograph of dried PS-masterbatch emulsion, AIBN as an initiator in the polymerization

An optimum viscosity ratio of the components was achieved when glycerol was added to the low molecular weight PS-masterbatch, with a corresponding decrease in resistivity of the final composite. The viscosity and dynamic moduli of the final composite increased when glycerol was added to the low molecular weight PS-masterbatch (Figure 1). With the addition of glycerol, the plasticized PS-masterbatch formed finer phase morphology in the final composite and the CNTs were able to diffuse into the PS matrix, which slightly increased the viscosity of the final composite. The T_g values of the pure composite components correlated, to some extent, with the viscosities of the composites (Table 2). The PS matrix had the lowest T_g, but the high molecular weight PS-masterbatch had a similar value. The low molecular weight PS-masterbatch showed the highest T_g. Due to the initiator used in the *in situ* polymerization of the low molecular weight PS-masterbatch, there were polymer chains grafted to the CNTs, which increased the T_g of the PS-masterbatch.

The matrix polymers were processed similarly as composites, in order to diminish the processing effects on the mechanical properties of CNT composites. The processing itself deteriorated the mechanical properties, which can be seen by comparing the values of pure matrix polymers given by the manufacturers and the values of processed matrix polymers (Tables 1 and 3). Tensile strength and strain at break for PS are 43.0 MPa and 2.0%, and for PMMA 73.0 MPa and 11.0%, respectively, given by manufacturers.

Table 3. The electrical resistivity and mechanical properties of PMMA samples

Sample	CNT content [wt%]	Electrical resistivity [Ω·cm]	Young's modulus [MPa]	Tensile strength [MPa]	Strain [%]
PMMA	–	$> 10^{15}$ a)	1220±39	58±3	6.2±0.5
1 CNTs/PMMA	1	$>10^9$	–	–	–
1 MB_{PMMA}/PMMA	1	$>10^9$	–	–	–
2 CNTs/PMMA	2	$>10^9$	1260±50	41±6	3.6±0.6
2 MB_{PMMA}/PMMA	2	$>10^9$	1240±33	25±4	2.4±0.4
2 MB_{PMMA} plast30/PMMA	2	$1.1 \cdot 10^8$	–	–	–
2 MB_{PMMA} plast50/PMMA	2	$4.1 \cdot 10^7$	–	–	–
3 CNTs/PMMA	3	$>10^9$	1280±35	32±10	3.5±0.8
3 MB_{PMMA}/PMMA	3	$>10^9$	1270±10	20±4	2.1±0.05
3 MBPMMA plast30/PMMA	3	320	989±69	26±8	3.2±1.3
4 CNTs/PMMA	4	$>10^9$	–	–	–
4 MB_{PMMA}/PMMA	4	$1.3 \cdot 10^5$	–	–	–

a)The resistivity of pure PMMA is a literature value, from [26]

Compounding CNTs directly with the matrix polymer appeared to slightly weaken the mechanical properties. In the case of PS, tensile modulus was affected more by the high molecular weight PS-masterbatch than by CNTs (Table 1). Tensile modulus was slightly higher when the high molecular weight PS-masterbatch was used. The direct addition of CNTs into the PS matrix did not affect tensile modulus, nor did the use of the low molecular weight PS-masterbatch. The improvement of mechanical properties depending on the molecular weight of the PS-masterbatch was seen more clearly in tensile strength. Tensile strength decreased when CNTs were added directly to PS matrix, which implies that CNTs were agglomerated and not dispersed as individual tubes. It has been observed that the addition of 0.15 wt% purified CNTs into a polystyrene slightly decreased tensile strength [22]. When the amount of CNTs increased to 4 wt%, they began to strengthen the composite, as a micro-size filler. The addition of plasticizer to the low molecular weight PS-masterbatch decreased the mechanical properties of the final PS composite (Table 1).

The SEM micrographs confirmed that the CNTs and the masterbatches formed separate phases in the final composites (Figures 4–5). The obtained resistivities of PS composites were ca. 10^5 Ω·cm. Though π-stacking between CNTs and PS limits the reagglomeration of CNTs, the CNTs formed agglomerates and behaved as macroscopic particles rather than individual nanoparticles in the directly melt mixed CNT composites. The diameter of CNT agglomerates was ca. 1 μm in the PS matrix, and the effect of the agglomerates can be seen in the mechan-

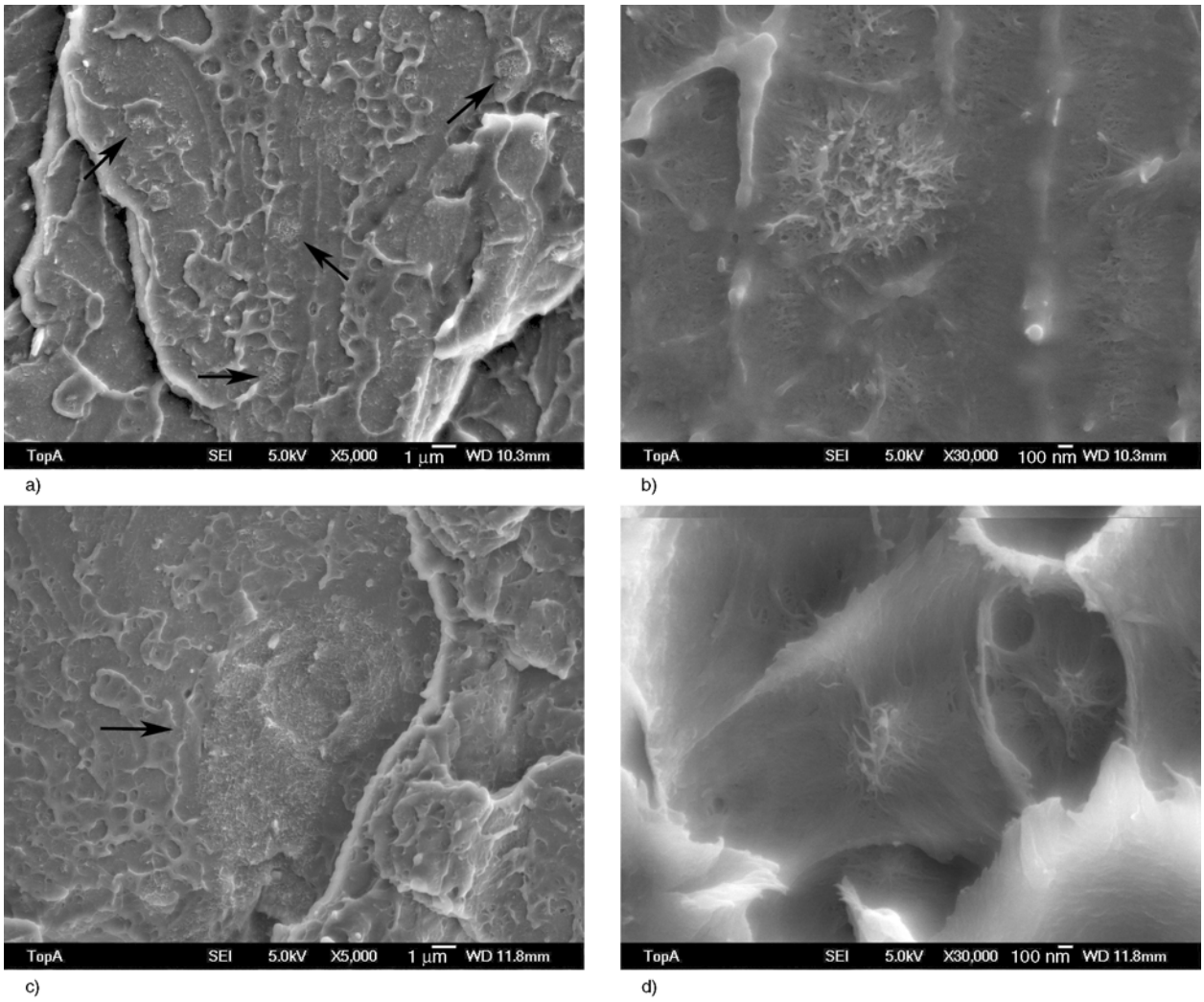

Figure 4. SEM micrographs of fracture surfaces of PS extrudates, a) 2 wt% CNTs in the final composite, prepared directly melt-mixed CNTs (2 CNTs/PS), b) higher magnification of 2 CNTs/PS composite c) 2 wt% CNTs in the final composite, prepared using masterbatch (2 $MB_{PS,AIBN}$/PS), and d) higher magnification of 2 $MB_{PS,AIBN}$/PS composite

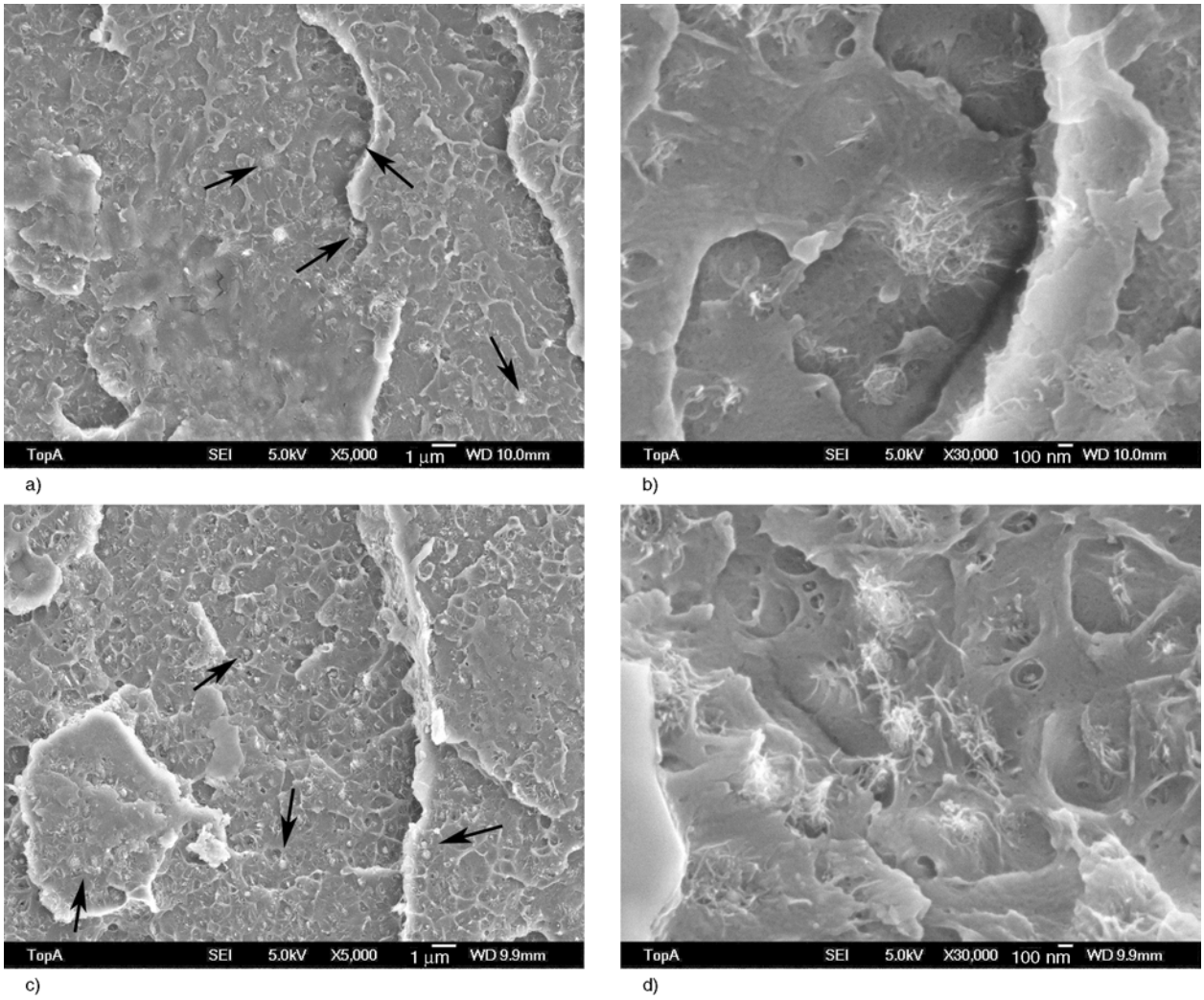

Figure 5. SEM micrographs of fracture surfaces of PMMA extrudates, a) 3 wt% CNTs in the final composite, prepared directly melt-mixed CNTs (3 CNTs/PMMA), b) higher magnification of 3 CNTs/PMMA composite c) 3 wt% CNTs in the final composite, prepared using masterbatch (3 MB_{PMMA}/PMMA), and d) higher magnification of 3 MB_{PMMA}/PMMA composite

ical properties, which were not improved as much as expected based on the amount of CNTs. On the other hand, CNTs were partly dispersed as individual tubes that formed an agglomerated network which improved the conductivity of the composite. In the final PS composites with PS-masterbatches, CNTs were mainly in the masterbatch phase and they were covered with *in situ* polymerized styrene (Figure 4c–d). In the previous study of *in situ* polymerization of PS-CNT composites, the obtained resistances were under 100 Ω [24]. Even though the resistivity and resistance values are not exactly proportional, the difference between the conductivities of the final PS composites and *in situ* polymerized PS-CNT composites indicates, in accordance with SEM image (Figure 4c), that the PS-masterbatch was dispersed in the matrix. Therefore, the resistivities of the final composites with PS-masterbatches were relatively high.

In the case of PMMA, without significant interfacial adhesion between the matrix polymer and the CNTs, there are only shear forces in the midiextruder to break up the CNT agglomerates. In addition, there are no additional forces to break up the CNT agglomerates and inhibit the reagglomeration of CNTs. The resistivity values of PS composites were clear indicators to select the efficient mixing parameters for PMMA. When the same mixing parameters were used, directly melt mixed PMMA-CNT composites were not conductive even with CNT loading of 4 wt% (Table 3).

To form a conductive network of CNTs in the PMMA matrix, the PMMA-masterbatch was tested. The low molecular weight masterbatch was chosen based

on the results of PS-masterbatches. The use of the PMMA-masterbatch gave clearly lower resistivity values than the use of the directly melt mixed CNTs (Table 3). A conductive composite was achieved below 4 wt% CNTs when the PMMA-masterbatch was used. When the viscosity of the PMMA-masterbatch was decreased with glycerol, the conductive composite was achieved below 3 wt% CNTs. Moderately low resistivity was achieved even with 2 wt% CNTs when a higher amount of glycerol was added to the PMMA-masterbatch.

As the viscosity of the components had an effect on the properties of the PS composites, the PMMA composites was analyzed by rheometry. The rheological behavior of PMMA composites was more straightforward than the case of PS composites (Figure 2). The addition of CNTs increased the viscosity of the PMMA matrix, and viscosity was highest when the PMMA-masterbatch was used. The PMMA-masterbatch had a higher molecular weight than the PMMA matrix and most of the CNTs were located in the PMMA-masterbatch phase, and both these factors led to an increase in viscosity.

When glycerol was added to the PMMA-masterbatch, the viscosity of the final PMMA composite was lower than the directly melt mixed CNT composite with a constant amount of CNTs. The glass transition temperatures, which were measured directly from the masterbatches as well as the matrix polymers, follow the trends in molecular weight and plasticization (Table 2). The PMMA matrix had the lowest T_g and the PMMA-masterbatch with higher molecular weight and CNTs had the highest T_g. When the PMMA-masterbatch was plasticized, the T_g shifted to a lower temperature. T_g of the plasticized PS-masterbatch was almost identical to the unplasticized PS-masterbatch. In the case of PMMA, without additional covalent bonds formed by initiators or other interfacial interactions between PMMA and CNTs, the plasticization of the PMMA-masterbatch was more effective than plasticization of the PS-masterbatch. Because of the improved plasticization of PMMA-masterbatch, the viscosity ratio of the components in PMMA composites was optimized, and PMMA-masterbatch formed continuous phase.

Due to the effective plasticization of the PMMA-masterbatch, tensile modulus was mainly affected by the plasticizer and not by the CNTs (Table 3). Without interactions between PMMA and CNTs, tensile modulus remained at similar values regardless of how CNTs were introduced into the PMMA matrix. On the other hand, tensile strength of the PMMA composites decreased after the addition of CNTs, which was more pronounced with the use of the PMMA-masterbatch than with directly melt mixed CNTs. However, tensile strength of the PMMA composite was improved upon addition of plasticizer to the PMMA-masterbatch. The same behavior can be seen for tensile strain at break. This may be taken as indirect evidence that CNTs were well-dispersed in the plasticized PMMA composite. Based on the SEM images, CNTs agglomerates were larger in the PS composites compared to the PMMA composites (Figures 4–5). The diameter of CNT agglomerates was ca. 0.5 μm in the PMMA matrix (Figure 5), which was half of the diameter of the CNT agglomerates in the PS matrix. Though the CNTs formed smaller agglomerates in the PMMA matrix, the resistivity of the PMMA composites was high. CNTs were mostly present in the form of agglomerates without individualized CNTs forming a network which would increase conductivity into the composites. Contrary to the PS composites, the PMMA-masterbatch formed a continuous phase in the final PMMA composite. In the previous study of *in situ* polymerization of CNT/PMMA composite, the obtained resistances were ca. 100 Ω [24], which are similar to the resistivities of PMMA-masterbatch composites, 100 Ω·cm. This indicates that there was the continuous phase of PMMA-masterbatch in the final PMMA composite. Finer phase morphology of PMMA-masterbatch in the PMMA matrix can be seen in the SEM image (Figure 5c) compared to the PS-masterbatch in the PS composite (Figure 4c). The CNTs were not coated by polymerized methyl methacrylate in the PMMA-masterbatch, and CNTs can diffuse more easily during melt mixing. Therefore, the use of PMMA-masterbatch improved the conductivity of the final composites of PMMA.

4. Conclusions

The properties of composite materials are determined by many different variables. It is not the sum of the mechanical and electrical properties of the components that determines properties of the final composite. The rheological properties of the materi-

als and the internal and external forces, such as interfacial interactions between the components and mechanical mixing forces, have great impact on the properties of the composite. Two different CNT composites were studied: PS composites with interactions between the components and PMMA composites without interactions between the components.

The results confirm that, for lowering the percolation threshold of CNTs, novel compounding methods are needed, as there are limited possibilities for adjusting the shear forces during melt mixing. The mechanical properties of the composites were mostly determined by the amount of CNTs. In contrast, the resistivity of the composites was more dependent on how CNTs were added into the matrix polymer. In the case of PS composites with stronger interfacial interactions between the components, CNTs can be directly melt mixed into the PS matrix and obtain a conductive composite. The strong interaction between CNTs and PS enhanced the dispersion of the CNTs. But without significant adhesion between the components, the use of a masterbatch improved the conductivity of PMMA composites. In the case of PMMA, there are no strong interactions between CNTs and the matrix during melt mixing, and there was only small amount of individually dispersed CNTs in the PMMA matrix. Due to the ease of emulsion polymerization of the masterbatch, the properties of the masterbatch could be tailored based on the molecular weight and viscosity, thereby tailoring the properties of the final composite. When CNTs were well-dispersed in a PMMA-masterbatch, which had optimized viscosity compared to the PMMA matrix, the use of a PMMA-masterbatch notably decreased the percolation threshold of the CNT-PMMA composite.

Acknowledgements

The Finnish Funding Agency for Technology and Innovation (Tekes, project 2330/31/06) and POPROK Graduate School are thanked for financial support. Mr. Antti Metsälä is warmly thanked.

References

[1] Gorga R. E., Cohen R. E.: Toughness enhancements in poly(methyl methacrylate) by addition of oriented multiwall carbon nanotubes. Journal of Polymer Science Part B: Polymer Physics, **42**, 2690–2702 (2004). DOI: 10.1002/polb.20126

[2] Feldman A. Y., Larin B., Berestetsky N., Marom G., Weinberg A.: Microbeam WAXD study of orientated crystalline arrays in carbon fiber/CNT – nylon 66 extruded/drawn composites. Journal of Macromolecular Science Part B: Physics, **46**, 111–117 (2007). DOI: 10.1080/00222340601044243

[3] Salalha W., Dror Y., Khalfin R. L., Cohen Y., Yarin A. L., Zussman E.: Single-walled carbon nanotubes embedded in oriented polymeric nanofibers by electrospinning. Langmuir, **20**, 9852–9855 (2004). DOI: 10.1021/la048536b

[4] Du F., Fischer J. E., Winey K. I.: Coagulation method for preparing single-walled carbon nanotube/poly (methyl methacrylate) composites and their modulus, electrical conductivity, and thermal stability. Journal of Polymer Science Part B: Polymer Physics, **41**, 3333–3338 (2003). DOI: 10.1002/polb.10701

[5] Kharchenko S. B., Douglas J. F., Obrzut J., Grulke E. A., Migler K. B.: Flow-induced properties of nanotube-filled polymer materials. Nature Materials, **3**, 564–568 (2004). DOI: 10.1038/nmat1183

[6] Mičušík M., Omastová M., Krupa I., Prokeš J., Pissis P., Logakis E., Pandis C., Pötschke P., Pionteck J.: A comparative study on the electrical and mechanical behaviour of multi-walled carbon nanotube composites prepared by diluting a masterbatch with various types of polypropylenes. Journal of Applied Polymer Science, **113**, 2536–2551 (2009). DOI: 10.1002/app.30418

[7] Moniruzzaman M., Winey K. I.: Polymer nanocomposites containing carbon nanotubes. Macromolecules, **39**, 5194–5205 (2006). DOI: 10.1021/ma060733p

[8] Jin S. H., Kang C. H., Yoon K. H., Bang D. S., Park Y-B.: Effect of compatibilizer on morphology, thermal, and rheological properties of polypropylene/functionalized multi-walled carbon nanotubes composite. Journal of Applied Polymer Science, **111**, 1028–1033 (2009). DOI: 10.1002/app.29009

[9] Lin B., Sundararaj U., Pötschke P.: Melt mixing of polycarbonate with multi-walled carbon nanotubes in miniature mixers. Macromolecular Materials and Engineering, **291**, 227–238 (2006). DOI: 10.1002/mame.200500335

[10] Isayev A. I., Kumar R., Lewis T. M.: Ultrasound assisted twin screw extrusion of polymer–nanocomposites containing carbon nanotubes. Polymer, **50**, 250–260 (2009). DOI: 10.1016/j.polymer.2008.10.052

[11] Coleman J. N., Cadek M., Ryan K. P., Fonseca A., Nagy J. B., Blau W. J., Ferreira M. S.: Reinforcement of polymers with carbon nanotubes. The role of an ordered polymer interfacial region. Experiment and modeling. Polymer, **47**, 8556–8561 (2006). DOI: 10.1016/j.polymer.2006.10.014

[12] Wiemann K., Kaminsky W., Gojny F. H., Schulte K.: Synthesis and properties of syndiotactic poly(propylene)/carbon nanofiber and nanotube composites prepared by *in situ* polymerization with metallocene/ MAO catalysts. Macromolecular Chemistry and Physics, **206**, 1472–1478 (2005).
DOI: 10.1002/macp.200500066

[13] Zhou Z., Wang S., Zhang Y., Zhang Y.: Effect of different carbon fillers on the properties of PP composites: Comparison of carbon black with multiwalled carbon nanotubes. Journal of Applied Polymer Science, **102**, 4823–4830 (2006).
DOI: 10.1002/app.24722

[14] Logakis E., Pandis C., Peoglos V., Pissis P., Stergiou C., Pionteck J., Pötschke P., Mičušík M., Omastová M.: Structure–property relationships in polyamide 6/ multi-walled carbon nanotubes nanocomposites. Journal of Polymer Science Part B: Polymer Physics, **47**, 764–774 (2009).
DOI: 10.1002/polb.21681

[15] Zhao C., Hu G., Justice R., Schaefer D. W., Zhang S., Yang M., Han C. C.: Synthesis and characterization of multi-walled carbon nanotubes reinforced polyamide 6 via *in situ* polymerization. Polymer, **46**, 5125–5132 (2005).
DOI: 10.1016/j.polymer.2005.04.065

[16] Jordhamo G. M., Manson J. A., Sperling L. H.: Phase continuity and inversion in polymer blends and simultaneous interpenetrating networks. Polymer Engineering and Science, **26**, 517–524 (1986).
DOI: 10.1002/pen.760260802

[17] Ports B. F., Weiss R. A.: One-step melt extrusion process for preparing polyolefin/clay nanocomposites using natural montmorillonite. Industrial and Engineering Chemistry Research, **49**, 11896–11905 (2010).
DOI: 10.1021/ie902050r

[18] Meincke O., Kaempfer D., Weickmann H., Friedrich C., Vathauer M., Warth H.: Mechanical properties and electrical conductivity of carbon-nanotube filled polyamide-6 and its blends with acrylonitrile/butadiene/ styrene. Polymer, **45**, 739–748 (2004).
DOI: 10.1016/j.polymer.2003.12.013

[19] Pötschke P., Bhattacharyya A. R., Janke A.: Morphology and electrical resistivity of melt mixed blends of polyethylene and carbon nanotube filled polycarbonate. Polymer, **44**, 8061–8069 (2003).
DOI: 10.1016/j.polymer.2003.10.003

[20] Grossiord N., Kivit P. J. J., Loos J., Meuldijk J., Kyrylyuk A. V., van der Schoot P., Koning C. E.: On the influence of the processing conditions on the performance of electrically conductive carbon nanotube/polymer nanocomposites. Polymer, **49**, 2866–2872 (2008).
DOI: 10.1016/j.polymer.2008.04.033

[21] Pötschke P., Pegel S., Claes M., Bonduel D.: A novel strategy to incorporate carbon nanotubes into thermoplastic matrices. Macromolecular Rapid Communications, **29**, 244–251 (2008).
DOI: 10.1002/marc.200700637

[22] Yuan J-M., Fan Z-F., Chen X-H., Chen X-H., Wu Z-J., He L-P.: Preparation of polystyrene–multiwalled carbon nanotube composites with individual-dispersed nanotubes and strong interfacial adhesion. Polymer, **50**, 3285–3291 (2009).
DOI: 10.1016/j.polymer.2009.04.065

[23] Tong X., Liu C., Cheng H-M., Zhao H., Yang F., Zhang X.: Surface modification of single-walled carbon nanotubes with polyethylene via *in situ* Ziegler–Natta polymerization. Journal of Applied Polymer Science, **92**, 3697–3700 (2004).
DOI: 10.1002/app.20306

[24] Lahelin M., Annala M., Nykänen A., Ruokolainen J., Seppälä J.: *In situ* polymerized nanocomposites: Polystyrene/CNT and poly(methyl methacrylate)/CNT composites. Composites Science and Technology, **71**, 900–907 (2011).
DOI: 10.1016/j.compscitech.2011.02.005

[25] Schrader D.: Physical constants of poly(styrene). in 'Polymer handbook' (eds.: Brandrup J., Immergut E. H., Grulke E. A., Abe A., Bloch D. R.) Wiley, New York, V/91–V/96 (1999).

[26] Wunderlich W.: Physical constants of poly(methyl methacrylate). in 'Polymer handbook' (eds.: Brandrup J., Immergut E. H., Grulke E. A., Abe A., Bloch D. R.) Wiley, New York, V/87–V/90 (1999).

[27] Jia Z., Wang Z., Xu C., Liang J., Wei B., Wu D., Zhu S.: Study on poly(methyl methacrylate)/carbon nanotube composites. Materials Science and Engineering A, **271**, 395–400 (1999).
DOI: 10.1016/S0921-5093(99)00263-4

eXPRESS Polymer Letters Vol.6, No.10 (2012) 826–836
Available online at www.expresspolymlett.com
DOI: 10.3144/expresspolymlett.2012.88

Microencapsulation of butyl stearate with melamine-formaldehyde resin: Effect of decreasing the pH value on the composition and thermal stability of microcapsules

*B. Alič, U. Šebenik, M. Krajnc**

University of Ljubljana, Faculty of Chemistry and Chemical Technology, Aškerčeva cesta 5, SI-1001 Ljubljana, Slovenia

Received 2 March 2012; accepted in revised form 12 May 2012

Abstract. The object of this study was to investigate how different decreasing of pH regimes during microencapsulation process with melamine-formaldehyde (MF) resin affects the composition, morphology and thermal stability of microcapsules containing a phase-change material (PCM). Technical butyl stearate was used as PCM. Microencapsulation was carried out at 70°C. For all experiments the starting pH value was 6.0. After one hour of microencapsulation at the starting pH value, the pH value was lowered to final pH value (5.5; 5.0; 4.5) in a stepwise or linear way. The properties of microcapsules were monitored during and after the microencapsulation process. The results showed that pH value decreasing regime was critical for the morphology and stability of microcapsules. During microencapsulations with a stepwise decrease of pH value we observed faster increase of the amount of MF resin in the microencapsulation product compared to the microencapsulations with a linear pH value decrease. However, faster deposition in the case of microencapsulations with stepwise decrease of pH value did not result in thicker MF shells. The shell thickness increased much faster when the pH value was decreased in a linear way or in several smaller steps. It was shown that for the best thermal stability of microcapsules, the pH value during microencapsulation had to be lowered in a linear way or in smaller steps to 5.0 or lower.

Keywords: *thermal properties, microencapsulation, melamine-formaldehyde resin, phase-change materials*

1. Introduction

Microcapsules are tiny particles with diameters in the range between 1 and 1000 μm that consist of a core material and a covering shell. Through a selection of the core and shell material, it is possible to obtain microcapsules with a variety of functions. This is why microcapsules can be defined as containers, which can release, protect and/or mask various kinds of active core materials [1]. Microencapsulation is mainly used for the separation of core material from the environment, but it can also be used for controlled release of core material in the environment. Microencapsulation has specially attracted a large interest in the field of phase change materials (PCMs) as they are capable of storing and releasing energy during solid-liquid phase transition. The applications of PCMs in thermal energy storage have been well known and used in many fields [2–11]. For shell material of PCM microcapsules melamine-formaldehyde resin is often used mainly because of its good mechanical [12–14] and thermal stability [9, 14–16]. Melamine-formaldehyde (MF) microcapsules can be prepared by the *in situ* polymerization process by polycondensation, where the melamine-formaldehyde prepolymer is initially soluble in the continuous water phase, while the hydrophobic core material is contained in dispersed droplets. As the polymerization reaction starts in aqueous solution, the formed oligomers start to collapse on the surface of the core droplets.

*Corresponding author, e-mail: matjaz.krajnc@fkkt.uni-lj.si

On the surface, the polymerization continues and crosslinking occurs, which results in a solid MF shell formation [17–21]. The shell formation is particularly linked to the pH value [15, 17, 18, 20], temperature [15, 20, 22], type and the amount of emulsifier used [18, 22–27] and to melamine to formaldehyde molar ratio [20], which all significantly determine thermal stability and shell morphology of microcapsules. For a successful formation of a homogenous and compact MF shell the usage of anionic emulsifiers is necessary. In the case of cationic emulsifiers, charge repulsion between cationic emulsifier and MF resin negatively influences the shell formation in microcapsules. On the other hand, the efficiency of nonionic emulsifiers is medium [26]. Faster MF shell formation is achieved at lower pH values. However, the usage of low pH values results in microcapsules with raspberry-like surface or even in lower microencapsulation efficiency, while at relatively high pH values a smooth MF shell is formed [20].

In our previous work, the research was focused on the investigation of MF microcapsules with decane core, which were prepared at different temperatures and different pH values [28]. The degree of curing of the MF resin at different process parameters was studied as well. It was found that at higher temperatures and lower pH values the time necessary for stable microcapsules formation is shorter. Thicker shells were obtained in microencapsulations carried out at lower pH values and higher temperatures. At lower pH values the degree of MF resin crosslinking was higher.

In the present work, microencapsulation of butyl stearate with melamine-formaldehyde resin was carried out at 70°C at different pH value decreasing regimes. As PCM butyl stearate was chosen because its phase change temperature is around 20ºC, where melting and crystallization occur, and because it has a relatively high heat storage capacity. Therefore, it can be used as an effective thermo regulating material at ambient temperature. For example, microencapsulated butyl stearate can be used as an additive in indoor or outdoor coatings or it may be built in insulating materials, such as foams. The main objective of this study was to investigate the effects of decreasing the pH value regime and final pH value on the composition of microcapsules, their thermal stability and morphology. To study the microencapsulation process, properties of microcapsules were investigated during and after the microencapsulation. For this purpose differential scanning calorimetry, scanning electron microscopy and thermogravimetric analysis were used.

2. Experimental

2.1. Materials

We used etherified melamine-formaldehyde (MF) resin (70 wt%, Melapret NF70/M, Melamin, Kočevje, Slovenia), butyl stearate (technical, 40–60%, rest butyl palmitate, Sigma-Aldrich, Steinheim, Germany), sodium dodecyl sulfate (SDS, 98.5%, Sigma-Aldrich, Steinheim, Germany), formic acid (99.8%, Kemika, Zagreb, Croatia) and deionized water.

2.2. Preparation of microcapsules

Emulsion preparation: 25 g of technical butyl stearate, 2.5 g of SDS (used as emulsifier), 15 g of MF resin and 457.5 g of deionized water were mixed for 30 minutes using Ultraturax Dispermat (VMA-Getzmann, Reichshof, Germany) at the rate of 1000 rpm and temperature of 30°C.

Microencapsulation: The emulsion was poured into a glass five neck reactor, equipped with a reflux condenser, a mechanical stirrer, a digital thermometer, a high pressure liquid chromatography (HPLC) pump K-120 (Knauer, Berlin, Germany) and a glass electrode for pH measurements. The reactor content was stirred at the rate of 500 rpm. The pH value of emulsion was adjusted to 6.0 by adding 1 wt% formic acid solution at the rate of 1 mL/min using HPLC pump and then heated to 70°C. During microencapsulation processes the temperature was kept constant at 70°C, while the pH value was regulated according to the regimes shown in Figure 1. Every 30 minutes samples were taken from the reactor to analyze the composition and properties of microcapsules. Before analyses the samples were filtered through paper filter discs (Sartorius 388) and washed with warm deionized water. The wet cake containing microcapsules was dried at room temperature to constant weight and dry powders of microcapsules were used for characterization. In the text of this report, the samples are labeled as MC(*x*–*y*/step/*t*) and MC(*x*–*y*/linear/*t*) for microencapsulation with stepwise or linear decrease regime of pH values, respectively. MC stands for microcapsules, *x*–*y* for

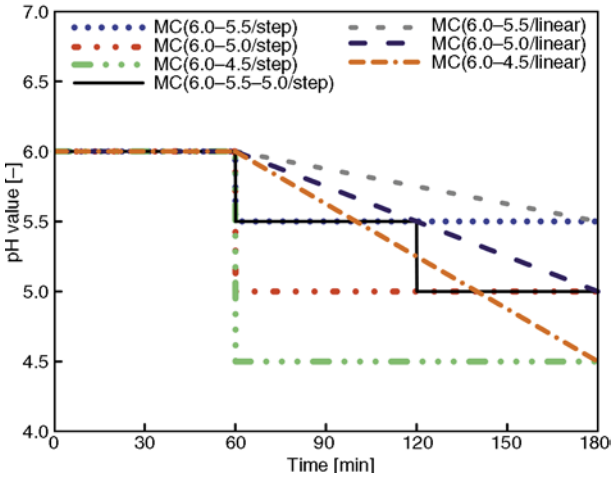

Figure 1. pH value regimes during microencapsulation processes

starting and final pH value of microencapsulation and *t* for sampling time.

2.3. Characterization of microcapsules

The morphology of microcapsules was observed by scanning electron microscopy using a FE-SEM ULTRA Plus (Carl Zeiss, Oberkochen, Germany) instrument. Before SEM analysis the samples were partly mechanically cut with a razor blade. The cutting lasted for several minutes until the analyzed sample contained enough damaged microcapsules for their shell thickness determination. Treated samples (containing damaged and whole microcapsules) were sparsely sprinkled onto a carbon tape attached to metal stubs, dried in vacuum at 100°C for 48 hours and then gold coated at 20 mA for 1.5 min (SCD 030 gold coater, Balzers Union model FL-9496, Liechtenstein). The samples were then imaged using an accelerating voltage of 1 kV. For the purpose of determining shell thickness at least four SEM images of the same sample were taken. The shell thickness was measured using SmartSEM software. The average shell thickness value was calculated out of at least ten shell thickness values obtained for an individual sample.

Differential scanning calorimetry (DSC) was used to define mass percentage of shell material in microcapsules. The measurements were performed on a Mettler Toledo DSC1 instrument with intra-cooler using STAR software. In and Zn standards were used for the temperature calibration and for the determination of the instrument time constant. Standard 40 μL alumina pans and air atmosphere were used. Sample mass was about 10 mg. The following temperature program was used: An isothermal segment at 50°C for 5 minutes was followed by a cooling segment from 50 to –50°C with a cooling rate of –5°C/min. Then a heating segment from –50 to 50°C with a heating rate of 5°C/min was performed. This temperature interval was chosen because the phase change temperature of butyl stearate is around 20°C. Each sample was analyzed three times and the average weight percentage of core material was calculated from melting enthalpies of bulk and encapsulated core material. Termograms of butyl stearate and samples isolated at 180 minutes are presented in Figure 2. To confirm the core to shell weight ratio obtained by DSC analysis a gravimetric analysis was performed by Soxhlet extraction of core material in acetone for 72 hours. Duration of one extraction cycle was 4 minutes. After extraction, sample residues were dried at room temperature for

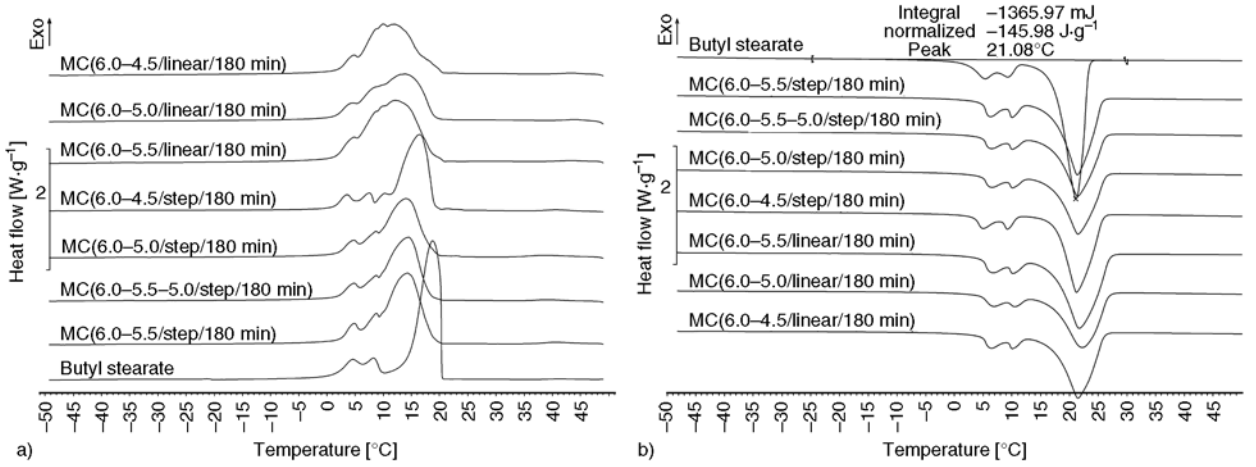

Figure 2. Thermograms for butyl stearate and microcapsules obtained at the end of microencapsulation: (a) butyl stearate crystallization peaks and (b) butyl stearate melting peaks

12 hours and additional 15 hours in vacuum at 50°C. The dried sample residues were weighed and the weight percentage of shell material in microcapsules was calculated. To confirm complete Soxhlet extraction of core material, DSC analysis of sample residue was also performed.

Thermogravimetric analysis (TGA) of microcapsules was performed using a Mettler Toledo TGA/DSC1 instrument with STAR software. All the experiments were conducted in a nitrogen atmosphere with a flow rate of 50 mL/min at a heating rate of 10°C/min from 50 to 500°C. Standard 80 µL Al_2O_3 crucibles were used. For all measurements the baseline was subtracted. Sample mass was about 10 mg.

3. Results and discussion

3.1. Microcapsule composition and morphology

Variations of weight percentage of MF resin in samples during microencapsulations carried out at different process parameters are presented in Figure 3.

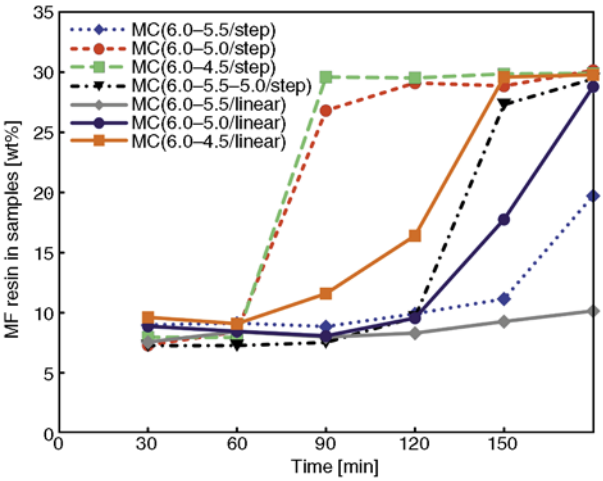

Figure 3. Weight percentage of MF resin in samples during microencapsulation processes determined by DSC analysis

Until 60 minutes of microencapsulation processes, which was carried out at pH value 6.0 for all experiments, the weight percentage of MF resin in samples was constant and within the range of 7–10%. Discrepancies between individual microencapsulation samples can be attributed to incomplete stability of microcapsule shells [28]. At the point when the pH value started decreasing, the weight percentage of MF resin in samples started to increase, depending on the regime by which pH value was decreased and on the final pH value. The increase of the amount of MF resin was faster in the case of stepwise pH value decrease, than in the case of linear pH value decrease. As expected, the fastest increase of the amount of MF resin was observed in microencapsulation MC(6.0–4.5/step), i.e. when we used a stepwise pH value decrease to the lowest pH value. This is explained by faster MF resin polymerization [29, 30], curing reactions [31] and consecutive deposition [20] of MF resin on microcapsules surface at lower pH values. In MC(6.0–4.5/step) synthesis the final weight percentage of MF resin was reached already at 90 minutes (30 minutes after lowering the pH value from 6.0 to 4.5). The lowest increase of MF resin amount was achieved in synthesis MC(6.0–5.5/linear), i.e. at linear pH value decrease to the highest final pH value. To verify the accuracy of DSC results a gravimetric analysis by Soxhlet extraction was performed. DSC and gravimetric measurements results for samples of microencapsulations are shown in Table 1. DSC results were in good agreement with gravimetrical results.

Shell morphology and thickness of microcapsules were evaluated using SEM images. Selected images of microcapsules, obtained at different process parameters and different process times, are shown in Figures 4 and 5.

Table 1. DSC and gravimetrical results for weight percentage of the MF resin in samples of microencapsulation

Microencapsulation	MF resin in samples [wt%]					
	DSC analysis			Gravimetric analysis		
	60 min	120 min	180 min	60 min	120 min	180 min
MC(6.0–5.5/step)	9.1	9.9	19.7	–	–	19.3
MC(6.0– 5.0/step)	8.4	29.1	30.1	–	–	29.6
MC(6.0– 4.5/step)	7.9	29.5	29.9	8.2	28.6	29.2
MC(6.0–5.5–5.0/step)	7.3	9.6	29.4	–	–	29.1
MC(6.0–5.5/linear)	8.4	8.3	10.1	–	–	10.3
MC(6.0–5.0/linear)	8.4	9.5	28.8	–	–	27.6
MC(6.0–4.5/linear)	9.1	16.4	29.8	10.4	17.1	29.6

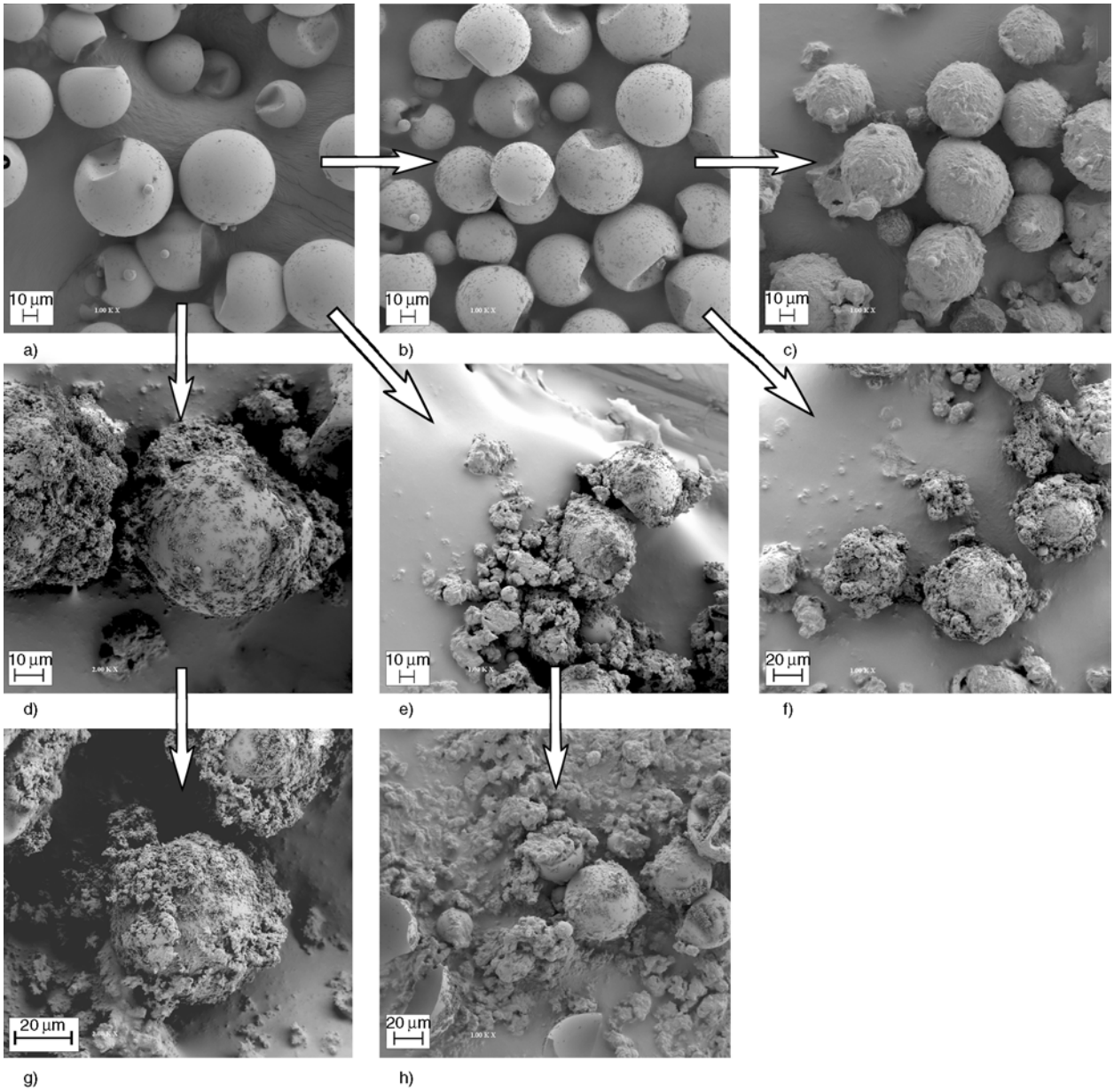

Figure 4. SEM image of microcapsules isolated during microencapsulations with stepwise decrease of the pH value: a→b→c for MC(6.0–5.5–5.0/step) at 60, 120 and 180 minutes; a→b→f for MC(6.0–5.5–5.0/step/180 min) at 60, 120 and 180 minutes; a→e→h for MC(6.0–5.0/step) at 60, 120 and 180 minutes and a→d→g for MC(6.0–4.5/step) at 60, 120 and 180 minutes

Since in all microencapsulations the process parameters were the same till 60 minutes, the microcapsules morphology was also the same. As can be seen from SEM images of microcapsules at 60 minutes (Figure 4a and Figure 5a), microcapsules have a smooth shell with only a few pure MF particles attached to them. After the pH value was decreased the pure MF particles started depositing faster on the surface. Deposition of MF particles was particularly rapid in the case of stepwise decrease of the pH value to 5.0 (Figures 4e and 4h) and 4.5 (Figures 4d and 4g). The MF particles were not deposited evenly all over the surfaces of microcapsules. Moreover, the MF particles were not firmly attached to the surface as several free clusters of MF particles were noticed.

Treatment (cutting, crushing) of microcapsules before actual SEM analysis allowed for the determination of the average shell thickness. An example of shell thickness determination for sample MC(6.0–4.5/linear/180 min) is given in Figure 6.

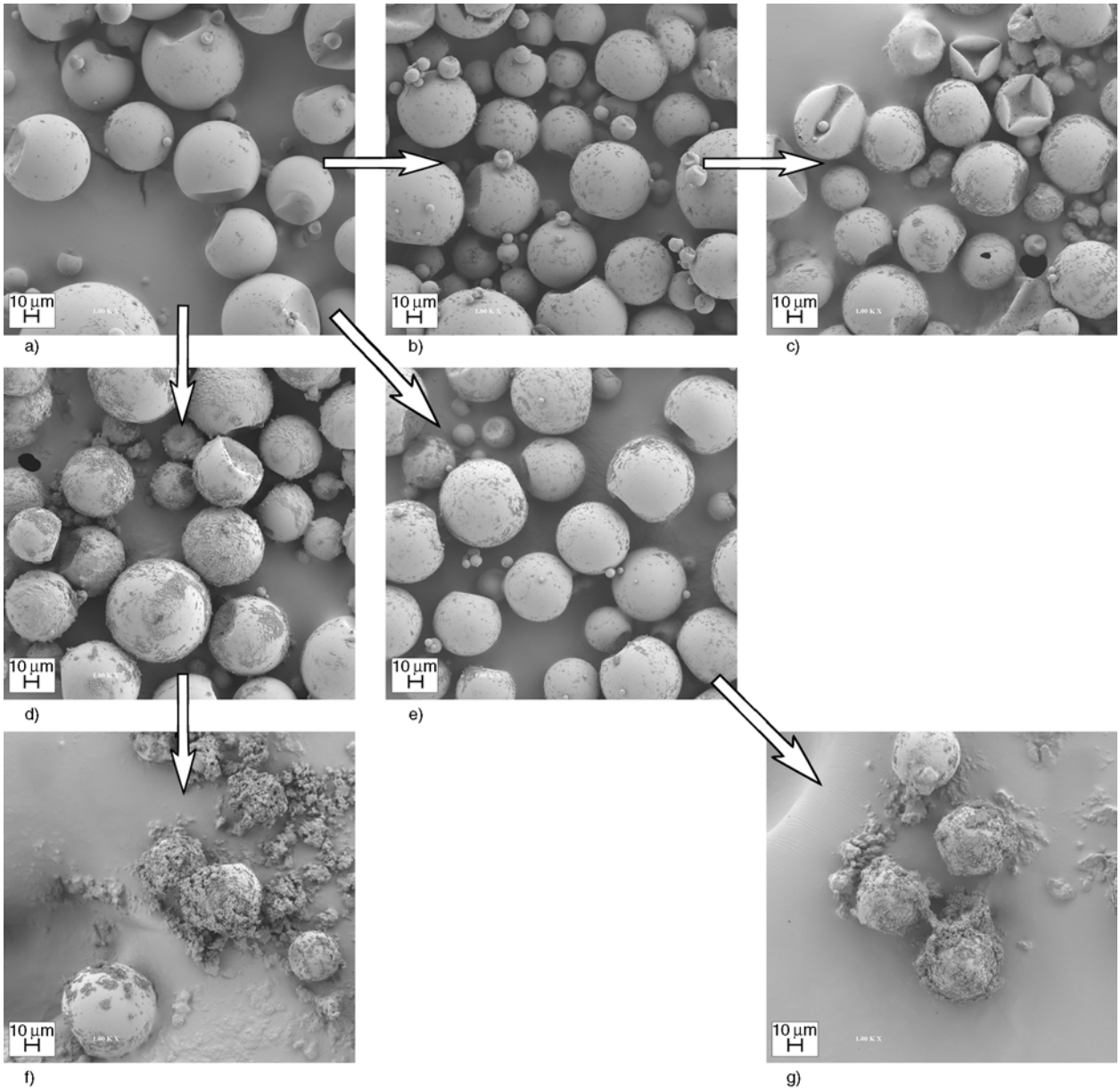

Figure 5. SEM image of microcapsules isolated during microencapsulations with linear decrease of the pH value: a→b→c for MC(6.0–5.5/linear) at 60, 120 and 180 minutes; a→e→g for MC(6.0–5.0/linear) at 60, 120 and 180 minutes; a→d→f for MC(6.0–4.5/linear) at 60, 120 and 180 minutes

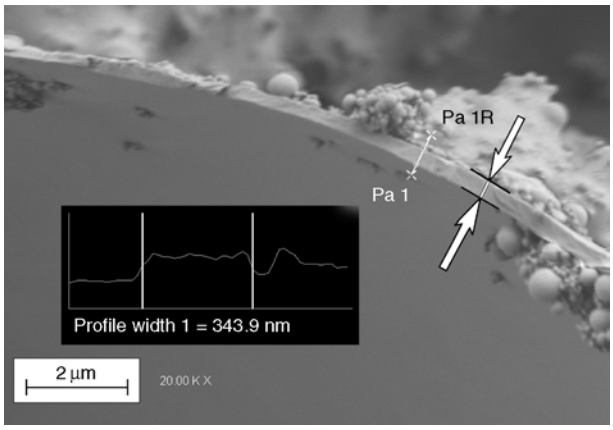

Figure 6. Shell thickness determination for microcapsules MC(6.0–4.5/linear/180 min)

In this figure we can clearly observe the small pure MF particles. For determining the shell thickness only the thickness of the smooth part of the shell without small particles on the surface was measured. Changes in the average shell thicknesses during microencapsulation processes are shown in Figure 7.

Shell thickness of microcapsules after one hour of microencapsulation was almost the same in all experiments because of identical process parameters used during the first 60 minutes. The average shell thickness at 60 minutes was between 290 and

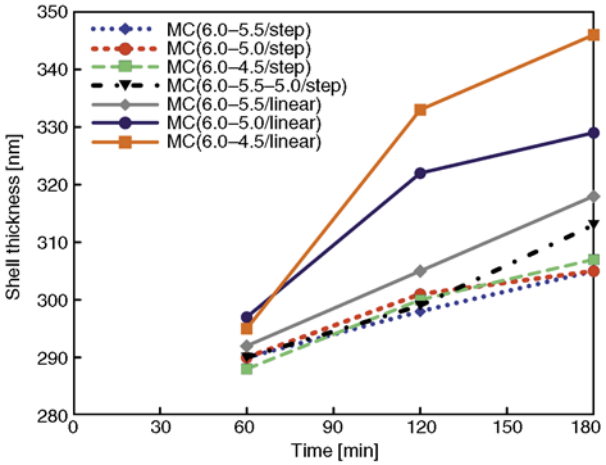

Figure 7. Average shell thickness during microencapsulation processes

300 nm. After that, in all syntheses the average shell thickness increased with microencapsulation time. The increase depended on the pH value and on the manner in which the pH value was lowered. In microencapsulations with stepwise pH value decrease the shell thickness increased slowly and there were no major differences in shell thickness between the experiments. Among these samples the thickest shell was observed in sample MC(6.0–5.5–5.0/step/180 min) for which the pH value decrease was performed in two steps. On the other hand, in microencapsulations with linear pH value decrease significant differences in shell thickness between samples with different final pH value were observed. Namely, the shell thickness increased with decreasing the final pH value. The shells of microcapsules, obtained by linear decrease the pH value, were therefore significantly thicker than those of microcapsules obtained by stepwise pH value decrease.

3.2. Thermal stability of microcapsules

TGA was used to investigate thermal stability of microcapsules and its pure components. Thermal characteristics of starting components (butyl stearate and dried MF prepolymer Melapret NF 70/M) and by Soxhlet extraction isolated MF resin of samples MC(6.0–5.0/linear/180 min) and MC(6.0–5.5–5.0/step/180 min) are shown in Figure 8. Butyl stearate evaporated/decomposed completely in one step from 160 to 300°C (Table 2). For dried uncured MF resin Melapret NF 70/M two distinctive steps of weight loss were observed. In two partially cured MF resins (microcapsules' shell material) the weight loss did not occur as distinctively on the account of differences in the chemical structure between partially cured and non-cured MF resin. Thermal stability of MF resins was studied in detail by Manley

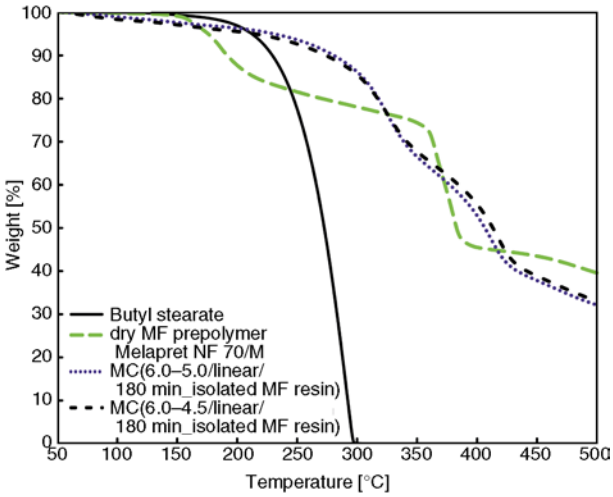

Figure 8. TGA curves of butyl stearate, dried MF prepolymer Melapret NF70/M and isolated MF resins of MC(6.0–5.0/linear/180 min) and MC(6.0–4.5/step/180 min)

Table 2. Results TGA analysis of core material, isolated MF resins and microcapsules at 180 minutes

Sample	Shell thickness [nm]	MF resin [wt%]	At 300°C			Residue at 500°C [wt%]
			Total weight loss [wt%]	Weight loss on account of core material [wt%]	Evaporated core material [wt%]	
butyl stearate	–	0	100	100	100	0
isolated MF resins	–	100	15*	0	0	32
MC(6.0–5.5/step/180 min)	307	19.7	20.5	17.5	22	5.2
MC(6.0–5.0/step/180 min)	307	30.2	29.6	25.1	36	8.9
MC(6.0–4.5/step/180 min)	307	29.9	40.0	35.5	51	9.4
MC(6.0–5.5–5.0/step/180 min)	313	29.4	18.6	14.2	20	8.4
MC(6.0–5.5/linear/180 min)	318	10.1	24.3	22.8	25	2.6
MC(6.0–5.0/linear/180 min)	329	28.8	17.5	13.3	19	8.6
MC(6.0–4.5/linear/180 min)	347	29.8	19.0	14.5	21	9.9

*average weight loss of the isolated MF resins

and Higgs [32] and Devallencourt *et al*. [33]. For Melapret NF 70/M the first significant weight loss occurs at the temperature around 160°C, which can be attributed to evaporation of methanol, formaldehyde and water during curing reactions. The next major weight loss step occurs above 350°C, when the methylene bridges start to breakdown. Above 400°C the three-dimensional polymer structure of MF resin continues to decompose slowly. At these temperatures ammonia, formaldehyde and other volatile decomposition products are released. The nonvolatile residue contains –NH– bridges between melamine rings as well as different cyameluric structures [33]. In isolated cured MF resins the decrease of weight starts already below 100°C, presumably as a result of adsorbed water on MF resin. With increasing the temperature (140–260°C), MF resin starts to cure and the weight loss can be ascribed to evaporation of water, formaldehyde and methanol. As these resins were partially cured [28] before TGA analysis, the weight loss due to crosslinking reactions is smaller compared to uncured MF resin Melapret NF 70/M. At temperatures above 280°C weight loss is visible, which can be mainly ascribed to transformation of dimethylene ether bridges to methylene bridges. The weight loss step of isolated MF resin due to decomposition of methylene bridges is not as distinctive as in the case of Melapret NF 70/M and shifts towards higher temperatures (400°C).

TGA curves of butyl stearate and microcapsules isolated at the end of microencapsulations are shown in Figure 9. At temperatures below 140°C the differences between samples are minimal and are due to weight loss caused by the adsorbed water evaporation. The remaining parts of TGA curves have two main weight loss stages. The first stage is in the temperature range between 140–300°C, where weight loss can be attributed mainly to evaporation of butyl stearate. Namely, microcapsules contained 70 wt% or more of core material. Of course, a certain part of weight decrease in this temperature range must also be ascribed to the evaporation of water, methanol and formaldehyde as a consequence of MF resin curing reactions. However, considering the core/shell ratio the thermal degradation of MF resin may be ascribed to a maximum of 4.5 wt% decrease in this temperature range (Figure 8). The second main weight decrease for microcapsules occurs above 350°C, where MF shell was unable to hold the expanding core material and its decomposition products within microcapsules due to enhanced disintegration of three-dimensional resin structure.

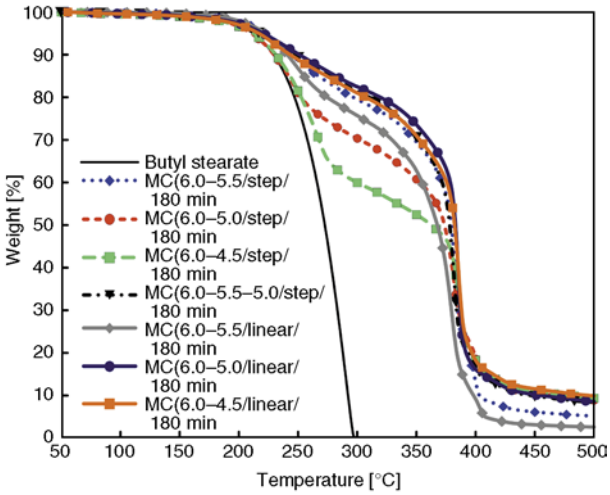

Figure 9. TGA curves of butyl stearate and microcapsules isolated at 180 minutes

For the purpose of comparing thermal stabilities of microcapsules obtained at different pH lowering regimes we focused on the weight losses at temperature point of 300°C, since 300°C is the temperature where butyl stearate exhibited 100% weight loss. By comparing the results of TGA analysis of samples after 180 minutes of microencapsulation (Table 2) we can observe that samples MC(6.0–4.5/step/180 min), MC(6.0–5.0/step/180 min) and MC(6.0–5.5/linear/180 min) had the highest weight loss in respective order. Other samples have comparable weight losses at 300°C. Distinct weight losses were calculated from the determined core/shell mass ratio (DSC measurements) and TGA results of pure butyl stearate and isolated MF resins. Weight percentage of evaporated core material was obtained by dividing weight loss on the account of core material at 300°C by weight percentage of core material in microcapsules before TGA analysis. Based on the results, presented in Table 2 it may be concluded, that in microcapsules MC(6.0–5.0/linear/180 min) only 19% of the core material evaporated till 300°C. On the other hand, in microcapsules MC(6.0–5.0/step/180 min), a 36 wt% loss of the core material was observed. The lower thermal stability of sample MC(6.0–5.0/step/180 min) may be explained by its thinner shell thickness since both samples contained around 30 wt% of shell

material. Shell thickness of sample MC(6.0–5.5–5.0/step/180 min) was between samples MC(6.0–5.0/linear/180 min) and MC(6.0–5.0/step/180 min). Therefore it may be concluded that if the end pH value is fixed, thermal stability of microcapsules increases with increasing the shell thickness, which is strongly dependent on the pH value lowering regime.

By comparing the results of the microcapsules obtained by lowering the pH value to different end values in one step, we can observe that a large pH value drop had a negative effect on thermal stability. In this case the shell thickness could not be the reason for the differences we noticed, since the shell thickness for all the samples (MC(6.0–4.5/step/180 min), MC(6.0–5.0/step/180 min) and MC(6.0–5.5/step/180 min), presented in Table 2, was the same. The reason may be due to the crosslink density of the MF shell, which is, together with shell thickness, the most important factor for good thermal stability of microcapsules. In the case of a large step decrease of the pH value, the curing of MF resin was strongly accelerated. Consequently, this leads to the formation of a thin outer layer of higher cured MF shell. On the other hand, the inner part of microcapsules shell (which was not in contact with the continuous phase with lowered pH value) remained less cured. Moreover, despite the fact that curing was faster, the crosslinking and resin density were lower at lower pH values. Namely, at high curing rate the crosslinking bonds are formed quickly and the molecules do not have sufficient time to orient themselves in positions to form the maximal number of crosslinks. A lower crosslink density results in a brittle and permeable MF shell.

To determine the changes in thermal stability of microcapsules during microencapsulation, and to prove that large pH value decrease in stepwise procedure has indeed a negative influence on thermal stability of microcapsules, microcapsules were also investigated for MC(6.0–5.0/step), MC(6.0–5.5–5.0/step) and MC(6.0–5.0/linear) at 60 and 120 minutes. Detailed results of TGA analysis of the core material, isolated MF shell material and microcapsules isolated at 60, 120 and 180 minutes of microencapsulations MC(6.0–5.0/step), MC(6.0–5.5–5.0/step) and MC(6.0–5.0/linear) are presented in Table 3. Due to identical reaction parameters till 60 minutes of microencapsulations, TGA curves for MC(6.0–5.0/step/60 min), MC(6.0–5.5–5.0/step/60 min) and MC(6.0–5.0/linear/60 min) are similar, as it was expected from the results of SEM analysis, i.e. microcapsules isolated at 60 minutes had identical morphology and comparable shell thicknesses. Minor differences between TGA with the microcapsules isolated at 60 minutes could be attributed to the fragile shells of microcapsules (possible rupture of microcapsules). Since different regimes of the pH value decrease were employed, there was also a greater differentiation in thermal stability of the microcapsules. While thermal stability of MC(6.0–5.0/linear) and MC(6.0–5.5–5.0/step) microcapsules increased with decreasing the pH value, the stability of microcapsules MC(6.0–5.0/step) decreased. In MC(6.0–5.0/step) the weight loss of the core material decreased from starting 28% at 60 minutes

Table 3. Results of TGA analysis of core material, isolated MF resins and microcapsules isolated at 60, 120 and 180 minutes of microencapsulations MC(6.0–5.0/step), MC(6.0–5.5–5.0/step) and MC(6.0–5.0/linear)

Sample	Shell thickness [nm]	MF resin [wt%]	At 300°C			Residue at 500°C [wt%]
			Total weight loss [wt%]	Weight loss on account of core material [wt%]	Evaporated core material [wt%]	
butyl stearate	–	0	100	100	100	0
isolated MF resins	–	100	15*	0	0	32
MC(6.0–5.0/step/60 min)	290	8.4	26.9	25.6	28	1.7
MC(6.0–5.0/step/120 min)	301	29.1	41.1	36.7	52	7.9
MC(6.0–5.0/step/180 min)	307	30.2	29.6	25.1	36	8.9
MC(6.0–5.5–5.0/step/60 min)	290	7.3	25.1	24.0	26	1.7
MC(6.0–5.5–5.0/step/120 min)	299	9.6	22.1	20.7	23	1.7
MC(6.0–5.5–5.0/step/180 min)	313	29.4	18.6	14.2	20	8.4
MC(6.0–5.0/linear/60 min)	298	8.4	23.8	22.5	25	2.0
MC(6.0–5.0/linear/120 min)	323	9.5	20.8	19.4	21	2.1
MC(6.0–5.0/linear/180 min)	329	28.8	17.5	13.2	19	8.6

*average weight loss of the isolated MF resins

to 52% at 120 minutes of microencapsulation. As microencapsulation continued, thermal stability of microcapsules MC(6.0–5.0/step) increased again. Weight loss due to core material evaporation was 36% in MC(6.0–5.0/step/180 min). Initial decrease of thermal stability could be explained by the formation of thin highly cured and less crosslinked outer layer of the microcapsules shell, while the inner layer was still incompletely cured. The shell, being rigid and thin, has lower mechanical stability, and consequently it is less able to retain core material. With microencapsulation time the inner layer of microcapsule shell slowly cures and the thermal stability of microcapsules increases.

4. Conclusions

In this paper we investigated the influence of different pH regimes during preparation of PCM microcapsules by *in situ* polymerization with melamine-formaldehyde resin on the composition of microcapsules, their morphology and stability. While on the one hand the decrease to a low pH value in one step resulted in a rapid increase of the weight percentage of MF resin in samples, thermal stability and morphology of microcapsules were unsatisfactory on the other. To attain better thermal stability it is necessary to ensure slow curing reaction and deposition of the MF resin on the microcapsule surface, which can be achieved by decreasing the pH value during microencapsulation in several smaller steps or in a linear way. With linear decrease of the pH value, microcapsules with thicker and better cured MF shells were obtained.

Acknowledgements

The financial support of this work by the Slovenian Ministry of Higher Education, Science and Technology is gratefully acknowledged.

References

[1] Ghosh S. K.: Functional coatings and microencapsulation: A general perspective. in: 'Functional coatings' (ed.: Ghosh S. K.) Wiley, Weinheim, 1–28 (2006). DOI: 10.1002/3527608478.ch1

[2] Shan X. L., Wang J. P., Zhang X. X., Wang X. C.: Formaldehyde-free and thermal resistant microcapsules containing *n*-octadecane. Thermochimica Acta, **494**, 104–109 (2009). DOI: 10.1016/j.tca.2009.04.026

[3] You M., Zhang X. X., Li W., Wang X. C.: Effects of microPCMs on the fabrication of microPCMs/polyurethane composite foams. Thermochimica Acta, **472**, 20–24 (2008). DOI: 10.1016/j.tca.2008.03.006

[4] Sarier N., Onder E.: The manufacture of microencapsulated phase change materials suitable for the design of thermally enhanced fabrics. Thermochimica Acta, **452**, 149–160 (2007). DOI: 10.1016/j.tca.2006.08.002

[5] Li W., Zhang X-X., Wang X-C., Niu J-J.: Preparation and characterization of microencapsulated phase change material with low remnant formaldehyde content. Materials Chemistry and Physics, **106**, 437–442 (2007). DOI: 10.1016/j.matchemphys.2007.06.030

[6] Zhang X-X., Tao X-M., Yick K-L., Wang X-C.: Structure and thermal stability of microencapsulated phase-change materials. Colloid and Polymer Science, **282**, 330–336 (2004). DOI: 10.1007/s00396-003-0925-y

[7] Su J-F., Huang Z., Ren L.: High compact melamine-formaldehyde microPCMs containing *n*-octadecane fabricated by a two-step coacervation method. Colloid and Polymer Science, **285**, 1581–1591 (2007). DOI: 10.1007/s00396-007-1729-2

[8] Zhang X-X., Fan Y-F., Tao X-M., Yick K-L.: Crystallization and prevention of supercooling of microencapsulated *n*-alkanes. Journal of Colloid and Interface Science, **281**, 299–306 (2005). DOI: 10.1016/j.jcis.2004.08.046

[9] Fan Y. F., Zhang X. X., Wu S. Z., Wang X. C.: Thermal stability and permeability of microencapsulated *n*-octadecane and cyclohexane. Thermochimica Acta, **429**, 25–29 (2005). DOI: 10.1016/j.tca.2004.11.025

[10] Mondal S.: Phase change materials for smart textiles – An overview. Applied Thermal Engineering, **28**, 1536–1550 (2008). DOI: 10.1016/j.applthermaleng.2007.08.009

[11] Salaün F., Devaux E., Bourbigot S., Rumeau P.: Thermoregulating response of cotton fabric containing microencapsulated phase change materials. Thermochimica Acta, **506**, 82–93 (2010). DOI: 10.1016/j.tca.2010.04.020

[12] Sun G., Zhang Z.: Mechanical properties of melamine-formaldehyde microcapsules. Journal of Microencapsulation, **18**, 593–602 (2001). DOI: 10.1080/02652040010019541

[13] Sun G., Zhang Z.: Mechanical strength of microcapsules made of different wall materials. International Journal of Pharmaceutics, **242**, 307–311 (2002). DOI: 10.1016/s0378-5173(02)00193-x

[14] Su J-F., Wang S-B., Zhou J-W., Huang Z., Zhao Y-H., Yuan X-Y., Zhang Y-Y., Kou J-B.: Fabrication and interfacial morphologies of methanol–melamine–formaldehyde (MMF) shell microPCMs/epoxy composites. Colloid and Polymer Science, **289**, 169–177 (2011).
DOI: 10.1007/s00396-010-2334-3

[15] Salaün F., Vroman I.: Influence of core materials on thermal properties of melamine–formaldehyde microcapsules. European Polymer Journal, **44**, 849–860 (2008).
DOI: 10.1016/j.eurpolymj.2007.11.018

[16] Su J., Wang L., Ren L.: Fabrication and thermal properties of microPCMs: Used melamine-formaldehyde resin as shell material. Journal of Applied Polymer Science, **101**, 1522–1528 (2006).
DOI: 10.1002/app.23151

[17] Dietrich K., Bonatz E., Geistlinger H., Herma H., Nastke R., Purz H-J., Schlawne M., Teige W.: Amino resin microcapsules. II. Preparation and morphology. Acta Polymerica, **40**, 325–331 (1989).
DOI: 10.1002/actp.1989.010400507

[18] Dietrich K., Bonatz E., Nastke R., Herma H., Walter M., Teige W.: Amino resin microcapsules. IV. Surface tension of the resins and mechanism of capsule formation. Acta Polymerica, **41**, 91–95 (1990).
DOI: 10.1002/actp.1990.010410205

[19] Thies C.: A survey of microencapsulation processes. in 'Microencapsulation: Methods and industrial application' (ed.: Benita S.) Marcel Dekker, New York, 133–154 (1996).

[20] Lee H. Y., Lee S. J., Cheong I. W., Kim J. H.: Microencapsulation of fragrant oil via *in situ* polymerization: Effects of pH and melamine-formaldehyde molar ratio. Journal of Microencapsulation, **19**, 559–569 (2002).
DOI: 10.1080/02652040210140472

[21] Zhang H., Wang X.: Fabrication and performances of microencapsulated phase change materials based on *n*-octadecane core and resorcinol-modified melamine–formaldehyde shell. Colloids and Surfaces A: Physicochemical and Engineering Aspects, **332**, 129–138 (2009).
DOI: 10.1016/j.colsurfa.2008.09.013

[22] Yuan Y. C., Rong M. Z., Zhang M. Q.: Preparation and characterization of microencapsulated polythiol. Polymer, **49**, 2531–2541 (2008).
DOI: 10.1016/j.polymer.2008.03.044

[23] Yuan L., Liang G-Z., Xie J-Q., He S-B.: Synthesis and characterization of microencapsulated dicyclopentadiene with melamine–formaldehyde resins. Colloid and Polymer Science, **285**, 781–791 (2007).
DOI: 10.1007/s00396-006-1621-5

[24] Zhang X. X., Fan Y. F., Tao X. M., Yick K. L.: Fabrication and properties of microcapsules and nanocapsules containing *n*-octadecane. Materials Chemistry and Physics, **88**, 300–307 (2004).
DOI: 10.1016/j.matchemphys.2004.06.043

[25] Wang H., Yuan Y., Rong M., Zhang M.: Microencapsulation of styrene with melamine-formaldehyde resin. Colloid and Polymer Science, **287**, 1089–1097 (2009).
DOI: 10.1007/s00396-009-2072-6

[26] Yu F., Chen Z-H., Zeng X-R.: Preparation, characterization, and thermal properties of microPCMs containing *n*-dodecanol by using different types of styrene-maleic anhydride as emulsifier. Colloid and Polymer Science, **287**, 549–560 (2009).
DOI: 10.1007/s00396-009-2001-8

[27] Kamio E., Kato A., Yonemura S., Ono T., Yoshizawa H.: Preparation of monodisperse crosslinked polymelamine microcapsules by phase separation method. Colloid and Polymer Science, **286**, 787–793 (2008).
DOI: 10.1007/s00396-008-1837-7

[28] Alič B., Šebenik U., Krajnc M.: Differential scanning calorimetric examination of melamine–formaldehyde microcapsules containing decane. Journal of Applied Polymer Science, **119**, 3687–3695 (2011).
DOI: 10.1002/app.33077

[29] Okano M., Ogata Y.: Kinetics of the condensation of melamine with formaldehyde. Journal of the American Chemical Society, **74**, 5728–5731 (1952).
DOI: 10.1021/ja01142a047

[30] Kumar A., Katiyar V.: Modeling and experimental investigation of melamine-formaldehyde polymerization. Macromolecules, **23**, 3729–3736 (1990).
DOI: 10.1021/ma00218a003

[31] Kandelbauer A., Wuzella G., Mahendran A., Taudes I., Widsten P.: Model-free kinetic analysis of melamine–formaldehyde resin cure. Chemical Engineering Journal, **152**, 556–565 (2009).
DOI: 10.1016/j.cej.2009.05.027

[32] Manley T. R., Higgs D. A.: Thermal stability of melamine formal-dehyde resins. Journal of Polymer Science: Polymer Symposia, **42**, 1377–1382 (1973).
DOI: 10.1002/polc.5070420337

[33] Devallencourt C., Saiter J. M., Fafet A., Ubrich E.: Thermogravimetry/Fourier transform infrared coupling investigations to study the thermal stability of melamine formaldehyde resin. Thermochimica Acta, **259**, 143–151 (1995).
DOI: 10.1016/0040-6031(95)02262-z

eXPRESS Polymer Letters Vol.6, No.10 (2012) 837–846
Available online at www.expresspolymlett.com
DOI: 10.3144/expresspolymlett.2012.89

Effect of different ligands on the controlled polymerization of monodisperse polystyrene nanospheres by atom transfer radical polymerization in an aqueous emulsion

B. Y. Tian[1,2], P. J. Hu[1], M. Yuan[1], E. J. Tang[1,2], S. J. Liu[1,2], X. Y. Zhao[2], D. S. Zhao[1,2]*

[1]School of chemical and pharmaceutical engineering, Hebei University of Science and Technology, 050018 Shijiazhuang Hebei, China
[2]Hebei research center of pharmaceutical and chemical engineering, Hebei University of Science and Technology, 050018 Shijiazhuang Hebei, China

Received 14 March 2012; accepted in revised form 15 May 2012

Abstract. Polystyrene nanospheres have been synthesized by atom transfer radical polymerization (ATRP) to control the molecular weight distribution in the aqueous system. The crucial factor in such a system is the ligand that adjusts the solubility of the catalyst in different phases to control the concentration of both the activator and the deactivator in reaction phase. The effect of different ligands including ethylenediamine, 1,10-phenanthroline (phen) and 4,4-dinonyl-2, 2-bipyridyl (dNbpy) on the catalytic solubility in the organic and aqueous phase has been investigated. The molecular weight distribution of polymer obtained in this way was analyzed by gel permeation chromatography (GPC). It showed that the obtained polymer particles presented a broad molecular weight distribution (polydispersity index 1.78) with ethylenediamine as the ligand, but the polymerization rate was high and conversion reached 96.8%. The molecular weight distribution of polystyrene was narrowest with dNbpy as ligand, but the conversion was lowest and only achieved to 69%. Possible reasons were the influence of the structure of three different ligands on the control of ATRP reaction. SEM and GPC indicated that the polystyrene nanospheres presented regular sphere with a diameter of about 120 nm and uniform molecular weight distribution, which possessed a significant potentials in drug carrier field.

Keywords: *polymer synthesis, ATRP, aqueous emulsion polymerization, polystyrene nanosphere, ligand*

1. Introduction

Monodisperse polymer nanospheres have found a wide variety of applications in coating, instrument calibration, chromatography and biomedical treatment etc [1]. However, polymer materials produced by traditional radical polymerization have a broad molecular weight distribution. Many applications require particles consisting of a pre-defined molecular weight and a narrow molecular weight distribution [2]. Control over the polymer molecular weight and its distribution during polymerization has long been a challenge in polymer material research, especially in the applications for medicine release material and as biotechnology materials [3, 4]. The advent of atom transfer radical polymerization (ATRP) provides a new way to synthesize polymers with controlled molecular weight [5–7]. Numerous well-defined (co)polymers with the desired molecular weight and low polydispersity index (PDI <1.5) [8, 9], (co)polymers with complex architectures [10–13], functional polymers and hybrid materials have been prepared by the ATRP technique [14–16]. Atom transfer radical polymerization (ATRP) also remains one of the most powerful, versatile,

*Corresponding author, e-mail: ejtang@sohu.com

simplest, and least expensive polymerization techniques [17]. Not only does this feature offer ability to tailor the polymer coatings to possess a variety of compositions and functionality, but this feature may be important in biomedical applications to modify a biological polymer specifically for cellular interactions [18, 19]. The basis of the ATRP technique is the reversible transfer of a halogen atom from a polymeric alkyl halide (R–X) to a transition metal complex (LMtn), generating an organic radical and a transition metal complex (LMtn+1X) with a higher oxidation state [20]. To establish the equilibrium between LMtn and LMtn+1X so that it is strongly shifted toward the LMtn complex, many factors should be taken into consideration, involving the monomer, initiator with a transferable halogen, catalyst (composed of a transition metal species with any suitable ligand), solvent and temperature [21].

Over the past few years, extensive studies on ATRP have mainly focused on homogeneous bulk or solution systems to obtain a variety of well-defined (co)polymers with controlled molecular weights. Its use has been demonstrated for the synthesis of a series of functional monomers such as (meth)acrylate, (meth)acrylamide and (meth)acrylic acids, giving the target polymers better control of the molecular weight and distribution [22–25]. Currently, in order to meet the requirements for environmentally benign technology and the development of sustainable chemistry, some new strategies are beginning to be pursued. The major approach is based on using water as the solvent, both from an environmental view and safety related reasons [26, 27]. In aqueous dispersed media, such as an emulsion or suspension, the polymerization is able to effectively transfer heat from exothermic polymerization processes and allows a dramatic increase of the polymerization rate [28]. The polymer nanospheres produced in this way can be used directly in drug delivery, microencapsulation and many other applications [29]. However, unlike bulk/solution ATRP, to maintain the 'living' character of the polymerization in a stable emulsion, many factors need to be considered. For instance, the choice of an appropriate surfactant, the solubility of the initiator and the radical trapping agent in both the organic and aqueous phases, avoidance of any potential side reactions caused by water and a high reaction temperature, all require attention. Among these, the choice of ligand is a crucial factor that adjusts the catalytic solubility in the organic and aqueous phases and has a tremendous impact on the controlled polymerization. It should be noted that a further requirement of the ligand (such as dNbpy) for aqueous dispersion is that it must form soluble catalyst complexes with the chosen monomer. The ligand can then improve the retention of the catalyst in the particle phase where polymerization takes place and minimize partitioning into the aqueous phase. However, it is well known that even with a hydrophobic ligand, not all of the catalyst complex can be prevented from partitioning into the aqueous phase [28].

The object of this work was to investigate the ability to control the molecular weight and latex stability of polystyrene nanospheres using ATRP in an aqueous emulsion system. The ligand adjusts the solubility of the catalyst in the different phases to control the concentration of both the activator and the deactivator in the reaction phase. The selection of the ligand becomes a key for controlling the reaction and molecular weight in the aqueous system. Ethylenediamine, phen and dNbpy were used as ligands with various experimental conditions. The influence of the ligands on the conversion and molecular weight distributions is then discussed. The reason for the different results obtained is analysed primarily by consideration of the solubility of the metal-ligand complexes in the organic phase and the structure of ligand.

2. Experimental

2.1. Materials

Commercially available styrene (St) was purchased from Beijing Dong fang Chemical Co. Ltd. (China). The St was distilled under reduced pressure and then kept refrigerated until used. Nonyl phenyl ether polyoxyethylene (10) (OP-10, AR) and sodium dodecyl sulfate (SDS) were obtained from the Beijing Chemical Plant (Beijing, China) and used without further purification. Copper chloride (CuCl, AR), carbon tetrachloride (CCl_4, AR), hexadecane (HD, AR) and polyoxyethylene sorbitan monoleate (TW-80, AR) were supplied by Tianjin Chemistry Reagent Co, Ltd, China. 1, 10-phenanthroline (phen, analytically pure) and ethylenediamine (analytically pure) were supplied by the Tianjin Research

Institute of Synthetic Material (China) and used without further purification. 4, 4-dinonyl-2, 2-bipyridyl (dNbpy), analytically pure, was purchased from the Hangzhou Chemistry Co. Ltd. (China). Deionized water was used for all polymerization and characterization processes.

2.2. Polymerization procedure

The polymerization was conducted in a flask fitted with a mechanical stirrer, nitrogen inlet and condenser. Copper(I) chloride (0.15 g) and different amounts of ligand were directly dispersed into monomers. The monomer mixture was added to an aqueous solution of the surfactant with hexadecane and then dispersed for 20 min (450 W) using an ultrasonic instrument (KQ-2300, 150 W, China) at room temperature. Afterwards, the mixture was added to a flask with constant stirring under high purity nitrogen (N_2 99.999%). The reactor was immersed in a thermostated water bath to maintain a constant temperature. A certain amount of CCl_4 was added to the reaction system held at the specified temperature (80°C) and the time noted. The polymerization reaction was carried out at constant temperature for 8 h to obtain the latex nanospheres.

2.3. Characterization

The monomer conversion was determined by a conventional gravimetric method. The molecular weight and the distribution of the polymer were characterized by gel permeation chromatography (GPC, HLC-8220) on a system equipped with a SHIMADZU (LC-10ADVP) pump and a RID-10A detector, with THF as the eluent and a flow rate of 1 mL/min. Narrow-standard polystyrene was used to generate a universal calibration curve. The partitioning of the complexes which were formed by the CuCl and different ligands were determined by UV–VIS spectrophotometry [29]. The latex nanosphere diameter was determined using a dynamic light scattering particle size analyzer (DLS BI-90Plus, Brookhaven Instruments Co., USA). The dispersion morphology of the particles in the latex system was observed using transmission electron microscopy (TEM 100CX-II, Jeol Co., Japan).

3. Results and discussion

3.1. The mechanism of synthesizing polystyrene nanospheres with ATRP in emulsion system

For this part of the investigation, a certain amount of emulsifier TW-80 was added to the reaction system to emulsify the organic monomer using the ultrasonic emulsification instrument in an aqueous system [30]. Subsequently, a large quantity of miniemulsion droplets was obtained and the ATRP reaction was carried out in the monomer droplets to obtain the nanosphere materials. The mechanism for the synthesis of the polystyrene latex nanospheres is shown in Figure 1. At the beginning of polymerization, copper(I) chloride and ligand were dispersed into monomers and the mixture was dispersed ultrasonically. The ligand can increase the solubility of the catalyst in the organic phase, so that the complex is diffused into the monomer droplets at the beginning of the polymerization. A certain amount of initiator CCl_4 was then added to the reaction system. In the initiation step, the transition metal complex abstracts the halogen from the organic halides, creating a radical that adds to the monomer; the resulting radical species then propagates further. As the radical propagation reaction takes place, it is rapidly deactivated by a reaction with the oxidized transition-metal/ligand complex, regenerating a halogen-terminated polymeric chain [31]. Through the equilibrium between the activator and the deactivator in the reaction droplets, polymer particles with a narrow molecular weight distribution were obtained using this ATRP method.

For this system, the transition-metal/ligand complex is located in the organic monomer phase (styrene) where the ATRP reaction takes place. In

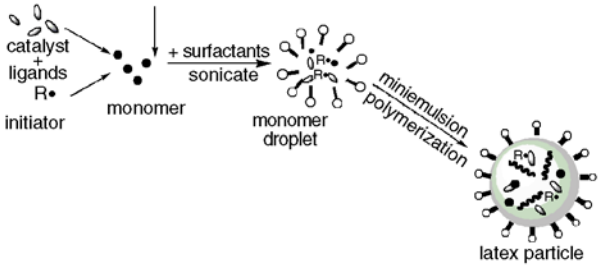

Figure 1. The mechanism of synthesizing polystyrene nanospheres by ATRP in miniemulsion droplets

addition, it may be located in aqueous phase, depending on the solubility of the ligand. If the majority of the complex remains in the organic phase, the control polymerization would be easily carried out. If not, the transition metal complex can diffuse into the aqueous phase and the radical species may be difficult to deactivate. The trend of radical propagation polymerization would play a major role. As a consequence, the controlled polymerization could not be completed perfectly and the molecular weight distribution of the polymer obtained would be broadened.

3.2. Solubility of the different catalytic system in organic and aqueous phase

The partition of the complexes which formed by CuCl and different ligands were determined by UV-VIS spectrophotometry [29]. Figure 2 shows the UV-VIS absorption spectrum curve of complex which formed by CuCl/ethylenediamine. A comparison of the absorption spectra of the complex in the organic phase and aqueous phase before and after mixing with water revealed a remarkable change at the relative intensity of the peaks around 580 nm. The resulting complex had a very low solubility in organic phase before mixing with water, but stronger characteristic absorption peak emerged in the aqueous phase after mixing with water. Figure 3 shows that the complex which formed with CuCl and phen emerged stronger characteristic absorption peak around 660 nm before mixed with water, and the absorption peak around 660 nm was weakened in the organic phase after mixing with water. Figure 4 shows that the complex (CuCl/dNbpy) exhibited stronger characteristic absorption peak around 460 nm in the organic phase.

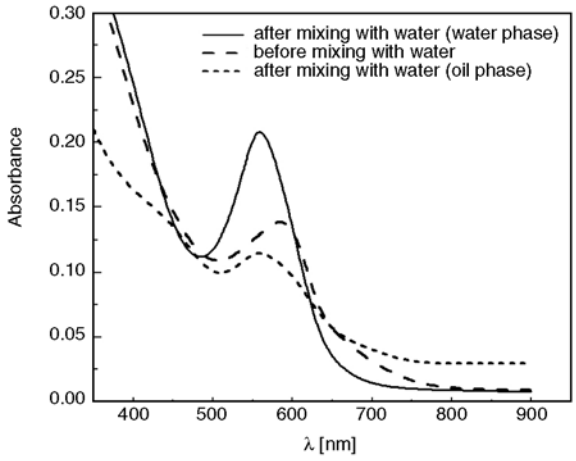

Figure 2. The absorbance of complex which formed CuCl/ethylenediamine. Temperature: 25°C; [CuCl]/[ethylenediamine]:1/2; the oil phase was styrene.

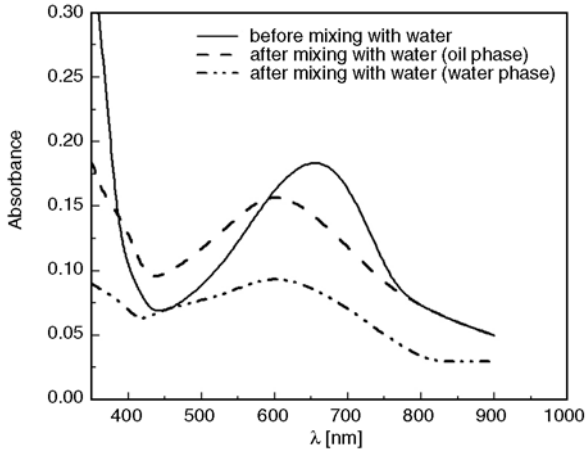

Figure 3. The absorbance of complex which formed CuCl/phen. Temperature: 25°C; [CuCl]/[phen]:1/2; the oil phase was styrene.

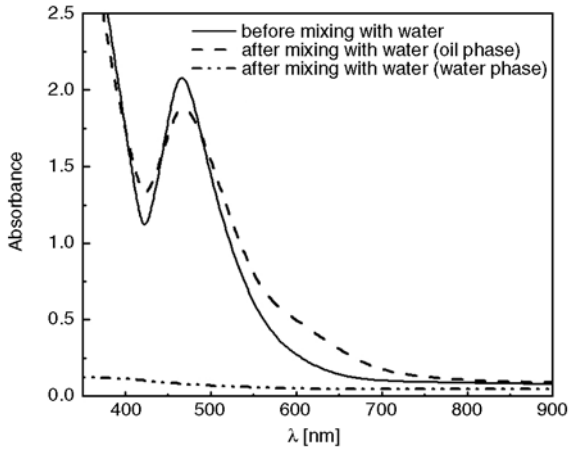

Figure 4. The absorbance of complex which formed CuCl/dNbpy. Temperature: 25°C; [CuCl]/[dNbpy]:1/2; the oil phase was styrene.

By comparing the three different metal complexes, the results indicated that CuCl/ethylenediamine was highly soluble in water phase and a lot of complexes were easily migrated to the aqueous phase. However, the complex of CuCl/dNbpy exhibited stronger characteristic absorption peak in the visible range. That is to say, the complexes had a stronger solubility in organic phase and the majority of the complex remains in the organic phase after mixing with water. The solubility of CuCl/phen in organic phase was between the two complexes mentioned above.

In ATRP, equilibrium switching between the n and $n+1$ oxidation states was achieved by using a metal complex [32]. Since the polymer chains grow in the organic phase, the first requirement for control of

the polymerization is to have a sufficient concentration of both the activator and the deactivator in the organic phase where reaction is to take place. The ligand increases the solubility of the catalyst in the organic phase. Therefore the choice of the proper ligand becomes crucial.

3.3. Influence of different kinds of ligands on the control of the ATRP reaction

The key to controlling the radical polymerization is to maintain a rapid equilibrium between the growing radicals and the dormant species. To facilitate a successful ATRP, it is essential to have both a radical activator and deactivator available in the organic phase where the polymerization takes place [33]. One role of the ligand is to adjust the partitioning behavior of the metal complex between the oil phase and the aqueous phase. Thus, the selection of a suitable ligand becomes essential.

In this system, CuCl was added to the ATRP system to facilitate the establishment of the equilibrium between the radical and dormant species. The relationship of the molecular weight versus conversion and that of conversion versus time with ethylenediamine as the ligand are shown in Figures 5a and 5b. It can be seen that the polymer finally obtained had a very broad molecular weight distribution with a polydispersity index of 1.78. A long tail was found in the GPC curves with a conversion of 96.8%. In contrast, experiments with phen and dNbpy as the ligand system were also carried out. Figures 6a and 6b show the relationship of conversion versus time and the relationship of molecular weight versus conversion with phen as the ligand. The results revealed that the conversion of styrene gradually increased with the polymerization time. The polymer obtained with phen as ligand had a narrow molecular weight distribution (PDI:1.65) and lat-

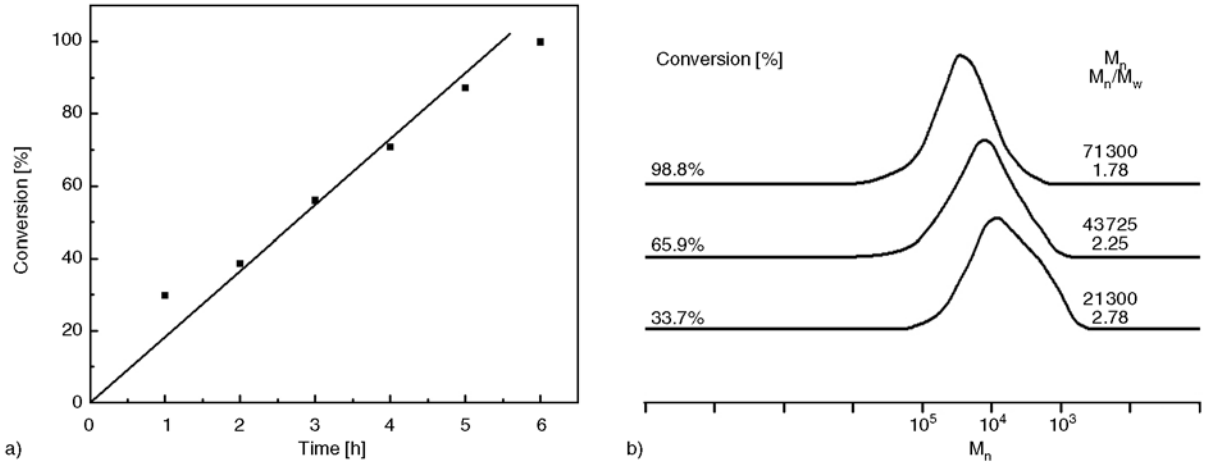

Figure 5. The relationship of conversion versus time (a) and that of molecular weight versus conversion with ethylenediamine as ligand (b)

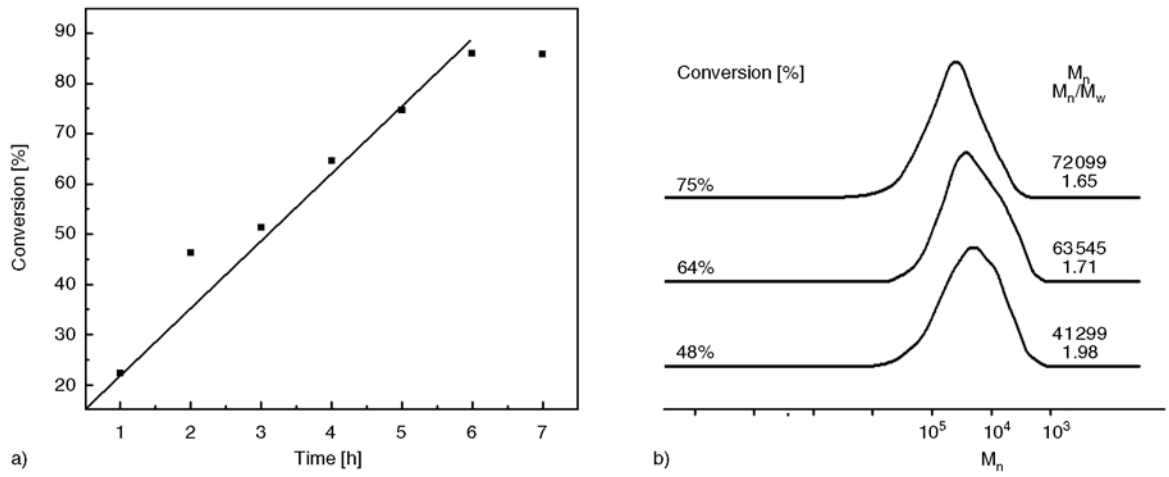

Figure 6. The relationship of conversion versus time (a) and that of molecular weight versus conversion with phen as ligand (b)

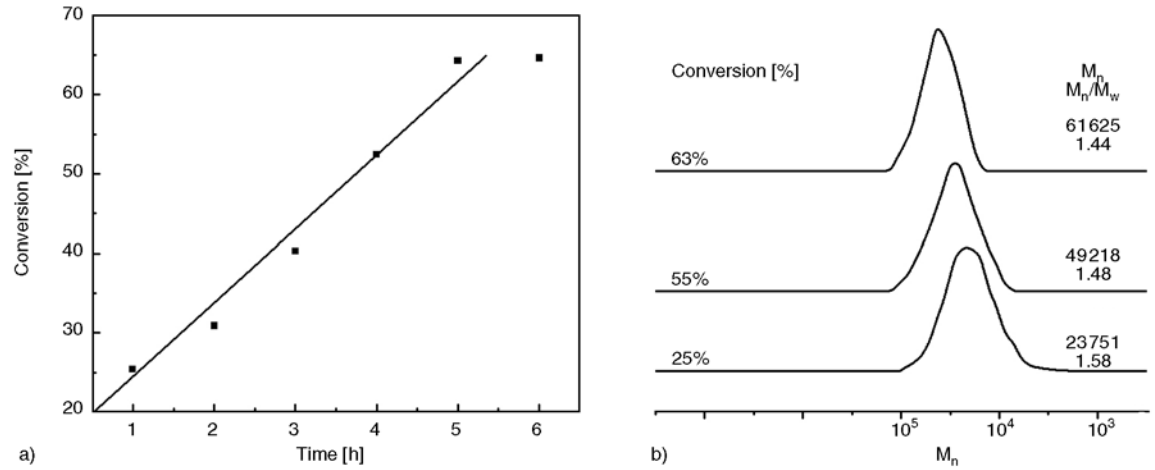

Figure 7. The relationship of conversion versus time (a) and that of molecular weight versus conversion with dNbpy as ligand (b)

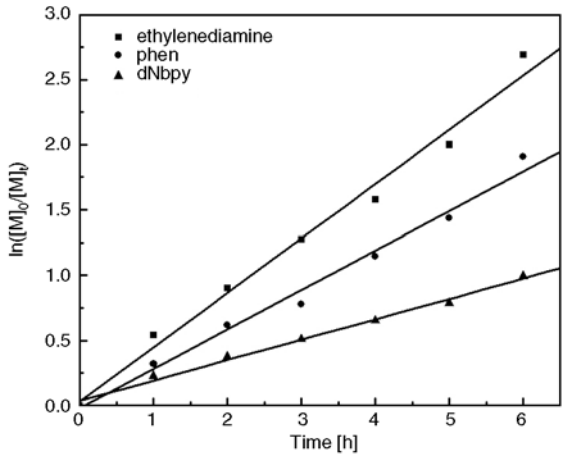

Figure 8. The relationship of $\ln([M]_0/[M]_t)$ versus time for the emulsion ATRP of St with three different ligand(ethylenediamine, phen, dNbpy)

eral shift with increasing of conversion towards higher molecular weight. Figures 7a and 7b show the relationship of conversion versus time and the relationship of molecular weight versus conversion with dNbpy as ligand. The molecular weight distribution of polystyrene was the narrowest (PDI:1.44) of the three samples, but the conversion was also lowest, only reaching 69%. Figure 8 shows the relationship of $\ln([M]_0/[M]_t)$ versus time of the emulsion ATRP of St with the three different ligands (ethylenediamine, phen, dNbpy). It shows that the polymerization rate obeyed almost first order kinetics [34]. The polymerization rate with the CuCl/ethylenediamine system was faster than either the CuCl/dNbpy or CuCl/phen systems.

From the above results we found that phen and dNbpy had higher solubility in the organic phase, especially dNbpy. The hydrophobic ligand can increase the solubility of the catalyst in the organic phase where the polymerization takes place. So the most efficiently controlled polymerization (giving a polydispersity below 1.50) was produced using the CuCl/dNbpy complex which facilitated a balance between the activation and deactivation processes in the reaction phase. dNbpy has stronger solubility in the organic phase, so it was employed effectively as a ligand for the ATRP in the emulsion and miniemulsion systems [35]. However, the catalytic activity of the copper complex with dNbpy is rather low and requires a high polymerization temperature, which reduces the stability of the monomer droplets/growing particles and leads to lower conversion during the polymerization.

The reason is possibly due to the different structures of the ligands. It can be found from the structure of the ethylenediamine ligand that the lower steric hindrance around the nitrogen atom was conducive to form the living radical more quickly and so increased the polymerization rate. The above results therefore indicated that CuCl/ethylenediamine was highly soluble in water and a large quantity of the complexes easily migrated to the aqueous phase. As a result, the particles produced can undergo an uncontrolled conventional free radical polymerization due to the absence of the copper complex as deactivator/activator. With the long alkyl substituent of dNbpy as ligand, the steric hindrance around the nitrogen atoms was significant. To a certain extent, large steric hindrance hindered the formation of a living radical. At the same time the copper complex

with dNbpy was rather unstable, which decreased the activity of the catalyst. In order to increase the catalytic activity, high polymerization temperature was required, but high temperature reduces the stability of the monomer droplets/growing particles during the polymerization.

In addition, the good oil-solubility of the ligand played a beneficial role for controlling the reaction. Therefore, the experiments demonstrated that the effect of ATRP on the controllability not only depended on the solubility of the catalyst complex in the organic phase, but also depended on its ability for radical trapping.

3.4. The selection of surfactant in emulsion of ATRP

The influence of latex stability with different types emulsifiers on the reaction system was studied with dNbpy as ligand (Table 1). It appeared that the stability of system with SDS as emulsifier was poor and the polymer presented a broad molecular weight distribution. The ionic surfactants appeared to be not suitable for the emulsion ATRP [36]. The possible reason was that the system had a lot of hydrophilic groups $–SO_4Na$, which finally led to the system instability. Nonionic surfactant, however, was good candidates for emulsion ATRP. But OP-10 did not stabilize the system and the latex particles were coagulated after 2 h from the beginning of polymerization. Among the surfactants in this work, the nonionic Tween 80 presented a perfect result. It obtained a stable reaction system and showed a good livingness for the conversion and control molecular weight of polystyrene nanosphere. Therefore, Tween 80 was employed as emulsifier in this study. One of the major challenges facing emulsion-based ATRP was very limited range of suitable surfactant. The latex stability was a real problem in controlled/living radical polymerization. Therefore, the choice of emulsifier became very essential.

Table 1. Results of the effects of surfactant types on latex nanospheres by ATRP

Emulsifier type	Conversion [%]	M_w/M_n	Diameter [nm]	Stability
SDS	8.43	4.31	–	unstable
OP-10	26.60	1.76	150	unstable
TW-80	97.75	1.44	120	stable

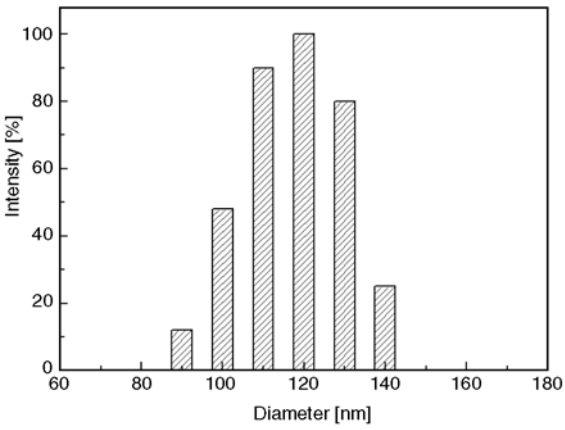

Figure 9. The size distribution of the PSt latex nanospheres produced by ATRP

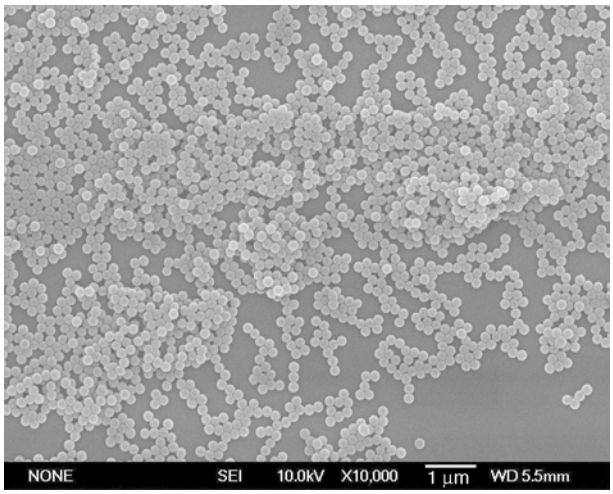

Figure 10. SEM of the PSt latex nanospheres produced by ATRP in emulsion system

Figure 9 shows the size distribution of polystyrene nanosphere by the method of emulsion ATRP with Tween 80 as surfactant. The polystyrene latex nanospheres obtained had a diameter of 120 nm with a narrow size distribution. The morphology of polymer latex nanosphere was observed by scaning electron microscopy (SEM), as shown in Figure 10. It appeared that the polystyrene latex nanosphere was uniform spherical with a diameter of about 120 nm. The most important predominance was that the polymer particle possessed a narrow molecular weight distribution. In other words, the obtained polymer nanospheres hold a symmetrical configuration and uniform size molecular weight. The material of latex nanosphere produced is very significant in drug targeting carrier systems, the target-selective delivery and release of loaded drugs and other many application fields.

4. Conclusions

The effect of different ligands including ethylenediamine, 1,10-phenanthroline (phen) and 4,4-dinonyl-2,2-bipyridyl (dNbpy) on the controlled polymerization of monodisperse polystyrene nanospheres was investigated. Using oil-soluble of ligand (dNbpy), the corresponding polydispersity of polystyrene was 1.44, but the conversion was at around 69%. The obtained polymer using ethylenediamine as ligand presented a broad molecular weight distribution (polydispersity index 1.78) but the polymerization rate was high and conversion reached to 96.8%. CuCl/ethylenediamine was highly soluble in water. The metal complexes were easily migrated to the aqueous phase and led to an uncontrolled polymerization reaction, whereas the polymerization rate with the CuCl/ethylenediamine system was faster than that with the CuCl/dNbpy or CuCl/phen system. The controllability of polymerization reaction depended on the solubility of metal complexes in organic phase, but the structure of ligand and the steric hindrance also played a key role in this system. With dNbpy or phen as ligands the steric hindrance around nitrogen atoms was remarkable. To a certain extent, large steric hindrance hindered the formation of living radical, at the same time the complex with CuCl was instable, which decreased the catalytic activity of the catalyst. Tween 80 presented the best results of latex nanosphere stability in the system. SEM showed the polystyrene latex nanospheres were uniform spherical with a diameter of about 120 nm. The material of latex nanosphere presented a significant potential in drug targeting carrier field.

Acknowledgements

The authors are grateful to the financial supports by the Natural Science Foundation of Hebei Province, China (E2007000629), Science and Technology Supported Item of Hebei Province, China (09215109D).

References

[1] Dai Q., Wu D., Zhang Z., Ye Q.: Preparation of monodisperse poly(methyl methacrylate) particles by radiation-induced dispersion polymerization using vinyl terminus polysiloxane macromonomer as a polymerizable stabilizer. Polymer, **44**, 73–77 (2003). DOI: 10.1016/S0032-3861(02)00728-0

[2] Song J-S., Winnik M. A.: Monodisperse, micrometer-sized low molar mass polystyrene particles by two-stage dispersion polymerization. Polymer, **47**, 4557–4563 (2006). DOI: 10.1016/j.polymer.2006.04.025

[3] Eslami H., Zhu S. P.: Emulsion atom transfer radical polymerization of 2-ethylhexyl methacrylate. Polymer, **46**, 5484–5493 (2005). DOI: 10.1016/j.polymer.2005.05.031

[4] Kurisawa M., Yokoyama M., Okano T.: Gene expression control by temperature with thermo-responsive polymeric gene carriers. Journal of Control Release, **69**, 127–137 (2000). DOI: 10.1016/S0168-3659(00)00297-2

[5] Hu B., Fuchs A., Huseyin S., Gordaninejad F., Evrensel C.: Atom transfer radical polymerized MR fluids. Polymer, **47**, 7653–7663 (2006). DOI: 10.1016/j.polymer.2006.08.069

[6] Ayres N., Boyes S. G., Brittain W. J.: Stimuli-responsive polyelectrolyte polymer brushes prepared via atom-transfer radical polymerization. Langmuir, **23**, 182–189 (2007). DOI: 10.1021/la061526l

[7] Su X., Feng Y., Wang B., Lu Z., Wei L.: Oligomeric cationic surfactants prepared from surfmers via ATRP: Synthesis and surface activities. Colloid and Polymer Science, **289**, 101–110 (2011). DOI: 10.1007/S00396-010-2331-6

[8] Gao Y., Li H., Wang X.: Synthesis and characterization of syndiotactic polystyrene-*graft*-poly(glycidyl methacrylate) copolymer by atom transfer radical polymerization. European Polymer Journal, **43**, 1258–1266 (2007). DOI: 10.1016/j.eurpolymj.2007.01.045

[9] Hansen N. M. L., Jankova K., Hvilsted S.: Fluoropolymer materials and architectures prepared by controlled radical polymerizations. European Polymer Journal, **43**, 255–672 (2007). DOI: 10.1016/j.eurpolymj.2006.11.016

[10] Jakubowski W., Matyjaszewski K.: New segmented copolymers by combination of atom transfer radical polymerization and ring opening polymerization. Macromolecular Symposia, **240**, 213–223 (2006). DOI: 10.1002/masy.200650826

[11] Lu J-M., Xu Q-F., Yuan X., Xia X-W., Zhai J-X., Wang L-H.: Synthesis, characterization, and fluorescence of end-functionalized polystyrene initiated by 4-chloromethyl benzoic acid and ethyl 4-chloromethyl benzenecarboxylate via ATRP. Journal of Applied Polymer Science, **104**, 75–80 (2007). DOI: 10.1002/app.25516

[12] Amin A., Sobh R., Ayoub M. M. H.: Three arm star homo- and block co-polymers via atom transfer radical polymerization. Journal of Macromolecular Science Part A: Pure and applied Chemistry, **43**, 667–677 (2006). DOI: 10.1080/10601320600602415

[13] Zhang X., Ai C., Ma J., Xu J., Yang S.: Synthesis of zwitterionic shell cross-linked micelles with pH-dependent hydrophilicity. Journal of Colloid and Interface Science, **356**, 24–30 (2011).
DOI: 10.1016/j.jcis.2010.12.041

[14] Dayananda K., Pi B. S., Kim B. S., Park T. G., Lee D. S.: Synthesis and characterization of pH/temperature-sensitive block copolymers via atom transfer radical polymerization. Polymer, **48**, 758–762 (2007).
DOI: 10.1016/j.polymer.2006.11.040

[15] Skrabania K., Kristen J., Laschewsky A., Akdemir Ö., Hoth A., Lutz J-F.: Design, synthesis, and aqueous aggregation behavior of nonionic single and multiple thermoresponsive polymers. Langmuir, **23**, 84–93 (2007).
DOI: 10.1021/la061509w

[16] Li Y., Lu G.: ARGET ATRP of methyl methacrylate with 2-(8-heptadecenyl)-4,5-dihydro-1H-imidazole-1-ethylamine (OLC) as both ligand and reducing agent in the presence of air. Colloid and Polymer Science, **288**, 1495–1500 (2010).
DOI: 10.1007/s00396-010-2285-8

[17] Chen J., Xiang J., Cai Z., Yong H., Wang H., Zhang L., Luo W., Min H.: Synthesis of hydrophobic polymer brushes on silica nanoparticles via the combination of surface-initiated ATRP, ROP and click chemistry. Journal of Macromolecular Science Part A: Pure and Applied Chemistry, **47**, 655–662 (2010).
DOI: 10.1080/10601325.2010.483357

[18] Oliveira J. M., Salgado A. J., Sousa N., Mano J. F., Reis R. L.: Dendrimers and derivatives as a potential therapeutic tool in regenerative medicine strategies – A review. Progress in Polymer Science, **35**, 1163–1194 (2010).
DOI: 10.1016/j.progpolymsci.2010.04.006

[19] Yokoyama R., Suzuki S., Shirai K., Yamauchi T., Tsubokawa N., Tsuchimochi M.: Preparation and properties of biocompatible polymer-grafted silica nanoparticle. European Polymer Journal, **42**, 3221–3229 (2006).
DOI: 10.1016/j.eurpolymj.2006.08.015

[20] Wang J-S., Matyjaszewski K.: Controlled/'living' radical polymerization. Halogen atom transfer radical polymerization promoted by a Cu(I)/Cu(II) redox process. Macromolecules, **28**, 7901–7910 (1995).
DOI: 10.1021/ma00127a042

[21] Matyjaszewski K., Patten T. E., Xia J. H.: Controlled/'living' radical polymerization. Kinetics of the homogeneous atom transfer radical polymerization of styrene. Journal of American Chemical Society, **119**, 674–680 (1997).
DOI: 10.1021/ja963361g

[22] Braunecker W., Matyjaszewski K.: Controlled/'living' radical polymerization: Features, developments, and perspectives. Progress in Polymer Science, **32**, 93–146 (2007).
DOI: 10.1016/j.progpolymsci.2006.11.002

[23] Grimaud T., Matyjaszewski K.: Controlled/'living' radical polymerization of methyl methacrylate by atom transfer radical polymerization. Macromolecules, **30**, 2216–2218 (1997).
DOI: 10.1021/ma961796i

[24] Rutnakornpituk M., Puangsin N., Theamdee P., Rutnakornpituk B., Wichai U.: Poly(acrylic acid)-grafted magnetic nanoparticle for conjugation with folic acid. Polymer, **52**, 987–995 (2011).
DOI: 10.1016/j.polymer.2010.12.059

[25] Li D., He Q., Cui Y., Wang K., Zhang X., Li J.: Thermosensitive copolymer networks modify gold nanoparticles for nanocomposite entrapment. Chemistry-A European Journal, **13**, 2224–2229 (2007).
DOI: 10.1002/chem.200600839

[26] Uegaki H., Kotani Y., Kamigaito M., Sawamoto M.: Nickel-mediated living radical polymerization of methyl methacrylate. Macromolecules, **30**, 2249–2253 (1997).
DOI: 10.1021/ma961367k

[27] Oh J. K., Bencherif S. A., Matyjaszewski K.: Atom transfer radical polymerization in inverse miniemulsion: A versatile route toward preparation and functionalization of microgels/nanogels for targeted drug delivery applications. Polymer, **50**, 4407–4423 (2009).
DOI: 10.1016/j.polymer.2009.06.045

[28] Ajioka N., Yokoyama A., Yokozawa T.: Synthesis of well-defined rod-coil diblock copolymer of aromatic polyether and polyacrylonitrile by chain-growth condensation polymerization and atom transfer radical polymerization. Macromolecular Rapid Communication, **29**, 665–671 (2008).
DOI: 10.1002/marc.200700862

[29] Huang Z., Zhang Y., Li H., Liu Y.: A novel immobilized cobalt(II)/copper(II) bimetallic catalyst for atom transfer radical polymerization (ATRP) of methyl methacrylate. Applied Catalysis A: General, **332**, 192–199 (2007).
DOI: 10.1016/j.apcata.2007.07.040

[30] Tang E., Dong S.: Preparation of styrene polymer/ZnO nanocomposite latex via miniemulsion polymerization and its antibacterial property. Colloid and Polymer Science, **287**, 1025–1032 (2009).
DOI: 10.1007/s00396-009-2057-5

[31] Bajpai A. K., Shukla S. K., Bhanu S., Kankane S.: Responsive polymers in controlled drug delivery. Progress in Polymer Science, **33**, 1088–1118 (2008).
DOI: 10.1016/j.progpolymsci.2008.07.005

[32] Qiu J., Gaynor S. G., Matyjaszewski K.: Emulsion polymerization of *n*-butyl methacrylate by reverse atom transfer radical polymerization. Macromolecules, **32**, 2872–2875 (1999).
DOI: 10.1021/ma981695f

[33] Coca S., Jasieczek C. B., Beers K. L., Matyjaszewski K.: Polymerization of acrylates by atom transfer radical polymerization. Homopolymerization of 2-hydroxyethyl acrylate. Journal of Polymer Science Part A: Polymer Chemistry, **36**, 1417–1424 (1998).
DOI: 10.1002/(SICI)1099-0518(19980715)36:9<1417::AID-POLA9>3.0.CO;2-P

[34] Pyun J., Jia S., Kowalewski T., Patterson G. D., Matyjaszewski K.: Synthesis and characterization of organic/inorganic hybrid nanoparticles: Kinetics of surface-initiated atom transfer radical polymerization and morphology of hybrid nanoparticle ultrathin films. Macromolecules, **36**, 5094–5104 (2003).
DOI: 10.1021/ma034188t

[35] Qiu J., Charleux B., Matyjaszewski K.: Controlled/living radical polymerization in aqueous media: Homogeneous and heterogeneous systems. Progress in Polymer Science, **26**, 2083–2134 (2001).
DOI: 10.1016/S0079-6700(01)00033-8

[36] Asua J. M.: Miniemulsion polymerization. Progress in Polymer Science, **27**, 1283–1346 (2002).
DOI: 10.1016/S0079-6700(02)00010-2

eXPRESS Polymer Letters Vol.6, No.10 (2012) 847–858
Available online at www.expresspolymlett.com
DOI: 10.3144/expresspolymlett.2012.90

Improved properties of chemically modified graphene/poly(methyl methacrylate) nanocomposites *via* a facile *in-situ* bulk polymerization

X. Y. Yuan[*], *L. L. Zou, C. C. Liao, J. W. Dai*

College of Science, Chongqing Jiaotong University, 400074 Chongqing, China

Received 16 March 2012; accepted in revised form 17 May 2012

Abstract. The nanosheet of graphene was chemically modified by long alkyl chain for enhanced compatibility with polymer matrix and graphene/poly(methyl methacrylate) (PMMA) nanocomposites with homogeneous dispersion of the nanosheets and enhanced nanofiller-matrix interfacial interaction were fabricated via a facile in-situ bulk polymerization. The nanocomposites were characterized by X-ray diffraction, Fourier transform infrared spectroscopy, Scanning electron microscopy and thermogravimetry. The results showed that the graphene nanosheets were fully exfoliated in PMMA matrix and the thermal and mechanical properties of the nanocomposites were significantly improved at low graphene loadings. Large shifts of 15°C in the glass transition temperature and 27°C improvement of onset thermal degradation temperature were achieved with graphene loading as low as 0.07 wt%. A 67% increase in tensile strength was also observed by the addition of only 0.5 wt% graphene. The method used in this study provided a novel route to other graphene-based polymers.

Keywords: *nanocomposites, graphene, poly(methyl methacrylate), mechanical property, thermal property*

1. Introduction

Graphene, a two-dimensional layer of sp^2-bonded carbon atoms densely packed in a honeycomb crystal lattice, has attracted significant interests due to its exceptional mechanical, electrical, thermal and optical properties [1–6] and is being explored for use in a variety of applications such as electronics [7], composites [8, 9], catalysis sensors [10], transparent and flexible electrodes [11], solar cells and supercapacitor [12]. Among these potential applications, the use of graphene as one of promising nanofillers incorporating in a polymer matrix has been extensively investigated to develop cost-effective, high-performance graphene-polymer nancomposites (GPN) [13–15]. Recent studies have shown that polymer nanocomposites with graphene as nanofiller exhibit substantial property enhancements at much lower loadings than with other conventional nanofiller in many cases [13–16].

To achieve high-performance of GPNs, however, homogeneous dispersion of graphene nanosheets in the polymer hosts and proper interfacial interactions between the nanosheets and the surrounding matrix must be considered. The nature of graphene is not compatible with the organic polymer matrix and the individual sheets tend to restack owing to their large specific surface area and van der Waals interactions between the interlayers of graphene nanosheets, which lowers its effectiveness as a nanofiller for property improvements [6, 17]. An effective way to overcome the agglomeration and enhance the compatibility between graphene nanosheets and polymer matrix is the surface modification of graphene via noncovalent and covalent interaction [14].

[*]Corresponding author, e-mail: yuanxy@cquc.edu.cn

Graphene oxide (GO), an important intermediate for preparing graphene via chemical reduction [18], consists of many oxygen-containing groups, such as hydroxyl, epoxy, carbonyl and carboxyl groups, which provide diverse active sites for covalent funcationalizations [17, 19]. Therefore, chemical interaction via direct coupling between polymers and the surface groups bound on GO sheets [20–26] and grafting some molecules including monomer [27] and atom transfer radical polymerization (ATRP) initiator [28–33] prior to polymerization could be accomplished. Pan *et al*. [25] prepared covalently functionalized graphene sheets by grafting a well defined thermo-responsive poly(N-isopropylacrylamide) via click chemistry and the nanocomposites exhibited a hydrophilic to hydrophobic phase transition at 33°C and a superior anticancer drug loading capacity of 15.6 wt%. Fang *et al*. [30] covalently grafted an ATRP initiator onto the graphene sheet via a diazonium addition and the resulting polystyrene nanocomposites showed around 70 and 57% increases in tensile strength and Young's modulus with 0.9 wt% graphene nanosheets, respectively. By reacting Gamma-aminopropyltriethoxysilane-grafted graphene oxide sheets and maleic anhydride grafted polyethylene, Fang *et al*. [33] recently demonstrated a covalently bonded polyethylene grafted graphene oxide hybrid material with about 20% increase in Young's modulus at 0.3 wt% of graphene oxide and about 15% increase in yielding strength and tensile strength with only 0.1 wt% of graphene oxide were achieved. Chemical linkage between graphene nanosheets and polymer matrix could indeed enhance the interfacial adhesion, which favored the load transfer across the interface of the nanocomposites. However, current methods available for enhanced interfacial compatibility via covalent functionalization of graphene nanosheets with the polymer suffer from certain drawbacks, including tedious processes, rigorous reaction conditions, lack of precise control of polymer architecture and nanofiller content.

Compared to these aforementioned methods, noncovalent interaction between the nanofiller and polymer matrix via hydrogen bonding and π-π stacking is more easily achieved by solution blending [34–37], self assembly [38–40] and *in situ* interactive polymerization [41–44]. Liang *et al*. [34] demonstrated that molecular-level dispersion of graphene into poly(vinyl alcohol) by solution-mixing and the hydrogen bonding at the interface were key to 76% increase in tensile strength and 62% improvement of Young's modulus of the nanocomposites at only 0.7 wt% of GO Liu *et al*. [40] synthesized pH-sensitive GPNs by attaching pyrene-terminated poly(2-N,N-(dimethyl amino ethyl acrylate) and poly (acrylic acid) onto the basal plane of graphene sheets via π-π stacking, respectively. Precipitation/extraction or solution casting to generate samples often coincide with these efforts, which causes an additional tedious work-up for purification. Therefore, it is very urgent to explore a facile and efficient method to compatibilize graphene sheets with the polymer hosts in GPNs while maintaining good dispersion of the nanosheets in the matrix.

In situ polymerization is an effective way to prepare layered-structure nanocomposite [45] and has been used to produce non-covalent graphene-based nanocomposites. Potts *et al*. [41] prepared chemically reduced graphene/poly(methyl methacrylate) (PMMA) by free radical solution-polymerization of methyl methacrylate (MMA) in the presence of exfoliated GO and an shift of over 15°C in the glass transition temperature with graphene loadings as low as 0.05 wt% and 28% increase of the elastic modulus at just 1 wt% loading were observed. To date, however, most of *in situ* polymerization techniques used for GPNs are focused on solution polymerization [41–44] and involve an intercalation of functionalized GO with a monomer prior to polymerization, where subsequent coagulation of polymer or reduction of GO are frequently involved. In addition, the tedious purification of GPNs by coagulation with non-solvent of the matrix polymer can potentially lead to aggregation of the nanofiller in the composites [46], which could worsen the properties of the resulting GPNs. Motivated by these results, in this work, we sought to explore a facile and efficient route for producing graphene/PMMA nanocomposites via *in situ* bulk-polymerization of MMA in the presence of Octadecylamine-modified graphene (C_{18}-graphene). The long-alkyl chain attached onto the edges of graphene favored homogeneous dispersion of graphene nanosheets in the matrix and good compatibility between graphene and PMMA. The obtained C_{18}-graphene/PMMA nanocomposites exhibited significant enhancement in mechanical properties and thermal stability at

very low loadings of graphene and the results are herein disclosed.

2. Experimental

2.1. Materials

Natural graphite flakes with an average particle size of 150 μm and a purity of >98% were supplied from Qingdao Nanshu Graphite Co., Ltd., China. Concentrated sulfuric acid (A.R., 98%), hydrochloric acid (A.R., 36%), Hydrogen peroxide (A.R., 30%), Sodium nitrate (A.R.), N, N-dimethylformamide (DMF, A.R.) and ethanol (A.R.), were purchased from Chongqing Chuandong Chemical Reagent Factory, China. Potassium permanganate (A.R.) was purchased from Yixin Chemical Reagent Co., Ltd., China. Hydrazine hydrate (A.R., 85%), Octadecylamine(A.R., ODA) and N, N-dicyclohexylcarbodiimide (DCC, A.R.) were provided from Sinopharm Chemical Reagent Co., Ltd., China. Methylmethacrylate (A.R.) and benzoyl peroxide (BPO, A.R.) were obtained from Kelong Chemical Reagent Factory, China and purified by distillation under reduced pressure. All the reagents were used as received without any further treatment.

2.2. Preparation of graphene oxide (GO)

GO was prepared according to the Hummers method [47]. Graphite (1.0 g), sodium nitrate (1.0 g) and concentrated H_2SO_4 (23 mL) were mixed and cooled to 0°C. $KMnO_4$ (3.0 g) was slowly added while stirring and the rate of addition was controlled to prevent the mixture temperature from exceeding 20°C. After the complete addition of $KMnO_4$, the mixture was then transferred to a 35°C water bath and stirred for 30 min, during which a brownish-gray paste was formed. Next, 50 mL of deionized water was added to the solution, and the temperature was increased to 98°C. After 15 min, the solution was further treated with 100 mL of warm water and 10 mL of 30% H_2O_2. The light-yellow warm solution was then filtered and the precipitate was washed with deionized water several times, and finally dried at 60°C under vacuum.

2.3. Preparation of octadecylamine-modified graphene(C_{18}-graphene)

Starting from GO, chemically reduced graphene (CRG) was prepared according to Ruoff's method [48, 49]. For surface modification of CRG with long alkyl chain, 0.15 g of graphene was dispersed in 200 mL anhydrous DMF by 1 h of ulstrasonication (As2060B bath sonicator, Automatic Science Instrument Co. Ltd., China). 5.0 g of ODA and 2.0 g of DCC were then added and the mixture was stirred at 90°C under N_2 for 48 h. After filtration of the solution, the resulting solid was washed with excess ethanol and dried under vacuum.

2.4. Preparation of octadecylamine-modified graphene/PMMA nanocomposites (C_{18}-graphene/PMMA)

The original loading of C_{18}-graphene was based on the weight of MMA monomer and C_{18}-graphene/PMMA nanocomposites were prepared *via in situ* bulk-polymerization. Typically, 0.02 g (0.1 wt% of MMA) of C_{18}-graphene was added into 20.0 g of MMA and the mixture was treated with ultrasound at 0°C for 1 h. The obtained black dispersion was then subjected to 15 min of centrifugation at 4000 rpm to remove any unexfoliated agglomerate. The obtained C_{18}-graphene/MMA suspension was purged with dry nitrogen for 10 min to remove traces of oxygen from the solution and 0.3 g of BPO was then added. Subsequently, the temperature was raised to 60°C to promote polymerization. The reaction was maintained at 60°C for 8 h until the mixture turned into transparent solid. A similar protocol was followed to prepare pure PMMA and C_{18}-graphene/PMMA composites with original graphene loading of 0.1, 0.5, 1.0 and 1.5 wt%, respectively. For clarity of discussion, the prepared PMMA nanocomposites with original graphene loading of 0.1, 0.5, 1.0 and 1.5 wt% were labeled as C_{18}-graphene-0.1/PMMA, C_{18}-graphene-0.5/PMMA, C_{18}-graphene-1.0 /PMMA and C_{18}-graphene-1.5/PMMA, respectively. The intrinsic loadings of graphene in these nanocomposites were measured by TGA analysis as discussed in Part 3.3.

2.5. Characterization

Fourier Transform Infrared Spectroscopy (FTIR)

A Nicolet 6700 Fourier transform infrared spectrometer (Thermo Fisher Scientific, USA) was used for FTIR analysis. FTIR was measured on with scanning from 400 to 4000 cm^{-1} by using KBr disks.

High resolution Transmission Electron Microcopy (HRTEM)
HRTEM was conducted on JEOL JEM -2100 electron microscope (Japan) at an acceleration voltage of 200 kV. The sample for HRTEM analysis was prepared by depositing an aliquot of the sample suspension onto a carbon grid and then the solvent was allowed to evaporate.

Scanning Electron Microscopy (SEM)
The fracture surface of the nanocomposites was observed by FEINova 400 SEM (FEI, Netherlands) with acceleration voltage of 20.0 kV. Samples were prepared by immersing the films in liquid nitrogen for 10 min before fracture. The fracture surfaces were coated with gold before analysis.

X-ray Diffraction (XRD)
XRD measurements were carried out using a Rigaku D/Max-2500 diffractometer (Rigaku, Japan) with Cu-Kα radiation.

Gel Permeation Chromatograph (GPC)
GPC measurements were determined using a Waters gel permeation chromatograph (USA) equipped with a Waters 1515 Isocratic HPLC pump, Waters 717 plus Autosampler, three Waters Styragel® HT4 columns collected in series and Waters 2414 Refractive Index Detector refractive index detector. All samples were analyzed at room temperature with tetrahydrofuran as the eluent at the flow rate of 1.0 mL/min.

Differential Scanning Calorimetry (DSC)
The glass transition temperature (T_g) was evaluated by using DSC method. DSC measurements were conducted on TA Q200 (TA, USA) with an approximately 5 mg of each sample in an atmosphere of nitrogen. The samples were tested from –40°Cand then heated to 220°C at a heating rate of 10°C/min, kept for 5 min to eliminate the thermal history, then cooled to –40°C at a cooling rate of 10°C/min. The DSC data reported were taken from the second scan and T_g were calculated.

Thermogravimetric Analysis (TGA)
TGA and the derivative of TG curves (DTG) were performed with Netzsch STA 449C thermogravimetric analyzer (Germany) under nitrogen atmosphere at a heating rate of 10°C/min and approximately 10 mg of each sample were measured under N_2.

Mechanical properties
The mechanical properties of graphene/PMMA nanocomposites were measured by a universal tensile testing machine (Sans Co. Ltd., China) at room temperature according to ASTM D882-2009. The samples used for mechanical test were prepared by injection molding and conducted with a crosshead speed of 5mm/min. In all cases, more than five samples were tested and standard deviations were calculated.

3. Results and discussion

3.1. Preparation of C_{18}-graphene and its dispersion in MMA

It is widely known that the maximum improvements in final properties of GPNs can only be achieved when graphene is homogeneously dispersed in the matrix and the external load is efficiently transferred through strong filler/polymer interfacial interaction [13–15]. Thus, how to chemically modify the surface of graphene and design facile preparation route may be essential to generate GPNs with enhanced reinforcement efficiency of graphene. The acylation reaction is one of the most common approaches used for linking molecular moieties onto oxygenated groups alongside the graphene nanosheets [4]. Even if strong reducing reagents are used in chemical deoxygenation of GO and most of oxygen-containing functional groups are removed from the graphene surface, some residual functional groups such as carboxylic and hydroxyl group remain within the graphene sheets, which facilitates further covalent functionalization opening plenty of opportunities for the preparation of GPNs [17, 22, 50]. In this work, chemically reduced graphene (CRG) was anchored by long alkyl chain via an amidation reaction to enhance the compatibility between the nanosheets and polymer matrix. The amidation reaction was achieved by the DCC-activated coupling reaction between carboxylic moieties on the CRG nanosheets and the amine group of ODA molecule, which was confirmed by FTIR. As presented in Figure 1a, there were some characteristic absorptions of graphene around 1580 cm^{-1}, attributed to C=C vibrations of graphene sheets. Moreover, a tiny absorption peak at 1730 cm^{-1} assigned to the

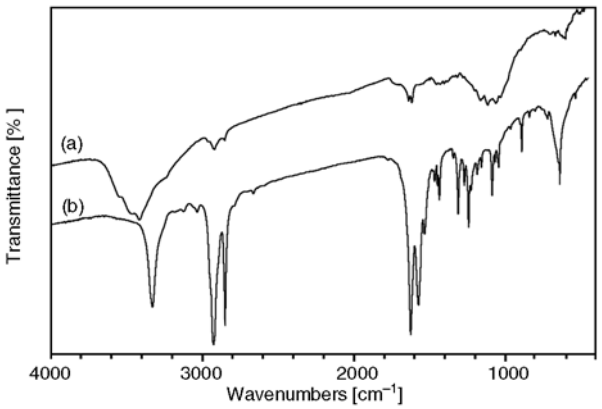

Figure 1. FTIR spectra of CRG (a) and C_{18}-graphene (b)

C=O situated at edges of CRG sheets was also identified. After the reaction with ODA, however, the peak of C=O became weaker and new bands around 3300 and 1640 cm^{-1} due to the formation of amide were observed (Figure 1b). Besides, the absorption peak at 2920 and 2850 (C–H stretch of alkyl chain), 1530 cm^{-1} (N–H bending of amide) also appeared in the spectrum of C_{18}-graphene. These results confirmed the success of the amidation reaction.

Grafting of long alkyl chain on the nanosheets imparted the functionalized C_{18}-graphene organophilic and was expected to have enhanced solubility in vavious organic medium [48–53]. As shown in Figure 2a, after removal of any unexfoliated agglomerate by ultrasonication and centrifugation, the functionalized C_{18}-graphene was homogenously dispersed in MMA solution. Compared to pure MMA, where the solution was almost clear, the MMA solution containing C_{18}-graphene was blacker, indicating that C_{18}-graphene was more soluble in MMA. Moreover, the blacker MMA solution was very stable and no sedimentation was observed for at least four weeks. To evaluate the degree of exfoliation of organophilic C_{18}-graphene into individual nanosheets in the MMA system, a suspension prepared from original loading of 0.5 wt% of C_{18}-graphene was examined by High resolution Transmission Electron Microcopy (HRTEM). As seen from Figures 2b and 2c, although some monolayer nanosheets could be detected on the substrate, large quantities of few-layers smooth graphene (<10 layers) with no significant folding or overlapping were obviously identified, showing that the long alkyl chain present on the sides of the sheets could effectively prevent the restacking of the nanosheets and good dispersibility was achieved in MMA solution.

3.2. Preparation and microstructure of C_{18}-graphene/PMMA nanocomposites

Bulk polymerization is ready to prepare PMMA with high molecular weight. After polymerization, the resulting C_{18}-graphene/PMMA nanocomposites darkened to a uniform black as the C_{18}-graphene content increased, contrary to colorless pure PMMA. It has been shown that gelation time was affected by some nanofillers in radical bulk polymerization of MMA and subsequent molecular weight and molecular weight distribution of the nanocomposites were different from those obtained from bulk polymerization of pure MMA [54, 55].

In order to investigate whether similar phenomenon occurred in our research, the molecular weight and polydispersity index of the neat PMMA and C_{18}-graphene/PMMA nanocomposites with various graphene contents were examined by gel perme-

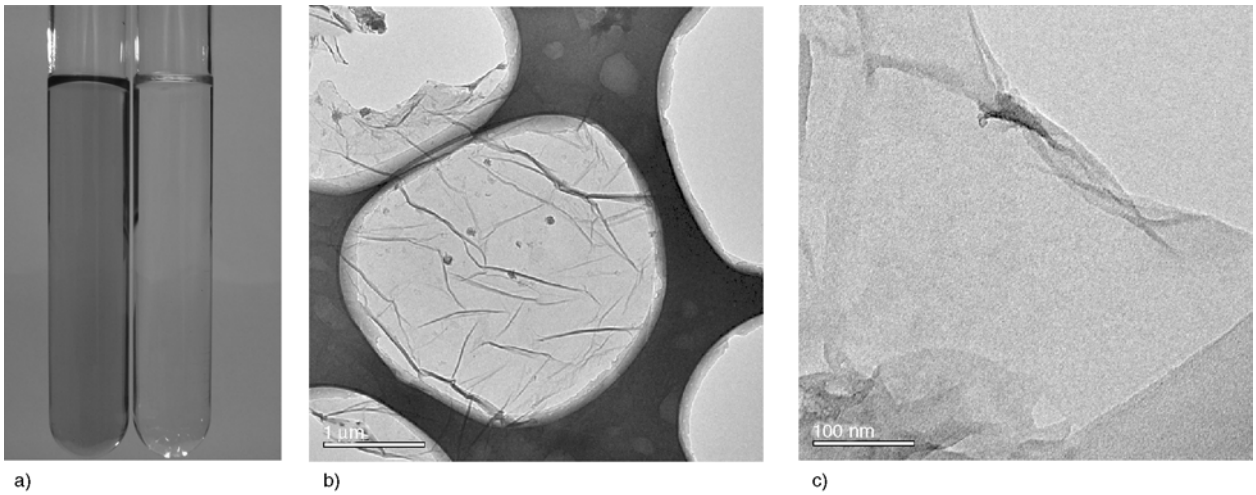

Figure 2. (a) Morphological image of MMA solution containing C_{18}-graphene (left) and pure MMA (right); (b) and (c) HRTEM images of C_{18}-graphene nanosheets in MMA solution of original loading of 0.5 wt%

Table 1. Results of GPC analysis for neat PMMA and C_{18}-graphene/PMMA nanocomposites with various graphene contents

Sample	$M_w(\cdot 10^5)$ [g/mol]	M_w/M_n [–]
Neat PMMA	2.83	5.25
C_{18}-graphene-0.1/PMMA	3.01	6.53
C_{18}-graphene-0.5/PMMA	2.94	5.31
C_{18}-graphene-1.0/PMMA	3.29	5.94
C_{18}-graphene-1.5/PMMA	3.46	6.11

ation chromatograph (GPC). Prior to molecular weight measurement, free PMMA was separated from C_{18}-graphene/PMMA nanocomposites by Soxhlet extraction with boiling acetone for 48 h, precipitated in methanol, and finally dried in vacuum at 60°C for 48 h. The results of GPC analysis are summarized in Table 1. It could be obviously that PMMA in these composites had higher molecular weight than their neat counterpart and the molecular weight increased slightly as the original loading of C_{18}-graphene increased. This maybe attributed to the participation of modified graphene nanosheets in the polymerization reaction and the additional consumption of radicals captured by the graphene surface, which was similar to the case where carbon nanotube was used as the nanofiller [54]. In fact, the polymer chains of PMMA nanocomposites measured in GPC were not directly attached to graphene surface because these nanofiller were filtered out prior to the GPC measurements. But this kind of end-tethered PMMA on graphene surface could affect some properties of the resulting GPNs.

The homogeneous dispersion of the nanosheets in the matrix is very crucial to improve the final properties of the GPNs. Li *et al*. [56] recently reported that simultaneous surface functionalization and reduction of GO was achieved by simple refluxing of GO with octadecylamine (ODA) without the use of any reducing agents and the ODA-modified graphene nanosheets could impove the nanofiller dispersion and thus the conductivity of polymer nanocomposites. To well-disperse the graphene sheets into the polymer, in this study, the as-prepared organophilic C_{18}-graphene was exfoliated into MMA solution via ultrasonication to form a stable colloid and C_{18}-graphene/PMMA nanocomposites were readily obtained by subsequent facile radical-bulk polymerization. To observe the dispersion of graphene in these nanocomposites, X-ray

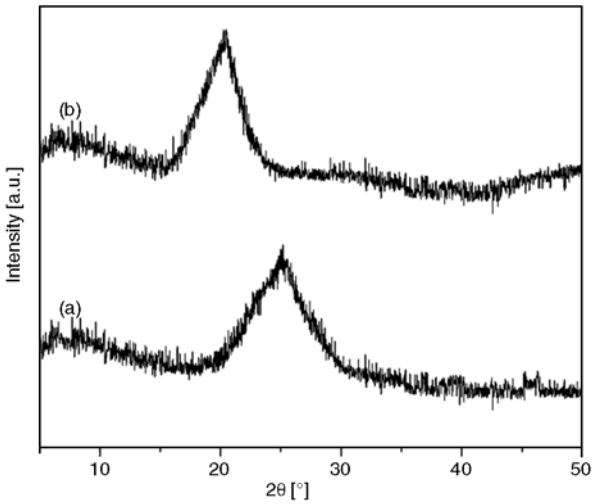

Figure 3. XRD patterns of CRG (a) and C_{18}-graphene (b)

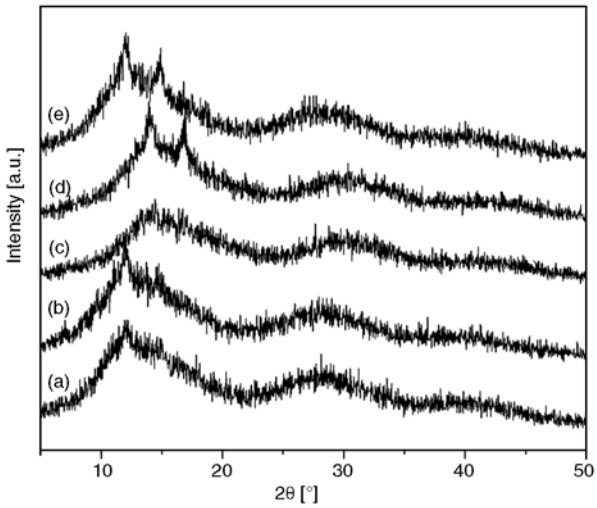

Figure 4. XRD patterns of (a) PMMA and C_{18}-graphene/PMMA nanocomposites, (b) C_{18}-graphene-0.1/PMMA, (c) C_{18}-graphene-0.5/PMMA, (d) C_{18}-graphene-1.0/PMMA and (e) C_{18}-graphene-1.5/PMMA

Diffraction (XRD) and Scanning Electron Microscopy (SEM) were employed to probe the morphology and nanostructure of these products. Figures 3 and 4 show the XRD patterns of the CRG, C_{18}-graphene and PMMA nanocomposites with different loading of C_{18}-graphene, respectively. The CRG nanosheets showed a (002) diffraction peak at $2\theta = 25^{\circ}$ (Figure 3a), which corresponded to a *d*-spacing of 0.35 nm slightly larger than that of pristine graphite (0.34 nm, JCPDS No. 75-1621). Upon functionalizing with ODA, the strongest diffraction peak of the C_{18}-graphene shifted to a smaller $2\theta = 21^{\circ}$ (Figure 3b), corresponding to a *d*-spacing of 0.41 nm, which indicated that attachment of long alkyl chain along the edges of the nanosheets

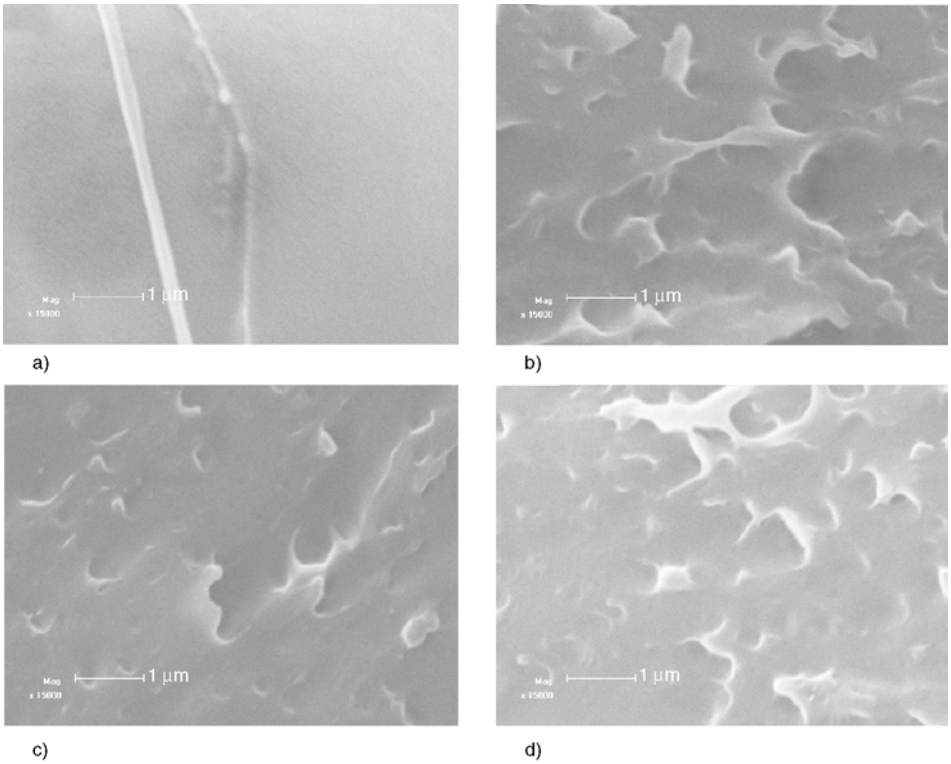

Figure 5. SEM image of cross-section fractured surface of C_{18}-graphene/PMMA nanocomposites. (a) C_{18}-graphene-0.1/PMMA, (b) C_{18}-graphene-0.5/PMMA, (c) C_{18}-graphene-1.0/PMMA and (d) C_{18}-graphene-1.5/PMMA.

enlarged the interlayer of C_{18}-graphene and thus would favor the intercalation of monomer and subsequent bulk polymerization within the gallery. For PMMA and C_{18}-graphene/ PMMA nanocomposites, pure PMMA showed a (002) diffraction peak at $2\theta \approx$ 12 and 30º (Figure 4a). However, as dispersing the functional C_{18}-graphene nanosheets into the PMMA matrix, the peak of C_{18}-graphene around 21º (Figure 3b) disappeared in the nanocomposites and only diffraction peaks around 12 and 30º arisen from PMMA were detected (Figure 4b~d), suggesting that penetration of PMMA chains into inter-layers of graphene were achieved [57], which was furthered confirmed by SEM. Figure 5 shows the cross-section SEM images of the fractured surface of C_{18}-graphene/PMMA nanocomposites. As can be seen from Figure 5, the graphene nanosheets were randomly dispersed in the matrix, especially in the case of lower loadings, showing typical characteristics of good compatibility between the nanosheets and polymer matrix. From Figure 5d, there was clear and irregular entanglement of nanosheets in higher graphene content. Meanwhile, the wrinkled and crumpled profile of the functional nanofiller in the nanocomposites was also detected, which could be largely attributed to strong covalent interaction between graphene nanosheet and PMMA matrix. This phenomenon was also mentioned elsewhere [44, 58, 59] and should contribute to enhance the final properties of graphene/PMMA nanocomposites.

3.3. Thermal and mechanical properties of graphene/PMMA nanocomposites

It is expected that thermal and mechanical properties of the as-prepared C_{18}-graphene/PMMA nanocomposites can be significantly enhanced, largely by the large interfacial area and high aspect ratio of the nanosheet, the homogeneous dispersion of the graphene sheets in the matrix and strong adhesion between graphene and the matrix. Figure 6 displays TGA and corresponding differential thermogravimetric (DTG) thermograms for neat PMMA and its nanocomposites with different graphene loadings under nitrogen atmosphere. The onset temperature of decomposition (T_d) can be considered as the temperature at the 5% weight loss. The relative thermal stability of the samples is evaluated by T_d and the temperature of the maximum degradation rate (T_{max}) obtained from DTG. These data, providing the information on the thermal degradation behavior, are also listed in Table 2. Both virgin PMMA

Table 2. Thermal data of PMMA and C_{18}-graphene/PMMA nanocomposites under nitrogen atmosphere

Sample	T_d[a] [°C]	T_{max}[b] [°C]	Calculated loading[c]	T_g [°C]
PMMA	249	369	–[d]	107
C_{18}-graphene-0.1/PMMA	276	372	0.07%	122
C_{18}-graphene-0.5/PMMA	256	370	0.21%	121
C_{18}-graphene-1.0/PMMA	273	367	0.28%	–[d]
C_{18}-graphene-1.5/PMMA	281	371	0.50%	122

[a]T_d:the degradation temperature at the 5% weight loss in the decomposition stage
[b]T_{max}: the maximum degradation temperature in the decomposition stage
[c]The value calculated from the residue at 480°C in TGA thermogram of C_{18}-graphene/PMMA nanocomposites
[d]not determined

and its nanocomposites exhibited similar weight loss curve profile with one-step threshold in their thermograms. With an onset of thermal degradation at ca. 249°C, pure PMMA showed mass loss between 300 and 400°C and almost no residue left behind above 480°C. Compared to that of pure PMMA, the TGA curves of C_{18}-graphene/PMMA nanocomposites were shifted toward higher temperature and all the T_d temperatures of these nanocomposites were significantly enhanced with low graphene loadings. For example, T_d values were raised from 249°C for virgin PMMA to 276°C for C_{18}-graphene-0.1/PMMA, 256°C for C_{18}-graphene-0.5/PMMA, 273°C for C_{18}-graphene-1.0/PMMA and 281°C for C_{18}-graphene-1.5/PMMA. Assuming that graphene was very stable against heat and the weight loss that occurred during thermal decomposition of these PMMA nanocomposites in higher temperature (~500°C) was entirely due to the removal of PMMA entity [30], the residue weight implied the intrinsic loading of graphene in these products, which was also presented in Table 2. With regard to the intrinsic loadings of C_{18}-graphene measured by TGA, therefore, dramatic improvement of thermal stability was achieved with very low loading of graphene in this study. From Table 2, only addition of measured loading of 0.07 wt% graphene afforded 27°C increment in T_d of C_{18}-graphene/PMMA nanocomposites. The reason was presumably that the homogeneously distributed CMG nanosheets could avoid heat concentration upon external thermal exposure and strong interaction between PMMA matrix and chemically modified graphene was introduced via in-situ bulk polymerization [34, 37, 41]. However, further increasing the graphene loading did not result

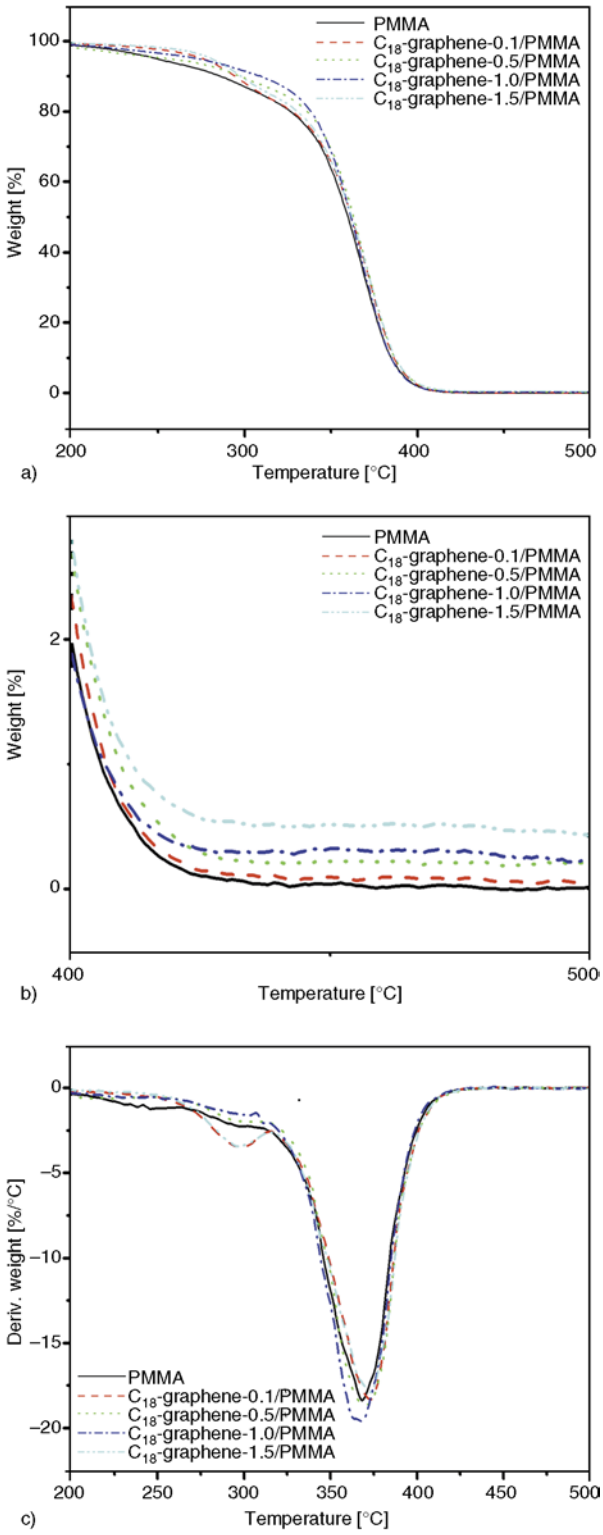

Figure 6. (a) TGA and (b) TGA in the range of 400–500°C, and (c) DTG thermograms for PMMA and C_{18}-graphene/PMMA nanocomposites in nitrogen atmosphere

in considerable enhancement of T_d. The T_{max} value was not also affected by the addition of the function-

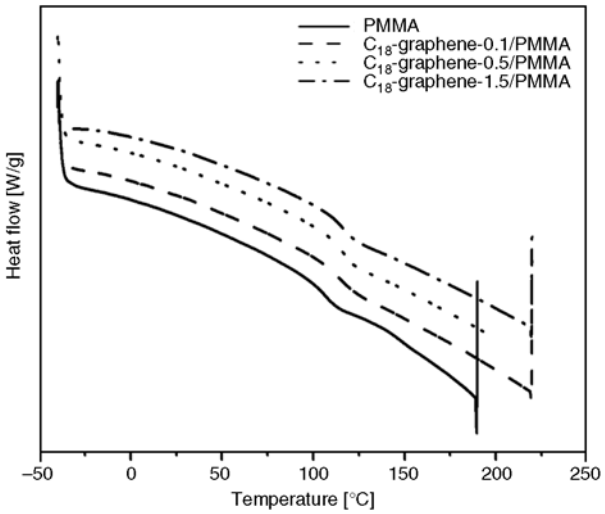

Figure 7. DSC thermograms for PMMA and C_{18}-graphene/PMMA nanocomposites

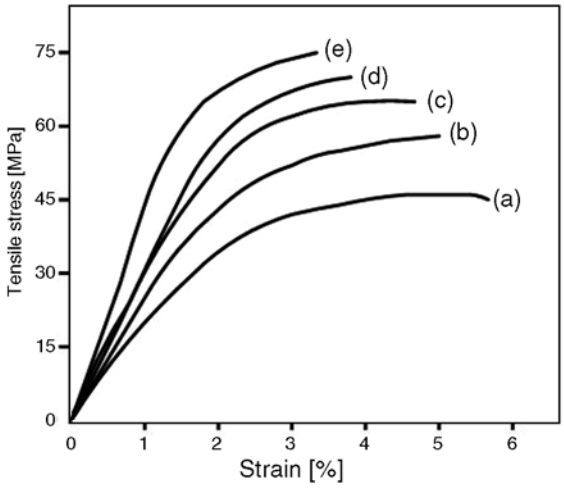

Figure 8. Typical stress-strain curves for (a) pure PMMA and C_{18}-graphene/PMMA nanocomposites, (b) C_{18}-graphene-0.1/PMMA, (c) C_{18}-graphene-0.5/ PMMA, (d) C_{18}-graphene-1.0/PMMA and (e) C_{18}-graphene-1.5/PMMA

alized graphene, showing that the nanofiller did not alter the thermal degradation mechanism.

Figure 7 discloses the DSC thermogram for PMMA and C_{18}-graphene/PMMA nanocomposites and the glass transition temperature (T_g) is obtained as listed in Table 2. T_g is a macroscopic indication of the segmental relaxation behavior of nanocomposite systems, strongly dependent on embedded nanoparticls. Compared to that of PMMA, C_{18}-graphene/PMMA nanocomposites showed 15°C increase in T_g at an intrinsic loading as low as 0.07 wt% and little increment was exhibited beyond this loading. Generally, T_g is highly molecular weight dependent, especially below the critical molecular weight of polymer. With regard to the same preparation condition and little difference in molecular weight for all samples in this case, however, the observed increase in T_g could not result largely from the molecular weight of PMMA. Therefore, the substantial enhancement in the T_g of these nanocomposites was attributed to the restriction in chain mobility due to confinement effect of 2D-layered graphene incorporated into the matrix and strong nanofiller-polymer interaction, which was similar to other reports elsewhere [27, 44].

As an important petrochemical polymer used in various fields, it is of much concern about mechanical property of PMMA composites. Figure 8 shows the typical stress-strain curves for pure PMMA and its nanocomposites with different graphene loadings. Taking the intrinsic loading of the nanofiller in these nanocomposites into account, it was obvious that low loading of graphene into the polymer matrix had a significant influence on the mechanical behavior and the tensile strength of C_{18}-graphene/PMMA nanocomposites with low graphene loading was dramatically enhanced as compared to that of pure PMMA matrix. For example, with intrinsic graphene loading of only 0.5 wt% for C_{18}-graphene-1.5/PMMA (the intrinsic loading of the nanocomposites is listed in Table 2), the tensile strength increased from 45 MPa of pure PMMMA to 75 MPa and the increase was 67%. The increasing trend was especially clear with lower loading. For example, the 0.07 wt% intrinsic loading of graphene increased the tensile strength up to 57 MPa and the tensile strength changed slightly without a pronounced threshold while further raising graphene loading, Suggesting that there existed a mechanical percolation probably due to the nanosheet restacking in the case of higher graphene content, which was consistent with the other reports [16, 57, 58]. On the contrary, the elongation at break of the nanocomposites gradually decreased with graphene loading in contrast to that of pure PMMA. The value of the elongation at break decreased from 6% for pure PMMA to 3.5% for C_{18}-graphene-1.5/PMMA. The mechanical reinforcement with low graphene loading could be attributed to the homogeneous dispersion of graphene sheets in the matrix and the strong interfacial adhesion between chemi-

cally modified graphene and PMMA. Because of the high surface area of graphene in the nanocomposites, the applied stress was expected to transfer effectively from the matrix to graphene layers resulting in enhancement of mechanical properties [59, 60].

4. Conclusions

Chemically modified graphene by long alkyl chain was prepared and the graphene/PMMA nanocomposites were successfully fabricated *via* a facile *in situ* bulk polymerization. Thermal and mechanical properties of the nanocomposites were significantly enhanced at very low graphene loadings. The reinforcement with low graphene loading was attributed to homogeneous dispersion of the nanosheets and enhanced nanofiller-matrix interfacial interaction. Because of easy performance of functionalized graphene and bulk polymerization, the facile method presented here could be extended to the implementation of other graphene-based polymer nanocomposites.

Acknowledgements

The authors would like to gratefully acknowledge the supports by Municipal Science Foundation Project of CQ CSTC (No.2007BB4442) and of CQEC (No.KJ110421) and Open-end Fund of Hi-tech Lab for Mountain Road Construction and Maintenance, CQTJU (CQMRCM-10-5).

References

[1] Geim A. K., Novoselov K. S.: The rise of graphene. Nature Materials, **6**, 183–191 (2007).
DOI: 10.1038/nmat1849

[2] Geim A. K.: Graphene: Status and prospects. Science, **324**, 1530–1534 (2009).
DOI: 10.1126/science.1158877

[3] Allen M. J., Tung V. C., Kaner R. B.: Honeycomb carbon: A review of graphene. Chemical Review, **110**, 132–145 (2010).
DOI: 10.1021/cr900070d

[4] Sun Z., James D. K., Tour J. M.: Graphene chemistry: Synthesis and manipulation. The Journal of Physical Chemistry Letters, **2**, 2425–2432 (2011).
DOI: 10.1021/jz201000a

[5] Kim J., Kim F., Huang J.: Seeing graphene-based sheets. MaterialsToday, **13**, 28–38 (2010).
DOI: 10.1016/S1369-7021(10)70031-6

[6] Zhu Y., Murali S., Cai W., Li X., Suk J. W., Potts J. R., Ruoff R. S.: Graphene and graphene oxide: Synthesis, properties, and applications. Advanced Materials, **22**, 3906–3924 (2010).
DOI: 10.1002/adma.201001068

[7] Wu J., Pisula W., Müllen K.: Graphenes as potential material for electronics. Chemical Review, **107**, 718–747 (2007).
DOI: 10.1021/cr068010r

[8] Singh V., Joung D., Zhai L., Das S., Khondaker S. I., Seal S.: Graphene based materials: Past, present and future. Progress in Materials Science, **56**, 1178–1271 (2011).
DOI: 10.1016/j.pmatsci.2011.03.003

[9] Stankovich S., Dikin D. A., Dommett G. H. B., Kohlhaas K. M., Zimney E. J., Stach E. A., Piner R. D., Nguyen S. T., Ruoff R. S.: Graphene-based composite materials. Nature, **442**, 282–286 (2006).
DOI: 10.1038/nature04969

[10] Shao Y., Wang J., Wu H., Liu J., Aksay I. A., Lin Y.: Graphene based electrochemical sensors and biosensors: A review. Electroanalysis, **22**, 1027–1036 (2010).
DOI: 10.1002/elan.200900571

[11] Bao Q., Zhang H., Yang J. X., Wang S., Tang D. Y., Jose R., Ramakrishna S., Lim C. T., Loh K. P.: Graphene–polymer nanofiber membrane for ultrafast photonics. Advanced Functional Materials, **20**, 782–791 (2010).
DOI: 10.1002/adfm.200901658

[12] Zhu Y., Murali S., Stoller M. D., Ganesh K. J., Cai W., Ferreira P. J., Pirkle A., Wallace R. M., Cychosz K. A., Thommes M., Su D., Stach E. A., Ruoff R. S.: Carbon-based supercapacitors produced by activation of graphene. Science, **332**, 1537–1541 (2011).
DOI: 10.1126/science.1200770

[13] Kim H., Abdala A. A., Macosko C. W.: Graphene/polymer nanocomposites. Macromolecules, **43**, 6515–6530 (2010).
DOI: 10.1021/ma100572e

[14] Kuilla T., Bhadra S., Yao D., Kim N. H., Bose S., Lee J. H.: Recent advances in graphene based polymer composites. Progress in Polymer Science, **35**, 1350–1375 (2010).
DOI: 10.1016/j.progpolymsci.2010.07.005

[15] Potts J. R., Dreyer D. R., Bielawski C. W., Ruoff R. S.: Graphene-based polymer nanocomposites. Polymer, **52**, 5–25 (2011).
DOI: 10.1016/j.polymer.2010.11.042

[16] Rafiee M. A., Rafiee J., Wang Z., Song H., Yu Z-Z., Koratkar N.: Enhanced mechanical properties of nanocomposites at low graphene content. ACS Nano, **3**, 3884–3890 (2009).
DOI: 10.1021/nn9010472

[17] Loh K. P., Bao Q., Ang P. K., Yang J.: The chemistry of graphene. Journal of Materials Chemistry, **20**, 2277–2289 (2010).
DOI: 10.1039/b920539j

[18] Park R., Ruoff R. S.: Chemical methods for the production of graphenes. Nature. Nanotechnology, **4**, 217–224 (2009).
DOI: 10.1038/nnano.2009.58

[19] Dreyer D. R., Park S., Bielawski C. W., Ruoff R. S.: The chemistry of graphene oxide. Chemical Society Reviews, **39**, 228–240 (2010).
DOI: 10.1039/b917103g

[20] Salavagione H. J., Gómez M. A., Martínez G.: Polymeric modification of graphene through esterification of graphite oxide and poly(vinyl alcohol). Macromolecules, **42**, 6331-6334 (2009).
DOI: 10.1021/ma900845w

[21] Park S., Dikin D. A., Nguyen S. T., Ruoff R. S.: Graphene oxide sheets chemically cross-linked by polyallylamine. The Journal of Physical Chemistry C, **113**, 15801–15804 (2009).
DOI: 10.1021/jp907613s

[22] Hsiao M-C., Liao S-H., Yen M-Y., Liu P-I., Pu N-W., Wang C-A., Ma C-C. M.: Preparation of covalently functionalized graphene using residual oxygen-containing functional groups. ACS Applied Materials and Interfaces, **2**, 3092–3099 (2010).
DOI: 10.1021/am100597d

[23] Salavagione H. J., Martínez G.: Importance of covalent linkages in the preparation of effective reduced graphene oxide–poly(vinyl chloride) nanocomposites. Macromolecules, **44**, 2685–2692 (2011).
DOI: 10.1021/ma102932c

[24] Sun S., Cao Y., Feng J., Wu P.: Click chemistry as a route for the immobilization of well-defined polystyrene onto graphene sheets. Journal of Materials Chemistry, **20**, 5605–5607 (2010).
DOI: 10.1039/c0jm01269f

[25] Pan Y., Bao H., Sahoo N. G., Wu T., Li L.: Water-soluble poly(*N*-isopropylacrylamide)–graphene sheets synthesized via click chemistry for drug delivery. Advanced Functional Materials, **21**, 2754–2763 (2011).
DOI: 10.1002/adfm.201100078

[26] Xu X., Luo Q., Lv W., Dong Y., Lin Y., Yang Q., Shen A., Pang D., Hu J., Qin J., Li Z.: Functionalization of graphene sheets by polyacetylene: Convenient synthesis and enhanced emission. Macromolecular Chemistry Physics, **212**, 768–773 (2011).
DOI: 10.1002/macp.201000608

[27] Pramoda K. P., Hussain H., Koh H. M., Tan H. R., He C. B.: Covalent bonded polymer–graphene nanocomposites. Journal of Polymer Science Part A: Polymer Chemistry, **48**, 4262–4267 (2010).
DOI: 10.1002/pola.24212

[28] Liu J., Yang W., Tao L., Li D., Boyer C., Davis T. P.: Thermosensitive graphene nanocomposites formed using pyrene-terminal polymers made by RAFT polymerization. Journal of Polymer Science Part A: Polymer Chemistry, **48**, 425–433 (2010).
DOI: 10.1002/pola.23802

[29] Gonçalves G., Marques P. A. A. P., Barros-Timmons A., Bdkin I., Singh M. K., Emami N., Grácio J.: Graphene oxide modified with PMMA *via* ATRP as a reinforcement filler. Journal of Materials Chemistry, **20**, 9927–9934 (2010).
DOI: 10.1039/c0jm01674h

[30] Fang M., Wang K., Lu H., Yang Y., Nutt S.: Covalent polymer functionalization of graphene nanosheets and mechanical properties of composites. Journal of Materials Chemistry, **19**, 7098–7105 (2009).
DOI: 10.1039/b908220d

[31] Deng Y., Li Y., Dai J., Lang M., Huang X.: An efficient way to functionalize graphene sheets with presynthesized polymer via ATNRC chemistry. Journal of Polymer Science Part A: Polymer Chemistry, **49**, 1582–1590 (2011).
DOI: 10.1002/pola.24579

[32] Lee S. H., Dreyer D. R., An J., Velamakanni A., Piner R. D., Park S., Zhu Y., Kim S. O., Bielawski C. W., Ruoff R. S.: Polymer brushes via controlled, surface-initiated atom transfer radical polymerization (ATRP) from graphene oxide. Macromolecular Rapid Communications, **31**, 281–288 (2010).
DOI: 10.1002/marc.200900641

[33] Lin Y., Jin J., Song M.: Preparation and characterisation of covalent polymer functionalized graphene oxide. Journal of Materials Chemistry, **21**, 3455–3461 (2011).
DOI: 10.1039/c0jm01859g

[34] Liang J., Huang Y., Zhang L., Wang Y., Ma Y., Guo T., Chen Y.: Molecular-level dispersion of graphene into poly(vinyl alcohol) and effective reinforcement of their nanocomposites. Advanced Functional Materials, **19**, 1–6 (2009).
DOI: 10.1002/adfm.200801776

[35] Ramanathan T., Abdala A. A., Stankovich S., Dikin D. A., Herrera-Alonso M., Piner R. D., Adamson D. H., Schniepp H. C., Chen X., Ruoff R. S., Nguyen S. T., Aksay I. A., Prud'homme R. K., Brinson L. C.: Functionalized graphene sheets for polymer nanocomposites. Nature Nanotechnology, **3**, 327–331 (2008).
DOI: 10.1038/nnano.2008.96

[36] Vickery J. L., Patil A. J., Mann S.: Fabrication of graphene–polymer nanocomposites with higher-order three-dimensional architectures. Advanced Materials, **21**, 2180–2184 (2009).
DOI: 10.1002/adma.200803606

[37] Kuila T., Bose S., Hong C. E., Uddin M. E., Khanra P., Kim N. H., Lee J. H.: Preparation of functionalized graphene/linear low density polyethylene composites by a solution mixing method. Carbon, **49**, 1033–1051 (2011).
DOI: 10.1016/j.carbon.2010.10.031

[38] Putz K. W., Compton O. C., Palmeri M. J., Nguyen S. T., Brinson L. C.: High-nanofiller-content graphene oxide–polymer nanocomposites via vacuum-assisted self-assembly. Advanced Functional Materials, **20**, 3322–3329 (2010).
DOI: 10.1002/adfm.201000723

[39] Zhao X., Zhang Q., Hao Y., Li Y., Fang Y., Chen D.: Alternate multilayer films of poly(vinyl alcohol) and exfoliated graphene oxide fabricated via a facial layer-by-layer assembly. Macromolecules, **43**, 9411–9416 (2010).
DOI: 10.1021/ma101456y

[40] Liu J., Tao L., Yang W., Li D., Boyer C., Wuhrer R., Braet F., Davis T. P.: Synthesis, characterization, and multilayer assembly of pH sensitive graphene–polymer nanocomposites. Langmuir, **26**, 10068–10075 (2010).
DOI: 10.1021/la1001978

[41] Potts J. R., Lee S. H., Alam T. M., An J., Stoller M. D., Piner R. D., Ruoff R. S.: Thermomechanical properties of chemically modified graphene/poly(methyl methacrylate) composites made by *in situ* polymerization. Carbon, **49**, 2615–2623 (2011).
DOI: 10.1016/j.carbon.2011.02.023

[42] Oh S. M., Lee H., Jeong H. M., Kim B. K.: The properties of functionalized graphene sheet/poly(ethyl methacrylate) nanocomposites: The effects of preparation method. Macromolecular Research, **19**, 379–384 (2011).
DOI: 10.1007/s13233-011-0404-0

[43] Hu H., Wang X., Wang J., Wan L., Liu F., Zheng H., Chen R., Xu C.: Preparation and properties of graphene nanosheets–polystyrene nanocomposites via *in situ* emulsion polymerization. Chemical Physics Letters, **484**, 247–253 (2010).
DOI: 10.1016/j.cplett.2009.11.024

[44] Wang J., Hu H., Wang X., Xu C., Zhang M., Shang X.: Preparation and mechanical and electrical properties of graphene nanosheets–poly(methyl methacrylate) nanocomposites via *in situ* suspension polymerization. Journal of Applied Polymer Science, **122**, 1866–1871 (2011).
DOI: 10.1002/app.34284

[45] Ray S. S., Okamoto M.: Polymer/layered silicate nanocomposites: A review from preparation to processing. Progress in Polymer Science, **28**, 1539–1641 (2003).
DOI: 10.1016/j.progpolymsci.2003.08.002

[46] Moniruzzaman M., Winey K. I.: Polymer nanocomposites containing carbon nanotubes. Macromolecules, **39**, 5194–5205 (2006).
DOI: 10.1021/ma060733p

[47] Hummers W. S., Offeman R. E.: Preparation of graphitic oxide. Journal of the American Chemical Society, **80**, 1339 (1958).
DOI: 10.1021/ja01539a017

[48] Cao Y., Feng J., Wu P.: Alkyl-functionalized graphene nanosheets with improved lipophilicity. Carbon, **48**, 1683–1685 (2010).
DOI: 10.1016/j.carbon.2009.12.061

[49] Stankovich S., Dikin D. A., Piner R. D., Kohlhaas K. A., Kleinhammes A., Jia Y., Wu Y., Nguyen S. T., Ruoff R. S.: Synthesis of graphene-based nanosheets via chemical reduction of exfoliated graphite oxide. Carbon, **45**, 1558–1565 (2007).
DOI: 10.1016/j.carbon.2007.02.034

[50] Yuan X-Y.: Progress in preparation of graphene. Journal of Inorganic Materials, **26**, 561–570 (2011).
DOI: 10.3724/SP.J.1077.2011.00561

[51] Wang G., Shen X., Wang B., Yao J., Park J.: Synthesis and characterisation of hydrophilic and organophilic graphene nanosheets. Carbon, **47**, 1359–1364 (2009).
DOI: 10.1016/j.carbon.2009.01.027

[52] Niyogi S., Bekyarova E., Itkis M. E., Mcwilliams J. L., Hamon M. A., Haddon R. C.: Solution properties of graphite and graphene. Journal of the American Chemical Society, **128**, 7720–7721 (2006).
DOI: 10.1021/ja060680r

[53] Tessonnier J-P., Barteau M. A.: Dispersion of alkyl-chain-functionalized reduced graphene oxide sheets in nonpolar solvents. Langmuir, **28**, 6691–6697 (2012).
DOI: 10.1021/la2051614

[54] Park S. J., Cho M. S., Lim S. T., Choi H. J., Jhon M. S.: Synthesis and dispersion characteristics of multi-walled carbon nanotube composites with poly(methyl methacrylate) prepared by in-situ bulk polymerization. Macromolecular Rapid Communications, **24**, 1070–1073 (2003).
DOI: 10.1002/marc.200300089

[55] Qu X., Guan T., Liu G., She Q., Zhang L.: Preparation, structural characterization, and properties of poly (methyl methacrylate)/montmorillonite nanocomposites by bulk polymerization. Journal of Applied Polymer Science, **97**, 348–357 (2005).
DOI: 10.1002/app.21749

[56] Li W., Tang X-Z., Zhang H-B., Jiang Z-G., Yu Z-Z., Du X-S., Mai Y-W.: Simultaneous surface functionalization and reduction of graphene oxide with octadecylamine for electrically conductive polystyrene composites. Carbon, **49**, 4724–4730 (2011).
DOI: 10.1016/j.carbon.2011.06.077

[57] Zhao X., Zhang Q., Chen D., Lu P.: Enhanced mechanical properties of graphene-based poly(vinyl alcohol) composites. Macromolecules, **43**, 2357–2363 (2010).
DOI: 10.1021/ma902862u

[58] Yuan X.: Enhanced interfacial interaction for effective reinforcement of poly(vinyl alcohol) nanocomposites at low loading of graphene. Polymer Bulletin, **67**, 1785–1797 (2011).
DOI: 10.1007/s00289-011-0506-z

[59] Salavagione H. J., Martínez G., Ellis G.: Recent advances in the covalent modification of graphene with polymers. Macromolecular Rapid Communications, **32**, 1771–1789 (2011).
DOI: 10.1002/marc.201100527

[60] Gong L., Kinloch I. A., Young R. J., Riaz I., Jalil R., Novoselov K. S.: Interfacial stress transfer in a graphene monolayer nanocomposite. Advanced Materials, **22**, 2694–2697 (2010).
DOI: 10.1002/adma.200904264